CHARACTERISTICS OF $ZnO/CuInSe_2$ HETEROJUNCTIONS AND $CuInSe_2$ HOMOJUNCTIONS

by

C. X. Qiu

A thesis submitted to the Faculty of Graduate Studies and Research in partial fulfillment of the requirements for the degree of Master of Engineering

Department of Electrical Engineering
McGill University
Montreal, Canada

ABSTRACT

The objectives of the work are (1) to study the doping effects of ZnO thin films, (2) to study ZnO/$CuInSe_2$ heterojunctions and (3) to study $CuInSe_2$ homojunctions. Both indium- and tin-doped ZnO films with a thickness of about 1 micrometer have been deposited on glass substrates using an rf magnetron sputtering technique with high purity argon gas. The targets used for the sputtering contained weighted amounts of ZnO and In_2O_3 (or SnO_2). It was found that the electrical and optical properties of the ZnO films were affected by the presence of indium or tin. For indium-doped ZnO films, the room temperature dark resistivity decreased by 4 orders of magnitute as the indium oxide content was increased from 0 to 10 wt.%. For tin-doped films, the resistivity decreased by about 3 orders of magnitude as the tin oxide content was increased from 0 to 2 wt.% and was essentially constant as the tin oxide content was further increased to 10 wt.%. Effect of the argon pressure on the resistivity was also studied. It was observed that the higher the pressure (within the range from 5 to 40 mTorr), the higher the resistivity. Using the sputtering technique established in the present work, several heterojunctions were fabricated by depositing a layer of low resistivity ZnO film on n- or p-type Bridgman-grown monocrystalline $CuInSe_2$

samples. Current-voltage and differential capacitance-voltage measurements have been carried out on the fabricated devices. It was found that current transport in the devices was dominated by a tunneling process (or a shunting effect) in the low voltage region. In the intermediate voltage region, this was dominated by a recombination/thermal emission process. From the differential capacitance measurements, it was found that the apparent barrier height was greater than that predicted from an ideal energy band diagram constructed from material parameters. A polarity reversal effect was also found for the open circuit voltage of the isotype ZnO(n)/$CuInSe_2$(n) devices. These were interpreted by a dipole effect and effects of interface states. From these results, energy band diagrams have been constructed for the heterojunctions. Temperature-dependent dark current-voltage characteristics were also investigated on $CuInSe_2$ homojunctions fabricated by diffusing indium or bismuth into p-type monocrystalline $CuInSe_2$ samples. It was found that a recombination process dominated the current in these devices in the intermediate voltage region. Differential capacitance and transient capacitance effects also have been studied. It was found that deep levels were present in monocrystalline $CuInSe_2$.

Résumé

Les buts de ce travail sont: 1) étudier le dopage de couches minces de ZnO, 2) étudier les hétérojonctions de ZnO/$CuInSe_2$ et, 3) étudier les homojonctions de $CuInSe_2$. Des couches minces de ZnO, d'une épaisseur d'environ 1 micron et dopées à l'indium ainsi qu'à l'étain ont été déposées sur des substrats de verre par pulvérisation RF par magnétron dans une atmosphère d'argon de grande pureté. Les cibles utilisées pour la pulvérisation contenaient des quantitées pesées de ZnO et In_2O_3 (ou SnO_2). On a trouvé que les propriétés optiques et électriques des couches de ZnO étaient modifées par la présence d'indium ou d'étain. Pour les films de ZnO dopés à l'étain, la résistivité d'obscurité, à la température de la pièce, a diminué de 4 ordres de grandeur avec une augmentation de la quantité d'oxide d'indium de 0 à 10% (poids). Pour les films dopés à l'étain, la résistivité a diminué par approximativement 3 ordres de grandeur avec une augmentation du contenu en oxyde d'étain de 0 à 2% (poids), et est demeurée essentiellement constante avec une augmentation supplémentaire du contenu en oxyde d'étain jusqu'à 10% (poids). L'effet de la pression d'argon a aussi été étudié. On a observé que la résistivité augmente avec la pression (dans le domaine de 5 à 40 mtorr). En utilisant la technique de pulvérisation établie dans ce travail, plusieurs hétérojonctions on été fabriquées en déposant une couche mince de ZnO de faible résistivité sur des échantillons monocristallins de $CuInSe_2$ de type n ou p préparés par croissance de Bridgman. Des mesures courant-tension et capacitance différentielle-tension ont été faites sur les dispositifs fabriqués.

On a trouvé que le transport de courant dans les dispositifs est dominé par un effet tunnel (ou "shunting") dans la région de basse tension. Dans la région de tension intermédiaire, c'est un processus de recombinaison/émission thermique qui domine. A partir des mesures de capacitance différentielle, on a trouvé

que la barrière de potentiel apparente est plus grande que celle prévue à partir d'un diagramme de bandes d'énergie idéal construit avec les paramètres des matériaux. On a aussi trouvé un effet d'inversion de polarité pour la tension en circuit ouvert des dispositifs isotypes ZnO(n)/$CuInSe_2$(n). Ces résultats sont interprétés par un effet dipolaire et l'effet des états d'interface. Des diagrammes de bandes d'énergie pour les hétérojonctions ont aussi été construits à partir de ces résultats.

Des caractéristiques de courant d'obscurité tension en fonction de la température ont été déterminées pour des homojonctions de $CuInSe_2$ fabriquées par diffusion de bismuth indium dans des échantillons monocristallins de $CuInSe_2$ de type p. On a trouvé qu'un processus de recombinaison est dominant pour le courant de ces dispositifs dans la région de tension intermédiaire. Les effets de capacitances différentielle et transitoire ont aussi été étudiées. On a trouvé que des niveaux profonds sont présents dans le $CuInSe_2$ monocristallin.

ACKNOWLEDGEMENTS

The author wishes to express her sincere gratitude to her supervisor, Dr. I. Shih for his guidance throughout this study.

Acknowledgements are also due to the Natural Sciences and Engineering Research Council of Canada and Chongqing University for the financial support.

The author is specially grateful to her parents and to Mr. and Mrs. S.C. Shih for their encouragement and to her husband for his understanding during the study.

TABLE OF CONTENTS

CHAPTER 1 INTRODUCTION

In views of limited energy resources on the earth and the increased demand of energy consumption, it is important to explore alternative and renewable energy resources. There are several candidates currently being developed. These include solar energy, energy from ocean waves and wind energy. Among them, the solar energy using direct conversion of photovoltaic cells has been considered to be a promising candidate because of the following reasons. (1) Considering the life-time of the earth, the sun is a longevous energy source. (2) Using solar cells, light can be converted directly into electricity. (3) There is no environmental contamination problem. (4) There are no moving parts in the system making the maintenance requirements to be minimal. (5) Solar cells with a high conversion effeciency can be fabricated. The first solar cell was fabricated using a diffused silicon homojunction in 1954 [1.1], since then several phtovoltaic structures have been developed.

There are several promising monocrystalline materials which have been considered and developed for photovoltaic application. Among them, monocrystalline silicon and GaAs have been extensively studied. Cells with an effeciency towards 20% have been achieved [1.2, 1.3]. However, it is not

economic for these single crystal cells to be used in large scale terrestrial applications. For such large scale applications, thin film cells appeared to be more appropriate due to the lower cost and smaller amount of material consumption. There already have been many research and development efforts on thin film devices. At the present, amorphous silicon, CdTe and $CuInSe_2$ appear to be successful candidates for low cost photovoltaic application.

Among the three thin film materials, $CuInSe_2$ has been considered to be the best candidate for future application due mainly to its high optical absorption coeffecient for photons with an energy above bandgap [1.4] and long term thermal stability [1.5]. Although high efficiency cells based on $CuInSe_2$ have been demonstrated [1.5], there are still many unanswered questions about the properties of this material. For example, defects in the crystalline $CuInSe_2$ have not been extensively studied. The defects in this material are important in determining minority carrier recombination processes and the performance of the final photovoltaic devices. Therefore, the main objective of the present research work is to study monocrystalline $CuInSe_2$. Experiments have been initiated to study both heterojunctions and homojunctions of this material. These were done in an attempt to obtain information about the current transport processes of the devices and deep levels (resulting from

defects) in the material. The information is useful for the development of this material for future device application.

There are several techniques for studying of deep levels in semiconductors. For example, deep level transient spectroscopy technique, thermal stimulated current technique and thermal stimulated differential capacitance technique. However, these techniques have not been applied to $CuInSe_2$. In the present work, differential capacitance measurements were made on $CuInSe_2$ junctions in order to investigate the effect of deep levels on the junction characteristics.

Apart from the absorbing material, window materials are also very important for photovoltaic devices. There have been many research activities on window materials like cadmium oxide (CdO) [1.6], cadmium sulfide (CdS) [1.7], cadmium zinc sulfide (CdZnS) [1.5], indium oxide (In_2O_3) [1.8], tin oxide (SnO_2) [1.9] and indium tin oxide (ITO) [1.10]. Arising from these research activities, the above-mentioned window materials have found applications in photovoltaic devices. In this work, another important window material, zinc oxide (ZnO), has been investigated and used to form $ZnO/CuInSe_2$ heterojunctions. Electrical and optical properties of the devices have been studied.

The arrangement of the thesis is as follows. Fabrication

processes for ZnO thin films using an rf sputtering technique and the effects of doping (by indium or tin) on electrical (resistivity) and optical properties of ZnO films are first given in chapter 2. Using the ZnO deposition technique developed, heterojunctions of the forms ZnO(n)/$CuInSe_2$(p) and ZnO(n)/$CuInSe_2$(n) have been fabricated and studied. Characteristics of these anisotype and isotype heterojunctions are given in chapter 3. In chapter 4, current transport mechanisms in monocrystalline $CuInSe_2$ homojunctions are discussed followed by preliminary results of the deep level investigation. Finally, main conclusions of the thesis are presented in chapter 5.

CHAPTER 2 INDIUM- AND TIN-DOPED ZINC OXIDE FILMS PREPARED BY RF MAGNETRON SPUTTERING

2.1 INTRODUCTION

Zinc oxide is an n-type semiconductor with a direct energy band gap of about 3.3 eV which is wide enough to transmit most of the terrestrial sunlight. The reflectivity of light from ZnO surface is small, therefore, it is a promising candidate for photovoltaic window material applications. Crystalline ZnO has a hexagonal structure [2.1] (the lattice parameters are: a_o = 3.24 Å; c_o = 5.23 Å [2.2]). Comparing with other metal oxide semiconductors, it is an inexpensive material and can be fabricated using simple and inexpensive deposition techniques.

Recently, many authors have reported results of ZnO thin films prepared using various techniques such as: spray pyrolysis, dc (magnetron) sputtering, rf (magnetron) sputtering, reactive sputtering, enhanced reactive evaporation and (OM)CVD. The purpose of these experiments is to prepare high resistivity ZnO films for surface acoustic wave transducers [2.3]. However, zinc oxide thin films with low resistivity of the order of 10^{-2} to 10^{-4} ohm-cm and high optical transmission over the whole solar spectral range have

been prepared only in recent years. The techniques used for the low resistivity film preparation are: enhanced reactive evaporation [2.4], rf reactive magnetron sputtering [2.5] and spray pyrolysis with a heat treatment [2.6]. Results reported by K. Ito and T. Nakazawa [2.7] and H. Nanto et al [2.8] showed that ZnO films with low resistivity could be obtaind on the upper surface of a substrate placed parallel to the target or on the two surfaces of a substrate placed perpendicular to the target using the rf sputtering technique. Low resistivity ZnO films also can be obtained by ajusting the film stoichiometry (sputtering from a ZnO + Zn target, or from a ZnO target using a mixture of hydrogen and argon gas) [2.9, 2.5]. Using a doping technique, T. Minami et al [2.10] found that ZnO films doped with aluminum not only showed a very low resistivity but also showed more stable electrical and optical properties. The results indicated that impurity doping could be a feasible method for preparing thermally stable ZnO films with low resistivity .

In this chapter, results of indium- and tin-doped ZnO films are reported. X-ray diffraction, EPMA, optical transmission and electrical measurements have been performed to characterize the deposited films.

2.2 PREPARATION METHODS

2.2.1 RF Sputtering System

In the present experiments, ZnO thin films were prepared using an rf sputtering system. The system consisted of a planar magnetron rf sputter source (US' Gun II, US Inc.), a 500 W rf power supply (13.56 MHz, with auto-tuning) and a Varian vaccum system with a conventional diffusion pump unit. A schematic diagram of the rf sputtering chamber is shown in figure 2.1.

For rf sputtering, a planar target which could be conducting or nonconducting is insulated from the rf generator by a plate insulator and used as the source material. This arrangement is necessary since it has been shown [2.11] that the electrode for the sputtering target in an rf system must be an insulator or be coupled to the rf power supply capacitively. Center and ring permanent magnets are arranged just under the target support and magnet housing so that there is a ring region immediately in front of the target where the magnetic field lines are all parallel to the target surface. Figure 2.2 shows a circular planar magnetron sputtering source where curved lines represent magnetic field lines. Using the magnetron technique, secondary electrons will be given a curved trajectory under the influence of the

transverse magnetic field so the direct bombardment of the substrate by the electrons is minimized. This effect has a benefit in decreasing the power dissipation thus reducing the substrate heating. The helix-like path of the secondary electrons also makes a larger number of collisions of the secondary electrons with sputtering gas atoms which will be ionized and then bombard the target. This effect allows sputtering with a high yield to be performed. However, the increased amount of target bombardment by the ions will result in target overheating. Therefore, a water cooling system is necessary to remove the generated heat by cooling the insulating plate to which the target is attached. The pressure of sputtering gas (Ar, in the present case) will greatly affect deposition rate and the energy of neutral particles incident on the substrate. The gas pressure in the experimental system is controlled by ajusting a leak valve and the orifice opening (between the deposition chamber and the diffusion pump shown in figure 2.1).

2.2.2 Experimental Procedure

Several dish-shaped aluminum holders (inner diameter of 4.7 cm) were fabricated and used to contain powder targets. Pure ZnO targets were made from high purity (five nine's, Johnson Matthey Chemicals, Ltd.) ZnO powder. For doping cases, 8 gm ZnO powder was mixed thoroughly with the

required amount of high purity In_2O_3 or SnO_2 powder (both five nine's) and pressed into target. To facilitate the experiments, weight percentages of In_2O_3/ZnO and SnO_2/ZnO were used in the present work. Microscope glass slides were used as substrates which were placed parallel to the target surface. The separation between substrate and target was chosen to be about 3 cm. No intentional substrate heating or cooling was applied throughout the experiments even though a relatively high temperature (estimated to be about 100°C) would be produced on substrates when large incident rf power (up to 200 W) was applied.

In order to get a constant deposition rate, incident rf power was fixed at 60 W for most of the deposited films (effects of variation in the rf power, from 30 to 200 W, were also investigated) and the typical deposition time was about 30 minutes. Most of the sputtering runs were carried out under high purity argon atmosphere at a pressure of 5 mTorr. To study the pressure effects, other pressure values were also adopted for the film preparation.

Deposition experiments of ZnO films were carried out as follows. The deposition chamber was first pumped down to a residual gas pressure of about 5×10^{-6} Torr, using an oil diffusion pump with a liquid nitrogen trap. High purity argon gas was then introduced to initiate the plasma. It was found

that the plasma could be induced in the present system only at an argon pressure higher than 25 mTorr. As soon as the plasma had been established, the argon pressure was controlled to 5 mTorr (or other required values) by adjusting the leak valve. The orifice opening was kept to the same position so that a constant gas flow rate could be retained. The deposition was continued for a period of about 30 minutes. After this, the rf power was turned off. The sputtered samples were maintained in the system for at least 20 minutes before being taken out of the system to aviod the film cracking.

It has been reported that the resistivity of ZnO films can be greatly reduced by selecting suitable deposition conditions: such as gas pressure, rf power, substrate position and substrate orientation [2.7, 2.8]. However, the purpose of the present experements was to determine how the presence of In and Sn would affect the quality of the doped films. Therefore, no special attention was paid to optimization of the film quality. During the experiments, a mixture of argon and oxygen (up to 10%) was also used to investigate the effects of the oxygen gas. It was found that the larger the oxygen content in the sputtering gas, the higher the resistivity of the films (results not shown). This effect is consistant with those reported by many other authors [2.12].

2.3 EXPERIMENTAL RESULTS

2.3.1 Thickness Measurements

A commercial stylus (Dektak Surface Profile Measuring System, Sloan Technology Corp.) was used to determine the thickness of the deposited films. Under the deposition conditions described above (5 mTorr, 30 minutes, 60 W), the typical thickness of the deposited films was found to be about 1 μm. The film thickness was also estimated by observing the number of interference fringes under an optical microscope (with filtered red light source). A quasi-linear relationship between the measured thickness and the number of interference fringes is shown in figure 2.3. Figure 2.3 was used for thickness estimation in routine deposition runs.

2.3.2 Experimental Results

Tables 2.1 and 2.2 give the results of In- and Sn-doped films. Several ZnO targets containing different amounts of In_2O_3 (or SnO_2) were used for the fabrication. Since the deposition rate and film resistivity change as the deposition experiment goes on (conditions of the target surface change with the bombardment of the accelerated ions), only the third and fourth samples deposited for each new target are listed in the two tables. Number of

interference fringes was counted under the microscope and film thickness was estimated from figure 2.3. Four-point probe was used to determine the room temperature sheet resistance, R_s, which is simply given by 4.5x(V/I). Here V and I are the measured voltage and current respectively. From this relation, resistivity of the film can be easily caculated.

2.3.3 EPMA (Electron Probe Micro Analysis)

Results from electron probe micro analysis for both In- and Sn-doped films are shown in figures 2.4 and 2.5. It is noted that for the Sn-doped films, the Sn content in the films is roughly equal to that in the targets. However, the In-content in the In-doped films is less than that in the targets especially for higher In_2O_3/ZnO weight percentages.

2.3.4 X-ray Results

In order to determine the crystalline structure of the deposited films, several samples deposited on glass slides were examined by X-ray diffractometry. A schematic diagram of the X-ray set-up is given in figure 2.6. Figure 2.7 shows a typical example of the diffraction experiments where X-ray intensity is plotted versus the angle between the incident and the diffracted beams for one of the In-doped (2 wt% In_2O_3

in the target) ZnO films. The X-ray diffraction results indicated that all deposited films were polycrystalline with a hexagonal structure and had a preferred (002) orientation. These results are similar to that obtained by Nayar [2.9]. However, doping of In and Sn introduced a lattice constant increment, Δd, and the value of Δd was found to increase with the increase of In or Sn content in the target. Figure 2.8 shows the calculated Δd versus the weight percentage of In_2O_3/ZnO or SnO_2/ZnO. It is noted that Δd increases more rapidly with the increase of the doping concentration for Sn-doped films than that for In-doped films. The difference in lattice constant increment could be a reason for the difference in optical transmission for In- and Sn-doped films (to be described in section 2.3.7).

2.3.5 Electrical Resistivity Results

Figure 2.9 shows the measured film resistivity plotted versus the In_2O_3 and SnO_2 content in the targets. The data were taken from the samples sputtered at 60 W, 5 mTorr for 30 minutes. It is seen that the resistivity decreases by about 4 orders of magnitude as the In_2O_3 content is increased from 0 to 10 wt% and by about 3 orders of magnitude for the Sn-doped films. It is also noted that the reproducibility of resistivity is improved for the films deposited with high In_2O_3 or SnO_2 content. A further decrement of resistivity for

In-doped films at higher doping concentration is expected. Resistivity of the films doped with SnO_2 remained essentially constant for a SnO_2/ZnO ratio in the range from 2 to 10%.

Using a target with 2 wt% In_2O_3, several films have been sputtered with different values of incident rf power and different argon pressure. It was found that the film resistivity decreased as the power was increased and increased with the increase of the Ar pressure. The results are presented in figures 2.10 and 2.11. From these samples, effects of incident rf power and gas pressure on the deposition rates were also studied (see figures 2.12 and 2.13). From figures 2.10 to 2.13, a cursory comment can be made that a relatively high deposition rate will result in a relatively low resistivity.

2.3.6 Mobility and Carrier Concentration

Hall effect measurements were carried out at room temperature (under a dark condition) for two samples deposited on glass substrates. The films were prepared using a target containing 2 wt% of In_2O_3 powder and the typical conditions (60 W, 5 mTorr) were maintained during the processes. A permanent magnet with a magnetic flux density of 0.2 tesla was used for the measurements and an HP model 3457A digital voltmeter was used to measure Hall voltages. From the

measurements, a Hall mobility value of 4 $cm^2/V\text{-}Sec$ was found for the samples. This value is comparable to the results obtained by K. Ito and T. Nakazawa [2.7]. The electron concentration was about 10^{20} cm^{-3} from the present results.

2.3.7 Optical Transmission Results

For high conversion efficiency solar cell application, large optical transmission values in the solar spectrum of the top layer is as important as the requirement of having low resistivity values. In the present experiments, optical transmission measurements for both In- and Sn-doped ZnO films were carried out at room temperature. A Beckman monochromator with a slit width of 1 mm was used as the light source. No other light source was applied during the measurements. Figure 2.14 shows a schematic diagram of the sample under the optical transmission measurement. Here I_o is the monochromator output intensity while I_1 and I_2 represent the transmitted light intensities for ZnO film coated glass and the uncoated one respectively. A Model PIN 6DP detector (United Detector Technology) was put behind the sample to measure I_1 and I_2. The same detector was used to measure I_o. Finally, the transmission value was obtained by taking the ratio I_1/I_2.

The results measured at 0.7 and 0.5 μm wavelengths for

films with different In and Sn content are shown in figures 2.15 and 2.16. It is seen that the transmission value for In-doped films at 0.7 μm is essentially constant (up to 85%) for the composition range studied and that at 0.5 μm is affected by the presence of In. For the Sn-doped films, the transmission value for both wavelengths first decreases with the increase in SnO_2 content, reaches minima at 5 wt%, then increases as the SnO_2 content is further increased. Transmission values at wavelengths in the range of 0.4-0.8 μm for four samples (one undoped, one In-doped and two Sn-doped) were also studied. The results are shown in figure 2.17. All of the four samples (undoped or heavily doped) show a region with flat transmission in the range from 0.55 to 0.8 μm however, the transmission value falls off rapidly for wavelengths below 0.5 μm. Reflection property of the sputtered ZnO films has not been studied in the present work.

2.4 CONCLUSIONS

Indium- and tin-doped ZnO films have been prepared on glass substrates by an rf magnetron sputtering technique using ZnO targets containing up to 10 wt% of In_2O_3 or SnO_2. The deposition experiments were carried out in an argon atmosphere (typical pressure 5 mTorr) without intentional heating of the substrates. Incident rf power used for most of the experiments was 60 W and the typical deposition time was

about 30 minutes (film thickness about 1 μm). It was found from electron probe micro analysis that the Sn-content in the films was roughly equal to that in the targets and the In-content in the films was smaller than that in the targets. Room temperature resistivity of the deposited films was found to decrease by about 3 orders of magnitude as the SnO_2 content was increased from 0 to 10 wt% and by 4 orders of magnitude as the In_2O_3 content was increased from 0 to 10 wt%. Using a target with 2 wt% In_2O_3, films have been prepared with different incident rf power and different argon pressure. Optical transmission data were also obtained for both In- and Sn-doped films. The transmission value at 0.7 μm was essentially unchanged for the In-doped films and that at 0.5 μm was affected by the presence of indium. For the Sn-doped films, the transmission value (both 0.5 and 0.7 μm) first decreased as the tin content was increased, reached minima at 5 wt.% SnO_2 and then increased as the tin content was further increased.

Tab 2.1 Results of In-doped Zinc Oxide Films.

Sample No.	In_2O_3/ZnO wt. %	No. of Interference Fringes	Thickness (μm)	Sheet Resistance (ohm/□)
ZnO-13	0	6	1.12	2.95×10^6
ZnO-14	0	6	1.12	1.76×10^5
ZnO-27	0.5	6	1.12	5.3×10^5
ZnO-28	0.5	6	1.12	1.4×10^5
ZnO-17	1	8	1.5	1.575×10^3
ZnO-18	1	5	0.94	9.45×10^2
ZnO-31	2	6	1.12	1.03×10^3
ZnO-32	2	6	1.12	5.35×10^2
ZnO-21	5	5	0.94	1.53×10^2
ZnO-22	5	5	0.94	8.8×10^1
ZnO-73	8	6	1.12	1.62×10^1
ZnO-74	8	6	1.12	2.025×10^1
ZnO-25	10	5	0.94	3.83×10^1
ZnO-26	10	5	0.94	4.05×10^1

* RF Power: 60 W.
** Ar Pressure: 5 mTorr.
*** Sputtering Time: 30 min. (ZnO-17, 43 min.).

Tab2.2 Results of Sn-doped Zinc Oxide Films.

Sample No.	SnO_2/ZnO wt.%	No. of Interference Fringes	Thickness (μm)	Sheet Resistance (ohm/□)
ZnSnO-3	0.5	6.5	1.21	8.055×10^3
ZnSnO-4	0.5	5	0.94	4.59×10^3
ZnSnO-7	1	5.5	1.03	1.8×10^3
ZnSnO-8	1	5	0.94	8.37×10^2
ZnSnO-11	2	6	1.12	5.22×10^2
ZnSnO-12	2	5.5	1.03	4.77×10^2
ZnSnO-15	5	6	1.12	5.31×10^2
ZnSnO-16	5	6	1.12	5.34×10^2
ZnSnO-31	7.5	6	1.12	4.9×10^2
ZnSnO-32	7.5	6	1.12	5.67×10^2
ZnSnO-18	10	6.5	1.21	5.85×10^2
ZnSnO-19	10	6	1.12	7.65×10^2

* RF Power: 60 W.
** Ar Pressure: 5 mTorr.
*** Sputtering Time: 30 min.

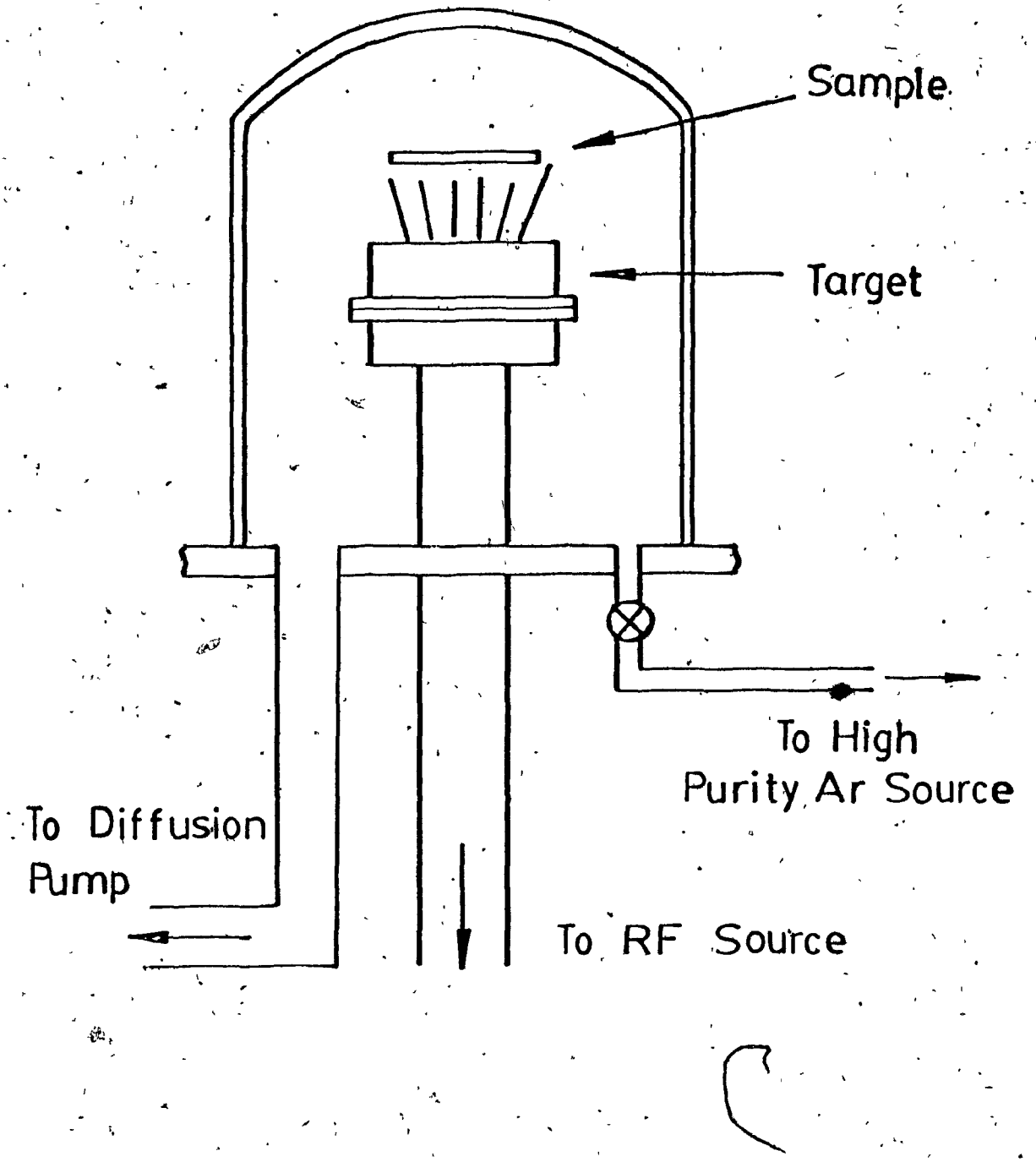

Fig. 2.1 Schematic diagram of an rf sputtering chamber.

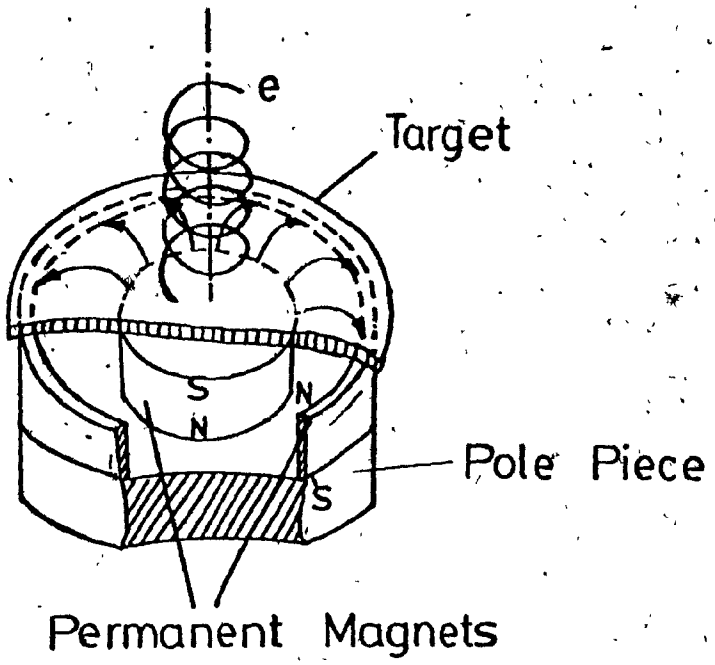

Fig. 2.2 Schematic diagram of a circular planar magnetron sputtering source (the curved lines represent magnetic field and the helix-like line represents the trajectory of the secondary electron).

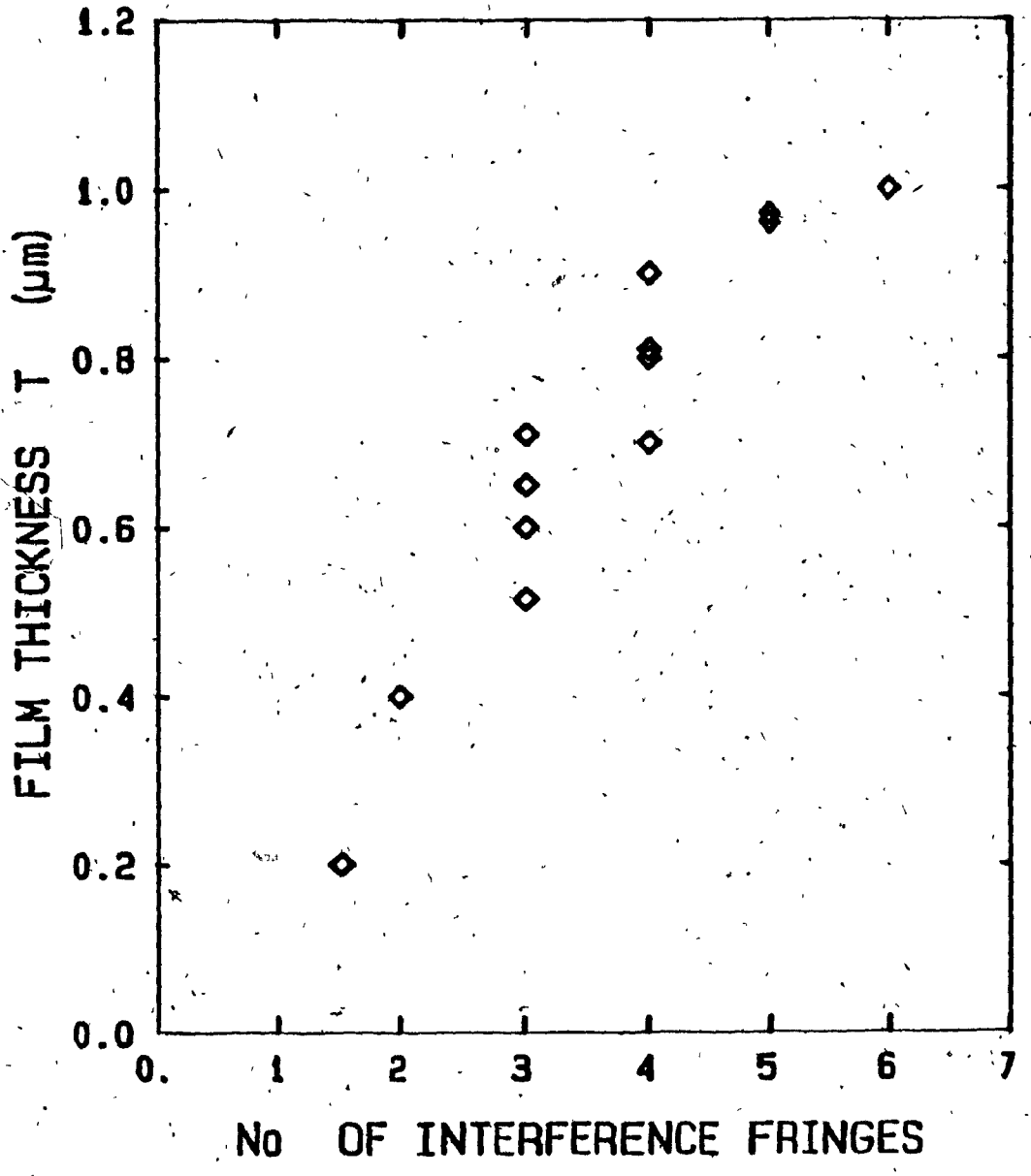

Fig. 2.3 Measured film thickness plotted against the number of interference fringes observed under an optical microscope.

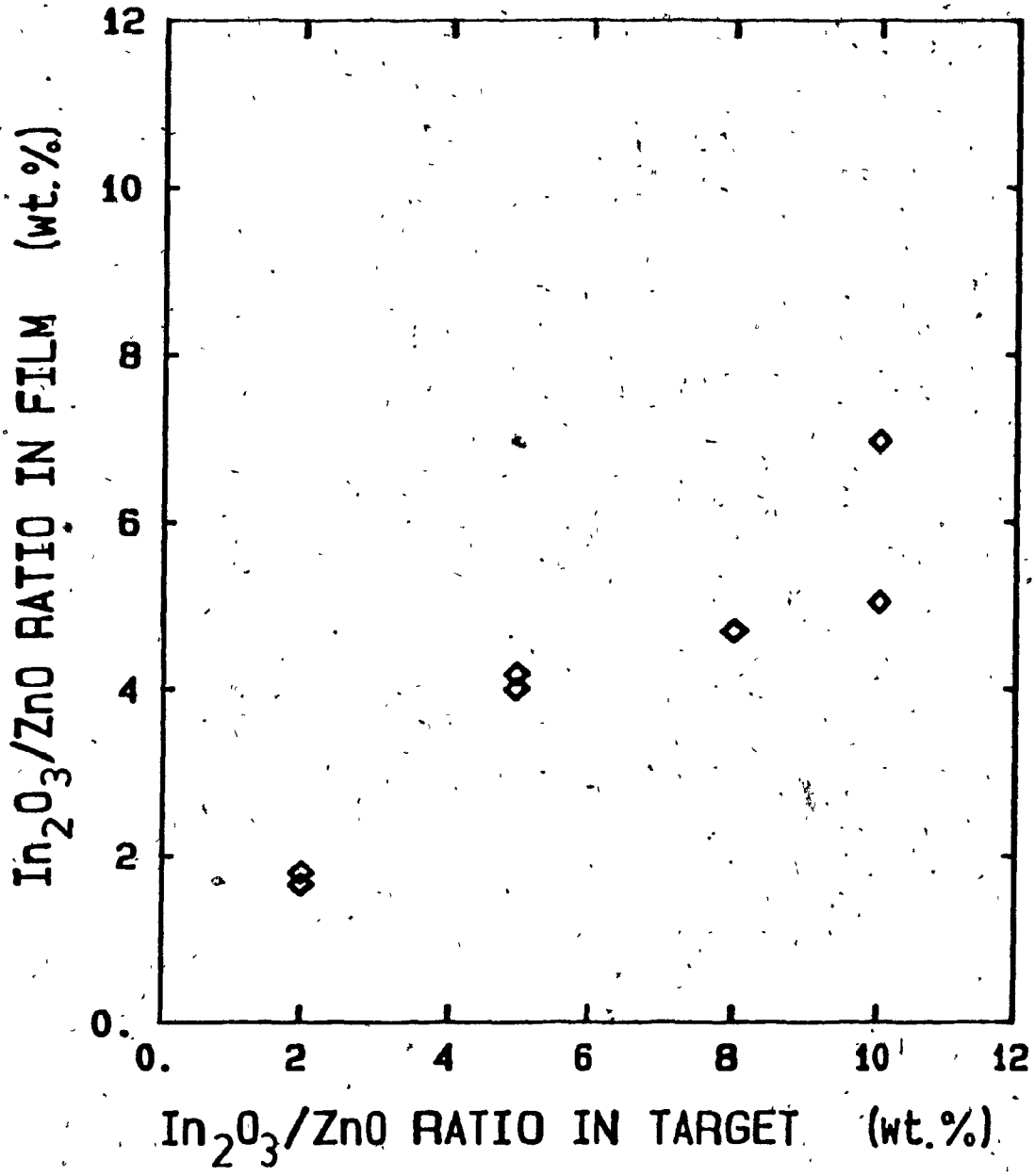

Fig. 2.4 In_2O_3/ZnO ratio in the film plotted versus that in the target.

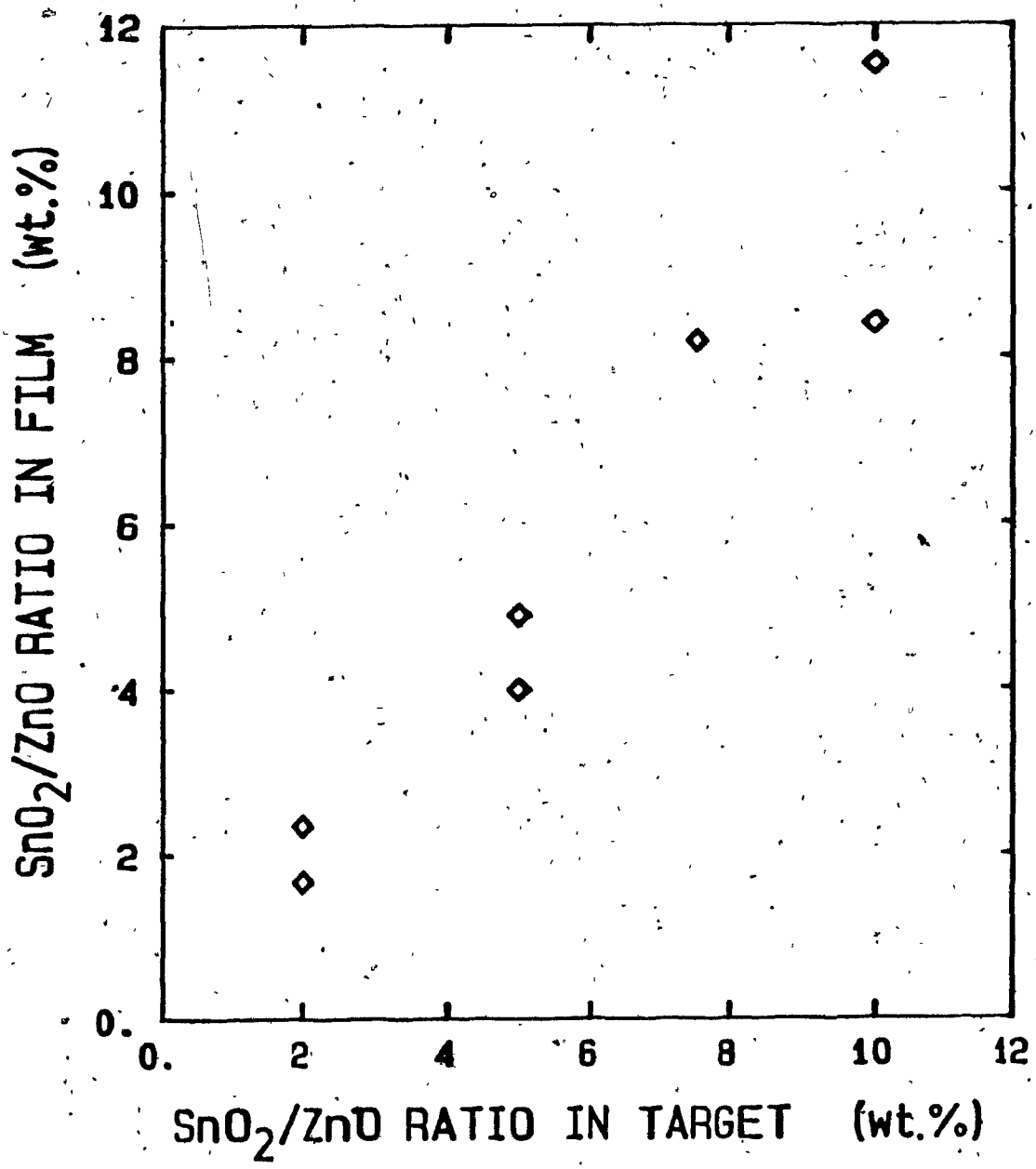

Fig. 2.5 SnO_2/ ZnO ratio in the film plotted versus that in the target.

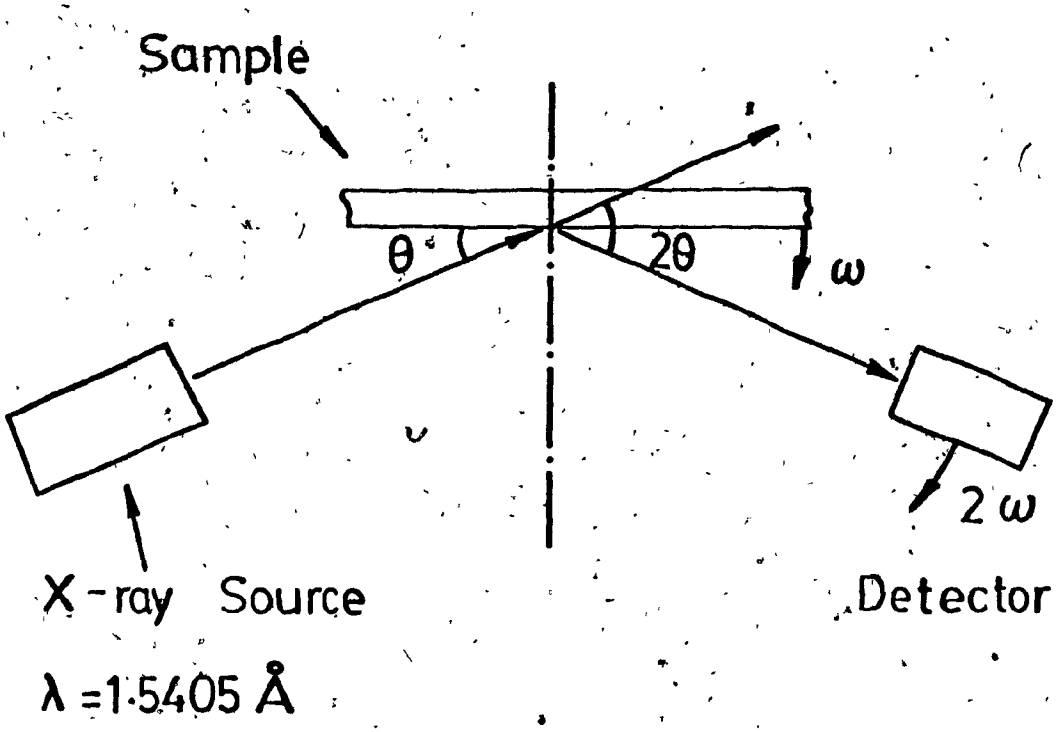

Fig. 2.6 Schematic diagram of the X-ray diffraction system.

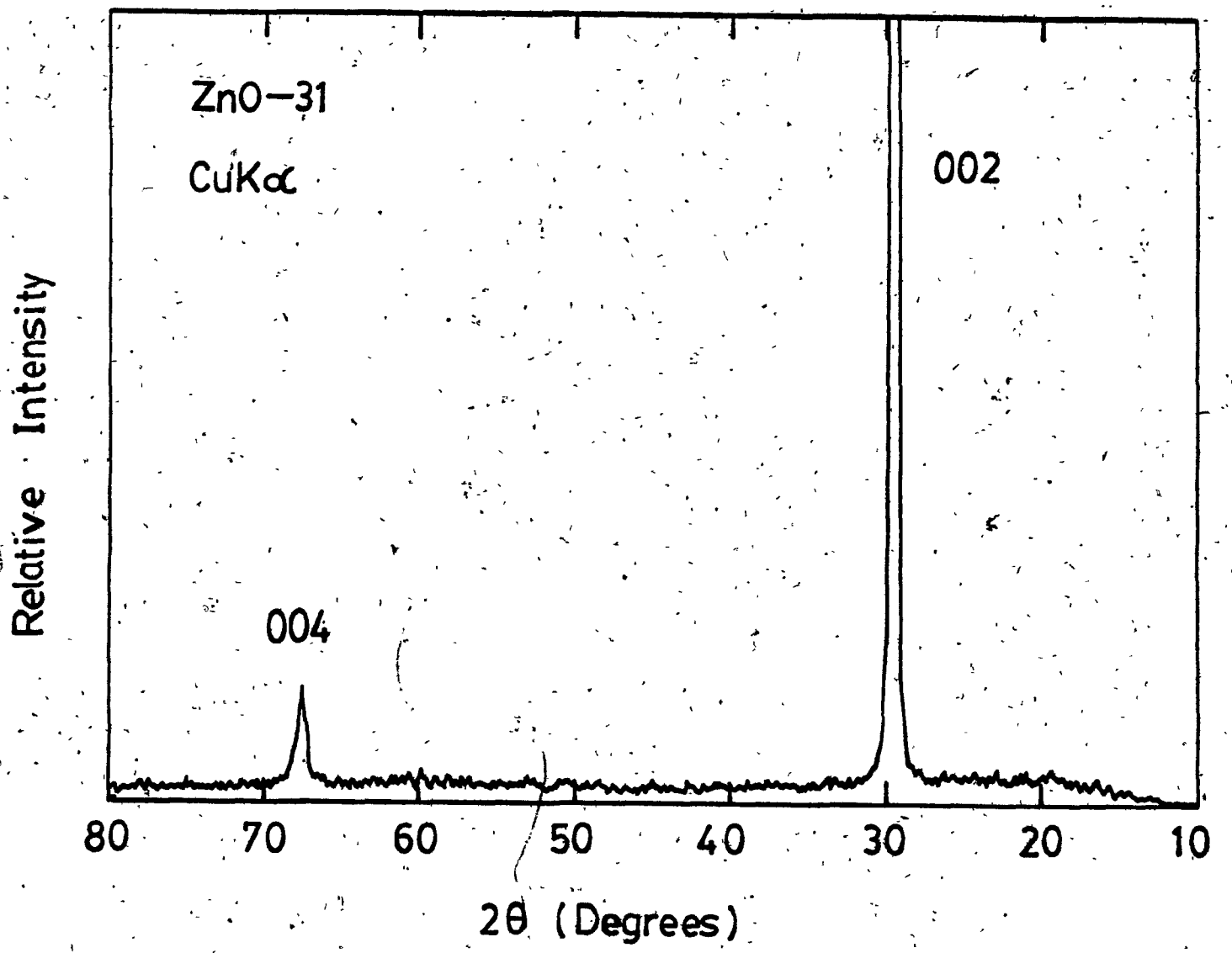

Fig. 2.7 Relative X-ray intensity versus 2θ for an In-doped ZnO sample (2% In_2O_3 in the target).

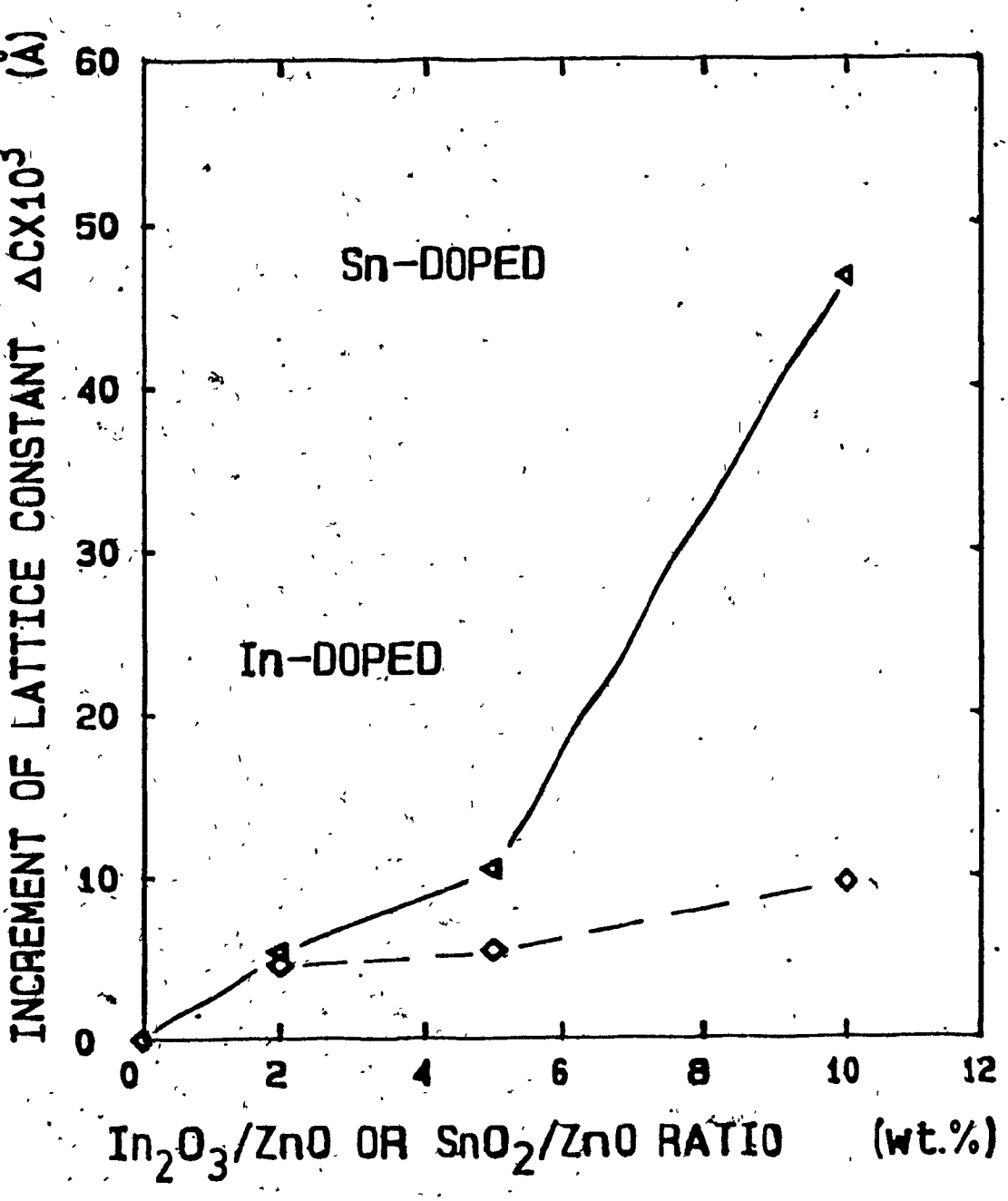

Fig. 2.8 Increment of lattice constant ΔC versus the In_2O_3/ZnO or SnO_2/ZnO ratio in the target.

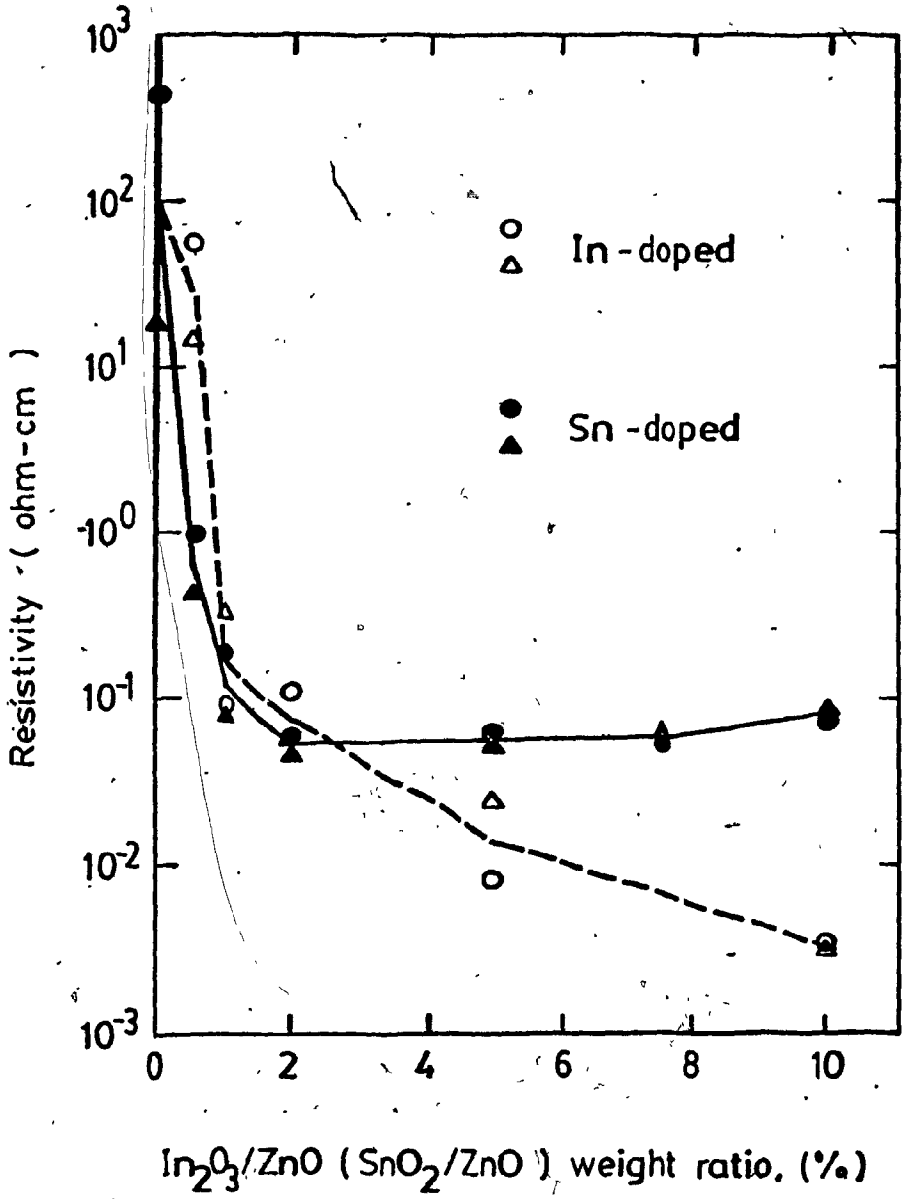

Fig. 2.9 Dark resistivity of ZnO films versus doping concentration in the target.

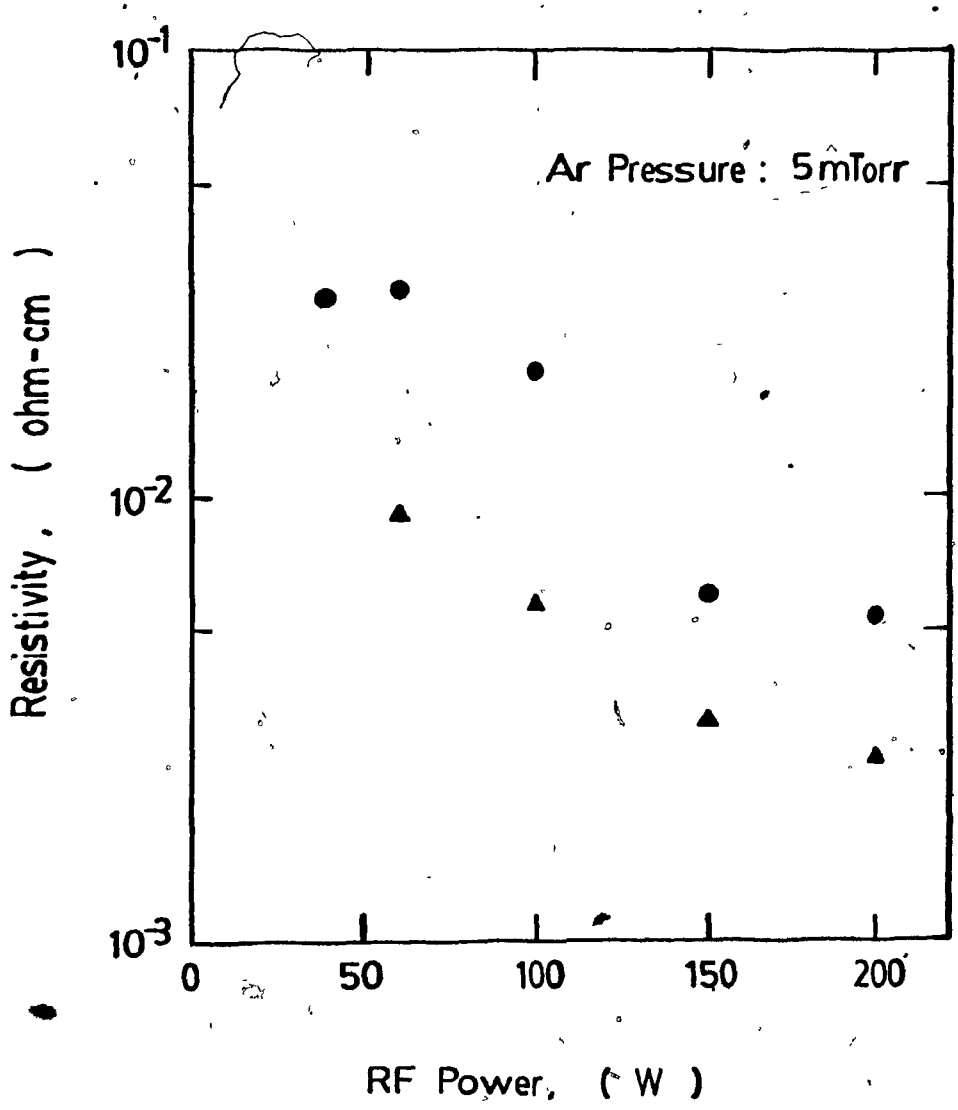

Fig. 2.10 Dark resistivity of ZnO films as a function of incident rf power at a fixed Ar pressure.

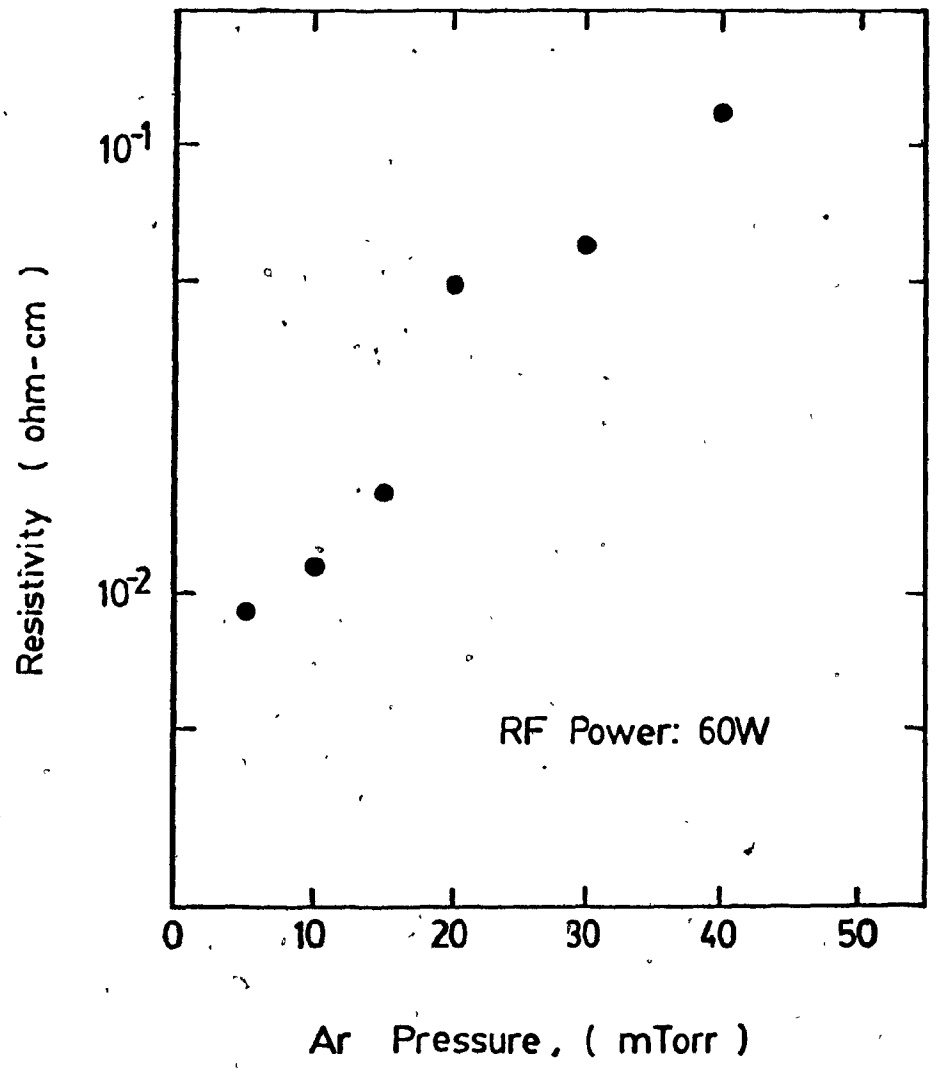

Fig. 2.11 Dark resistivity of ZnO films as a function of Ar pressure at a fixed rf power.

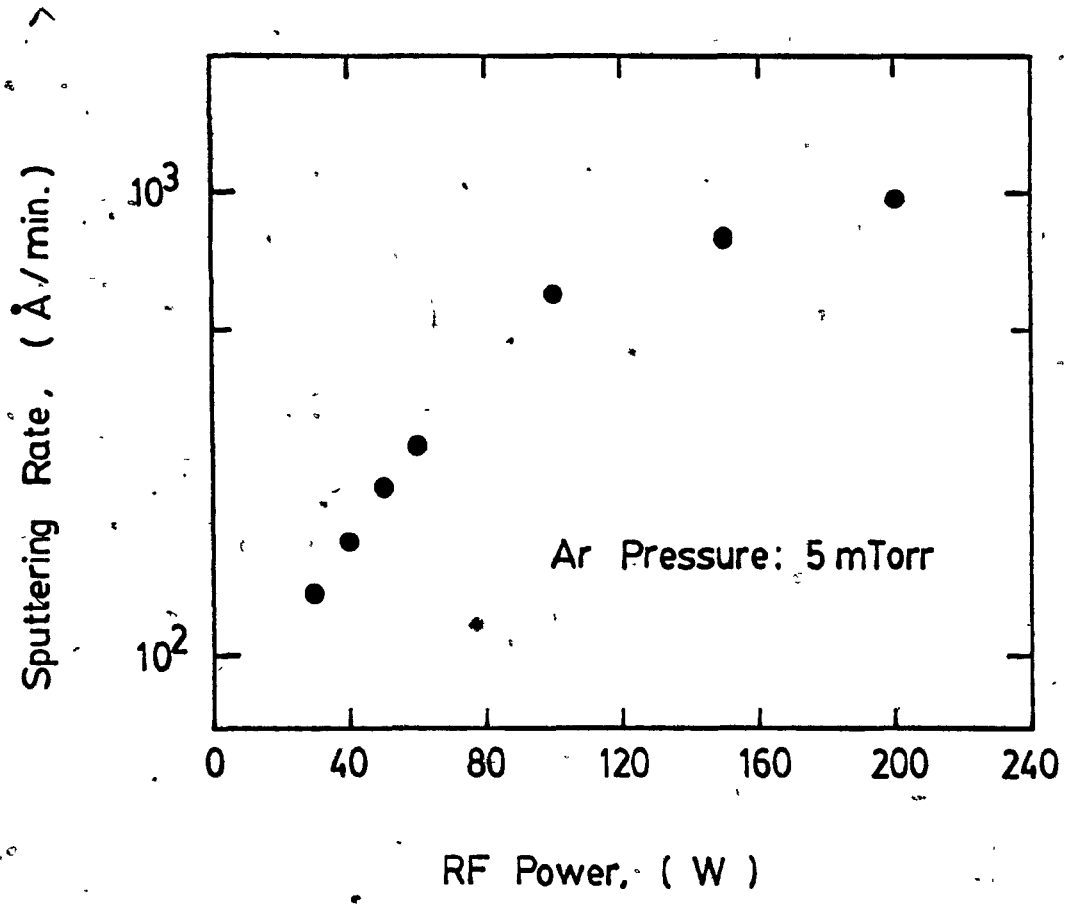

Fig. 2.12 Sputtering rate of ZnO films as a function of incident rf power at a fixed Ar pressure of 5 mTorr.

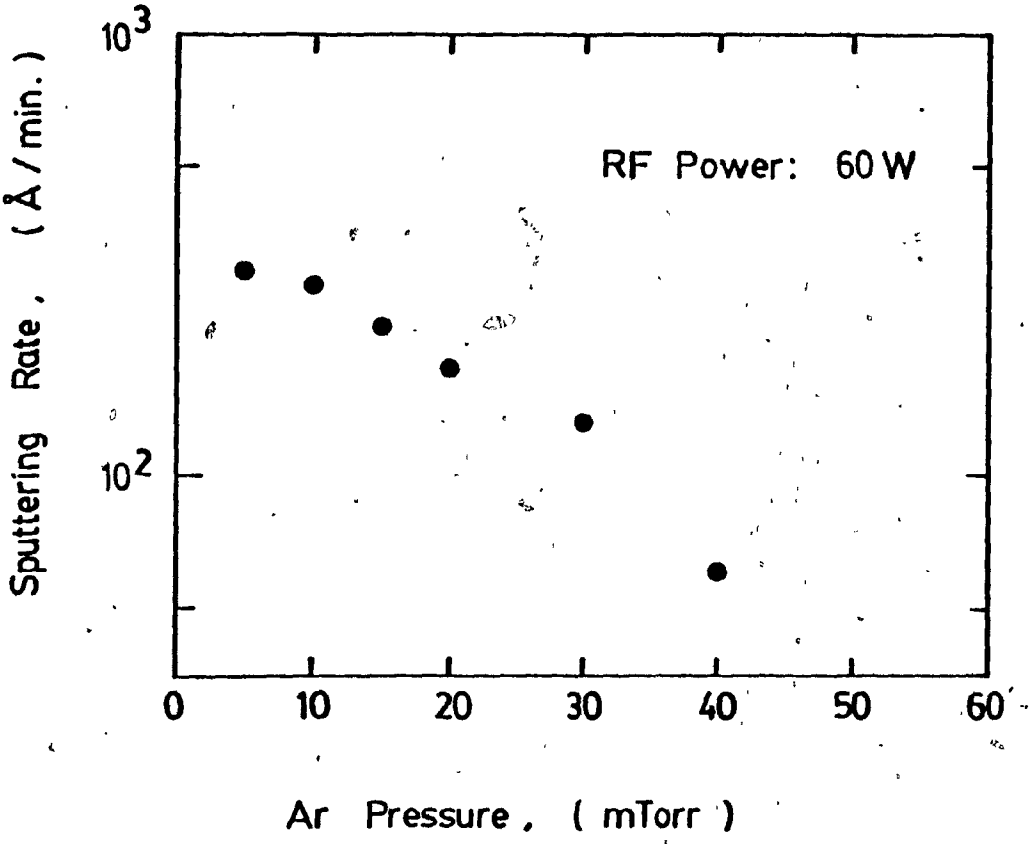

Fig. 2.13 Sputtering rate of ZnO films as a function of Ar pressure at a fixed incident rf power of 60 W.

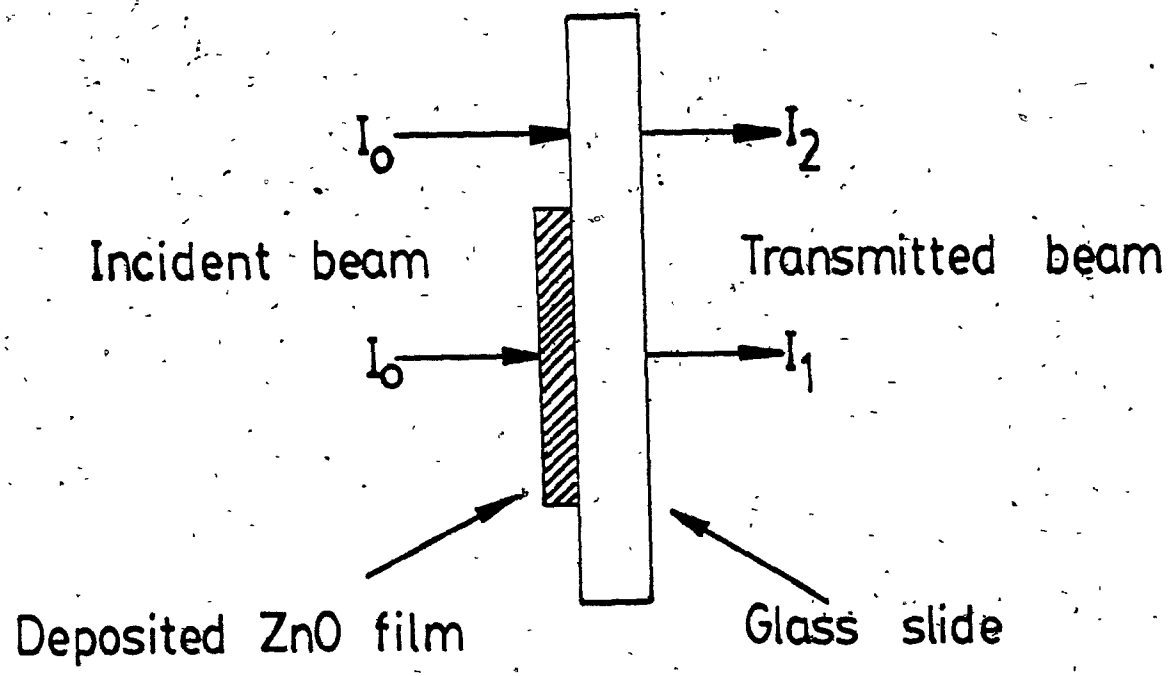

Fig. 2.14 Set-up for the transmission measurements. Here I_o is the monochromator output intensity. I_1 and I_2 are the transmitted light intensities for ZnO film coated glass and the uncoated one, respectively.)

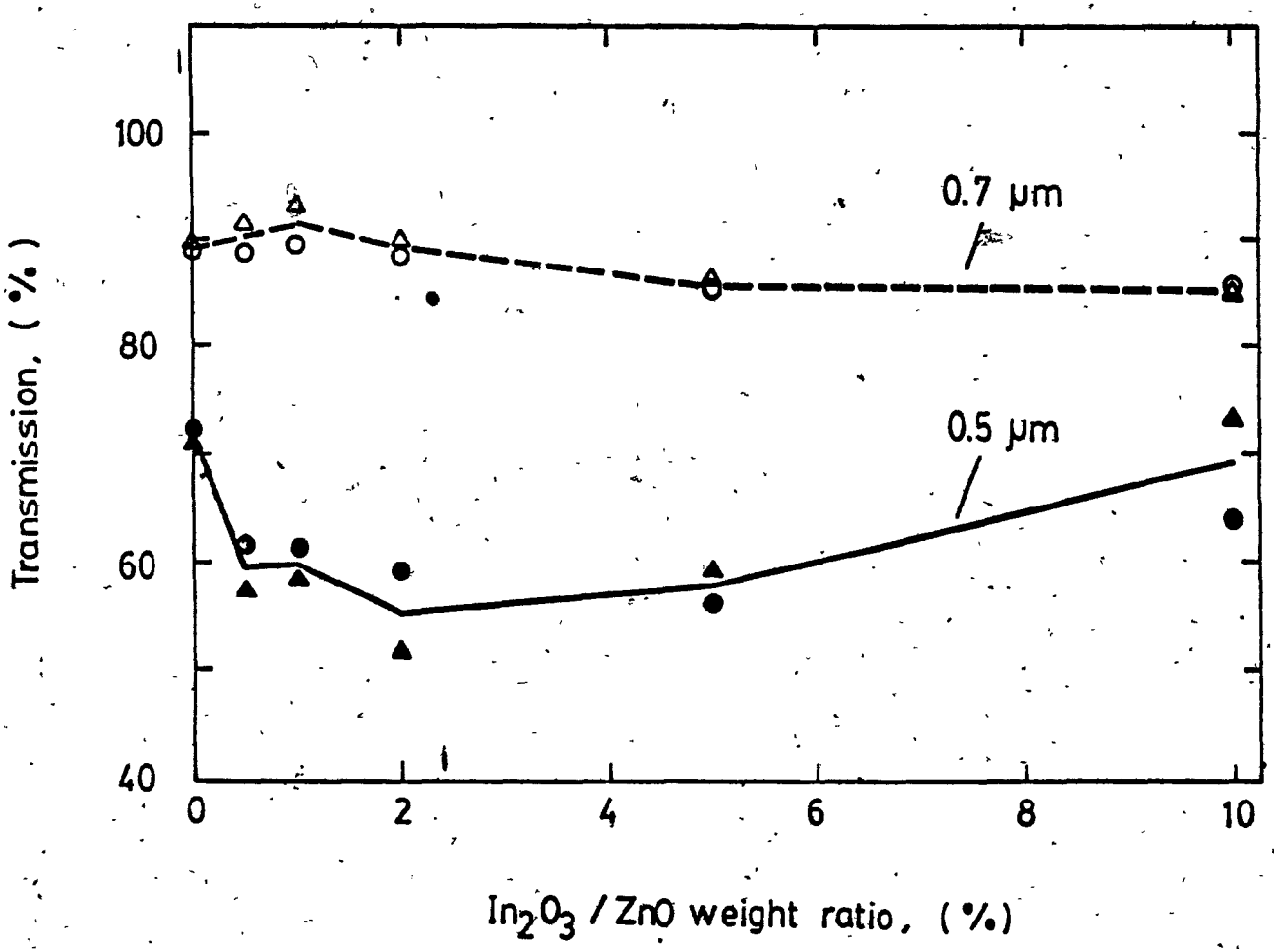

Fig. 2.15 Optical transmission of ZnO films at wavelengths of 0.5 and 0.7 μm plotted versus the indium oxide content in the target.

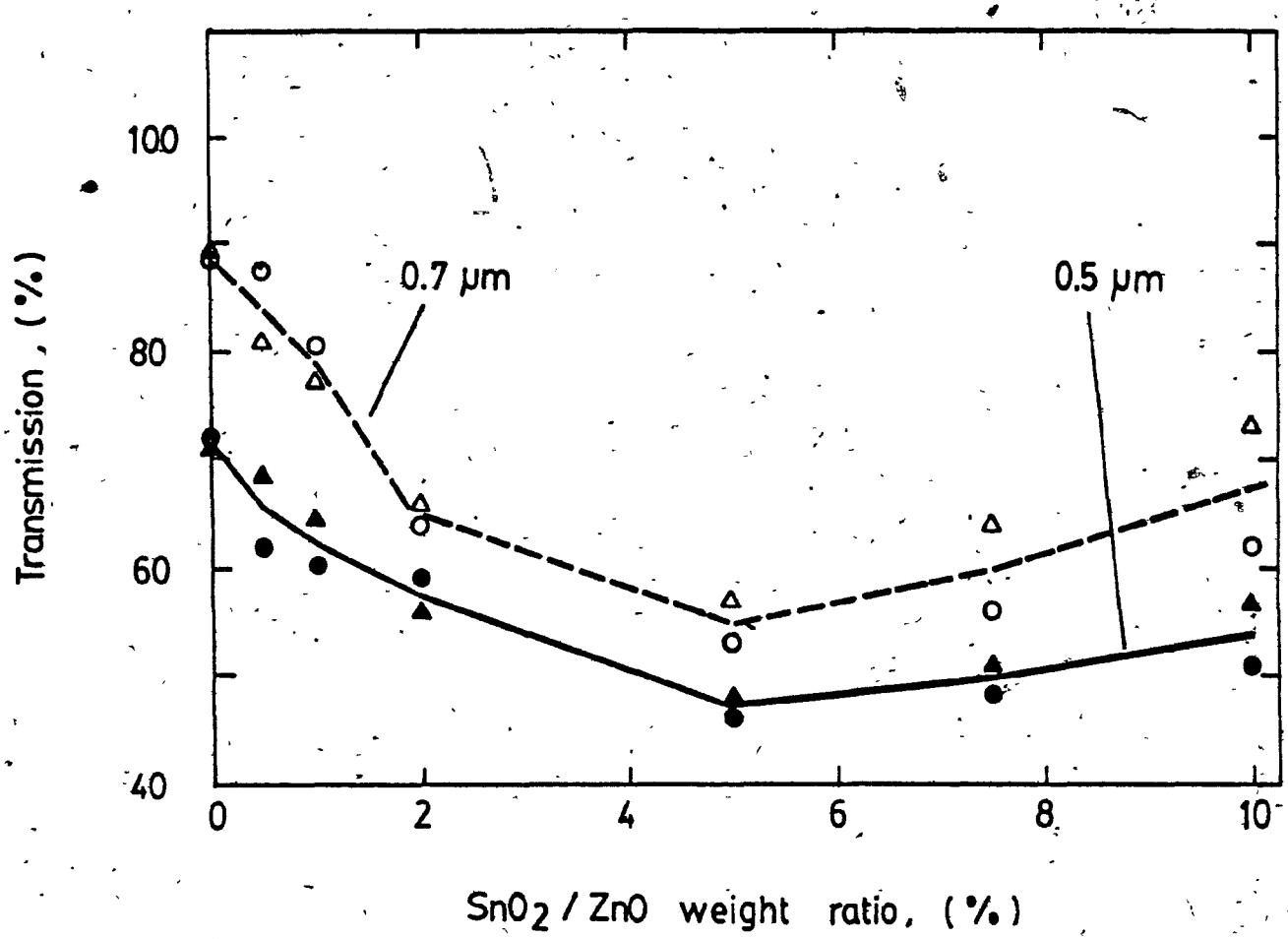

Fig. 2.16 Optical transmission of ZnO films at wavelengths of 0.5 and 0.7 µm plotted versus the tin oxide content in the target.

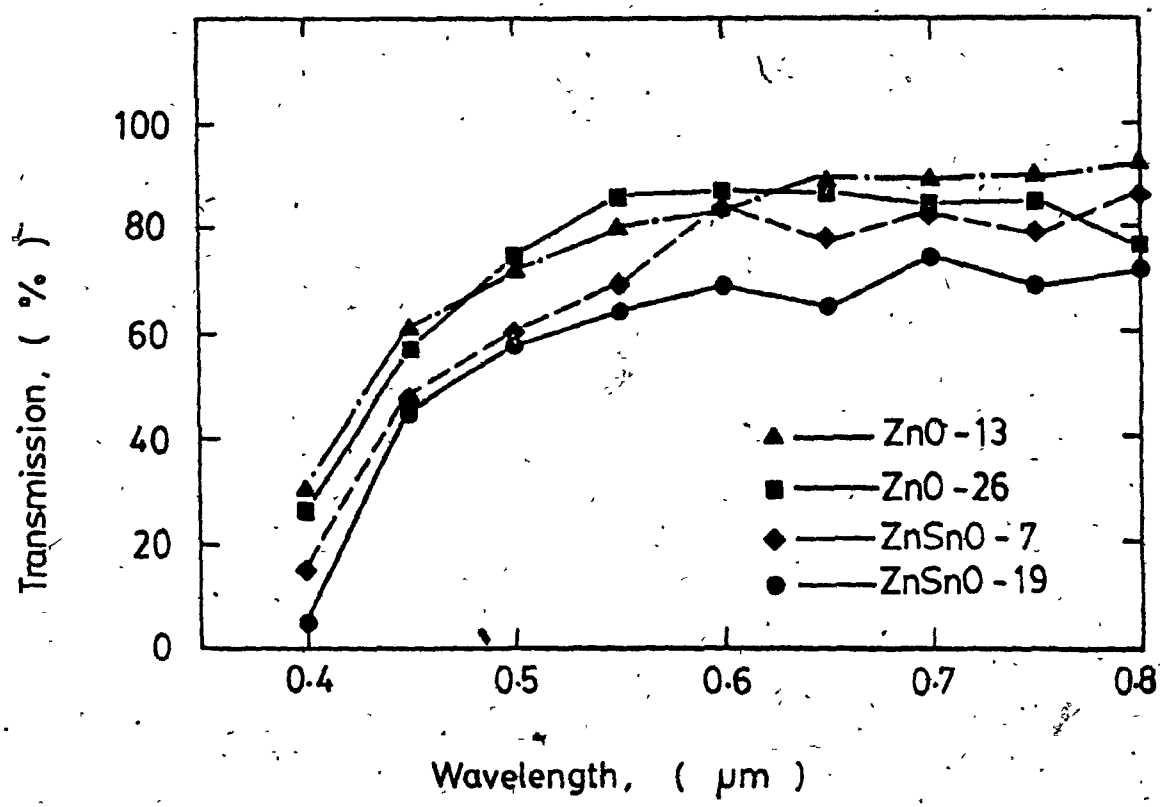

Fig. 2.17 Optical transmission of ZnO films as a function of wavelength.

CHARTER 3 CHARACTERISTICS OF $ZnO/CuInSe_2$ HETEROSTRUCTURES

3.1 INTRODUCTION

In the past few decades, many research activities have been done on investigation of semiconductor heterojunctions since there are many applications, especially for photovoltaic cells. Among these heterojunctions, structure of the form Ge/GaAs was the first one to be constructed with the band diagram proposed by R.L. Anderson [3.1]. From then on, many other heterostructures have been studied.

Copper indium diselenide is a promising photovoltaic material which has been studied intensively recently. A $CdS/CuInSe_2$ cell with a conversion efficiency over 12% [3.2] has already been fabricated, making this material a promising thin film solar cell candidate. However, $CuInSe_2$-based devices with other window materials are also interesting. Recently thin film heterojunctions of the form $ZnO/CuInSe_2$ have been reported by Tomar and Garcia [3.3] using a spray pyrolysis technique. Their devices showed a relatively large photocurrent density under AM1 illumination condition and were sensitive to light in a wavelength range from 0.4 to 1 μm. From their results, it appears that ZnO is one of the potential window materials for $CuInSe_2$-based solar cells.

Zinc oxide is a large band gap semiconductor which can be produced in a highly conducting thin film form by controlling the film stoichiometry and by impurity doping [2.10]. As described in chapter 2, indium doped ZnO thin films with a relatively low resistivity can be prepared by using a sputtering technique. Using such technique, ZnO film was sputtered on a monocrystalline $CuInSe_2$ sample to form a heterojunction. For the ZnO/$CuInSe_2$ structure, current transport mechanisms appear not to have been reported in literature. It is therefore interesting to investigate the current-voltage characteristics and to construct an energy band diagram for this heterostructure. In this chapter, simple heterojunction theories are first reviewed. Device fabrication processes and measurement techniques are then described. I-V and C-V characteristic results for both p-n and n-n structures are reported. Using electron affinity difference rule, theoretical energy band diagrams have also been established for the ZnO/$CuInSe_2$ heterojunctions.

3.2 HETEROJUNCTION THEORIES

A junction formed between two different semiconductors is called a heterojunction. It can be an isotype heterojunction (n-n or p-p) if the conductivity type of the two semiconductors is the same, or an anisotype one (p-n or

n-p) in which the conductivity type is different in the two semiconductors. To form a good quality heterojunction, the mismatch of lattice constant and thermal expansion coeffecients of the two materials should be as small as possible since it will introduce dislocations at the heterojunction interface and give rise to interface states. To reduce the energy discontinuities in the conduction band and the valence band as a spike or notch, the electron affinities of the two semiconductors should be close.

3.2.1 Semiconductor p-n Heterojunction Models

Several models for current transport in heterojunctions have been developed in the past decades. Of them Anderson's model, shown in figure 3.1, is the fundamental one which considers the current flow to be ideal diffusion or injection over the conduction or valence band barriers. In this model, it is assumed that no interface states exist. This could be a good approximation only when the difference of lattice constant between two materials is small enough ($<<1\%$) and the difference in the expansion cpefficient is small. The difference in energy of conduction band edges in the two semiconductors, or electron affinity difference, is represented by ΔE_C and that in the valence band edges by ΔE_V (both are invariant with doping for nondegenerate materials),

as shown in figure 3.1 (a). Figure 3.1 (b) shows the band diagram of a heterojunction formed between the two semiconductors in figure 3.1 (a). The total diffusion voltage V_D is defined as the difference in the work functions of the two materials. Because of the discontinuity in the valence band edge at the interface, the energy band barrier to holes flow is much larger than that to electrons flow. Therefore, the predominant current carriers are electrons. The current-voltage relationship, in the absence of recombination current is given by,

$$I = A\exp(-qV_D^2/KT)[\exp(qV_2/KT)-\exp(-qV_1/KT)] \quad (3.1)$$

where $A=aqXN_{D2}(D_{n1}/\tau_{n1})^{1/2}$, with X being transmission coefficient for electrons across the interface, a is the junction area, and D_{n1} and τ_{n1} the diffusion coefficient and lifetime of minority carriers, respectively, in the p-type material.

Rediker et al [3.4] have proposed a model for an abrupt anisotype heterojunctions where electrons have to surmount or tunnel through the potential barrier in the n-type wide band gap material to flow from n-type to p-type region or vice versa. If tunneling through the barrier greatly exceeds thermal emission over the barrier, then

$$I=I_s(T)\exp(V/V_o) \quad (3.2)$$

where $I_s(T)$ is a weakly increasing function of temperature.

Dolega [3.5] has discussed the recombination model assuming a lifetime approaching zero at the interface. He found that the dark forward current was proportional to $\exp(qV/nkT)$, where n ranges from 1 to 2 depending on the ratio of the impurity concentrations. And it can be shown that for a heterojunction with large lattice mismatch (>1%) the interface states will dominate the current flow mechanism. There seems very little prospect for an acceptable injection efficiency for such a junction.

3.2.2 Capacitance Study of Anisotype Heterojunctions

Applying Anderson's equation with the assumption of abrupt junction and uniform doping in two materials, the capacitance per unit area as a function of applied voltage, V is given by,

$$C=\left[\frac{qN_{D1}N_{A2}\varepsilon_1\varepsilon_2\varepsilon_o}{2(\varepsilon_1N_{D1}+\varepsilon_2N_{A2})(V_D\pm V)}\right]^{1/2} \quad (3.3)$$

Where N_{D1}, N_{A2} are net ionized impurity concentrations and ε_1, ε_2 are dielectric constants in the two materials, respectively. From the above equation, a linear relationship

between $1/C^2$ and the applied voltage should be obtained and the slope of the line can be written as,

$$d(1/C^2)/dV=2(\varepsilon_1 N_{D1}+\varepsilon_2 N_{A2})/(qN_{D1}N_{A2}\varepsilon_1\varepsilon_2\varepsilon_o) \quad (3.4)$$

For one-side heterojunctions ($N_{D1}>>N_{A2}$ or $N_{A2}>>N_{D1}$), the carrier concentration of the lightly doped-side can be obtained from this equation. When the applied forward voltage is equal to the diffusion potential V_D, the band bending will no longer exist (flat-band condition), and the capacitance becomes infinity. Therefore, the extrapolation of the $1/C^2$ curve versus V to abscissa gives the value of V_D.

For the junctions which have perfect interface, the value of V_D taken from capacitance measurements is in good agreement with that expected from calculation of the work function. However, there is some evidence that the barriers measured may be different from the cacylated results if the interface states are present. The effect of interface states on the capacitance of p-n junctions has been studied by Donnelly and Milnes [3.6]. They found that the apparent diffusion voltage, V_{Di}, obtained by extrapolating the slope of $1/C^2$ at low reverse bias and forward bias back to abscissa is given by,

$$V_{Di} = V_D - \chi_m - [Q_{is}^2/2q(\varepsilon_1 N_1 + \varepsilon_2 N_2)] \quad (3.5)$$

where Q_{is} is the charge per unit area associated with interface states, and χ_m represents a dipole effect. Electric dipole effects caused by interface states being dipolar and distributed in space on either side of the junction were first discussed by Van Ruyven et al in 1965 [3.7]. Since the concept of electric dipole effect has not been greatly explored with respect to heterojunctions, the actual values of Q_{is} and χ_m can not be obtained although equation (3.5) has provided a possibility of measuring interface state parameters by capacitance measurements.

3.2.3 Isotype Semiconductor Heterojunctions [3.8]

In an n-n heterojunction, the conduction band barrier is determined by the electron affinity difference for the two semiconductors ($\Delta E_c = \chi_2 - \chi_1$) and by the doping levels of the semiconductors if there are no interface states. A typical energy band diagram in absence of interface defects is shown in figure 3.2(a) where a barrier V_{D2} exists in the conduction band for electron flow from 2 to 1. Similarly, in a p-p heterojunction a barrier to hole movement exists in the valence band as shown in figure 3.2(b). Both structures (proposed by Anderson [3.1]) can act as rectifiers.

In heterojunctions formed from two materials with

different lattice constants, dislocations will occur at the interface in order to compensate for the lattice mismatch. Interface states resulted from dislocations at the interface will have a dominant effect on the barrier in isotype heterojunctions. Usually only the net charge on these states will affect the energy band diagram. It is not improbable, however, that the defects at the interface will create electric dipoles which will produce a quasi discontinuity in the electrostatic potential. Electric dipole, for this reason, has the same effect as the difference in electron affinity. Depending on the strength of the dipole, the energy band diagram might become more dependent on fabrication teqniques than on work function difference.

Considering an n-n heterojunction with the presence of the interface states, the energy bands at the interface are free to move up (or down) with the necessary charge being supplied by electrons (or their absence) in the interface states. Figure 3.3 shows examples presented by Donnelly and Milnes [3.9]. Junction 2 in Fig.3.3 (a) shows two depletion regions at both side while junctions 1 and 3 show depletion regions only in lightly doped side. A device with double depletion regions may display rectification in either direction. Typical I-V characteristics which correspond to the energy band diagrams of figure 3.3 (a) are given in figure 3.5 (b). As expected, diode 2 shows current saturation

in both directions, and a voltage direction for easy current flow in diodes 1 and 3 exists. The optical properties of the n-n Ge/Si heterojunction, shown in figure 3.5 (c), also have been studied by Donnelly and Milnes. The polarity of the optical response changes when wavelength is changed for diodes 2 and 3. This is due to the photoexcitation of the electrons from different side of the junction.

3.3 DEVICE FABRICATION PROCESSES

Monocrystalline p-type $CuInSe_2$ samples were selected from Bridgman grown ingots and polished using 0.3 μm alumina powder to give a mirror-like surface. For these samples, an effective carrier concentration of 10^{16} cm^{-3} and a room temperature mobility value of about 50 cm^2/V-sec have been reported from Hall effect measurements [3.10]. N-type $CuInSe_2$ samples were also prepared with a comparable effective carrier concentration. Using the rf sputtering system described in chapter 2, a layer of indium-doped ZnO was then deposited on the polished $CuInSe_2$ surface. A ZnO target containing 2 wt% In_2O_3 was used for the sputtering. The deposition experiments were carried out under an argon atmosphere with a pressure of about 5 mTorr and an incident rf power of 60 watts. Using the above described conditions, several devices have been fabricated and the typical ZnO film

thickness was found to be about 0.5 μm for a deposition time of 20 minutes. An aluminum mask with a circular window of 2.5 mm diameter was used to define the deposited ZnO area. A schematic cross sectional view of the fabricated device is shown in figure 3.4. During the deposition, a glass substrate was placed side by side with the $CuInSe_2$ sample to prepare a film for parameter testing. Since samples prepared by rf magnetron sputtering technique (under the conditions: 60 W, 5 mTorr, 20 minutes) were not intentionally heated during deposition (temperature of the samples about 60 ^{o}C), the thermal expansion difference is believed to be small in the present experiments.

Hall effect measurements, as described in chapter 2, were carried out at room temperature for two ZnO samples deposited on the glass substrates (magnetic flux density was 0.2 tesla). The Hall mobility value was found to be 4 cm^2/V-sec and the electron concentration about 10^{20} cm^{-3} from the present results. After the ZnO film deposition, a circular indium area (diameter about 1 mm and 1 μm thick) was then evaporated through a second aluminum mask. The device was finally mounted on an aluminum holder using silver epoxy. A short heat treatment of about 10 minutes at 140 ^{o}C was done on the samples to harden the silver epoxy.

The effect of the indium top contact to the ZnO film

was determined by observing the current-voltage characteristics of two ZnO films deposited on glass substrates, with three circular indium areas evaporated on each of them. Figure 3.5 shows the I-V characteristics between the circular indium areas. It is noted that both curve 1 and 2 are straight lines with different slopes. The resistivity value obtained from figure 3.5 was roughly equal to that obtained from four-point probe measurements, confirming the low resistance characteristics of the In/ZnO contacts.

3.4 MEASUREMENT TECHNIQUES

The fabricated ZnO/$CuInSe_2$ junction was mounted in a cryostat and the dark current-voltage characteristics at temperatures between 200 and 300 K were measured using an HP model 4145A semiconductor parameter analyzer. The input impedance of the analyzer was 10^{14} ohms, so that the loading effect was negligible in these experiments. Illuminated I-V characteristics were also measured using the same instrument. A tungsten lamp was used to provide an approximate AM1 illumination condition.

Differential capacitance of the junction was also determined at room temperature using an HP model 4274A multi-frequency LCR meter with an IBM computer. Samples were

maintained under the dark condition throughout the measurements and the LCR meter was set to the parallel function mode with the ac signal amplitude of about 20 mV. The range of dc voltage applied across the junctions was from 0 V to -3 V for the ZnO(n)/$CuInSe_2$(p) junctions and -3V to 3V for the n-n junctions. The connecting wires to the instrument were kept to be short so that the stray capacitance was small. Several frequencies (in the range from 100 Hz to 100 kHz) were used during the measurements and the results taken at 100 kHz were adopted for the diffusion voltage study.

The spectral variation of the open circuit voltage of the device was observed using a Beckman model 2400 monochromator in the wavelength range from 0.4 to 1.6 μm. An HP model 3468A multimeter with an input impedance of 10^{10} ohms, which is large enough to minimize the loading effect, was connected across the p-n heterojunction to measure the open circuit voltage. A lock-in voltmeter, HP model 3462A, was used to obtain the smaller V_{oc} value for the n-n junctions. The incident light intensity at the frequency range was determined by replacing the sample with a silicon detector (United Technology model PIN 6DP). The normalized V_{oc} was then obtained by dividing the measured V_{oc} by the light intensity.

3.5 EXPERIMENTAL RESULTS

3.5.1 ZnO(n)/$CuInSe_2$(p) heterojunctions

(1) I-V Characteristics

Dark forward current-voltage characteristics of one of the fabricated ZnO(n)/$CuInSe_2$(p) heterojunctions at different temperatures are shown in figure 3.6. At room temperature, the device current shows an ideality factor of about 2.8 in the intermediate voltage region. As the temperature is decreased, the I-V characteristics show two competing current transport processes. In the low voltage region, the current could be controlled by a shunting of the junction or a tunneling and recombination process which is not very sensitive to the temperature variation. In the intermediate voltage region, the current appears to increase exponentially with increasing voltage. The transition voltage for the two regions is seen to increase as the temperature is decreased.

(2) C-V Characteristics

In order to get an idea about the energy band diagram of the heterojunction, differential capacitance measurements have been made on the devices. Since the effective carrier

concentration in the ZnO films, obtained from Hall effect studies, was much larger than that for $CuInSe_2$ substrate, the differential capacitance measurements provided material information mainly for the $CuInSe_2$ side of the junction. Figure 3.7 is a plot of $1/C^2$ versus reverse bias voltage, V_R, at a frequency of 100 kHz. From the curve, the apparent diffusion potential was estimated to be about 2 volts*, which is larger than the difference in work functions, 0.8 V. And the effective ionized impurity concentration in the p-type $CuInSe_2$ near the junction given by the slope of the $1/C^2$ versus V_R curve was about 4×10^{15} cm^{-3}. Similar results have been obtained from two other devices. The slope discontinuity in the $1/C^2$ versus V_R plot at 0.5 volt could be due to deep levels in crystalline $CuInSe_2$ [3.11]. The ionized impurity concentration of 4×10^{15} cm^{-3} obtained from figure 3.7 is about one order of magnitude less than that measured for the p-type bulk $CuInSe_2$ samples [3.10].

* This value was obtained by extrapolating the curve for $|V_R| > 0.5$ volt. A slightly small value of diffusion potential could be obtained if in figure 3.7 extrapolation is done with the initial slope (ie below $|V_R| = 0.5$ volts).

(3) Energy Band Diagram

Using the electron affinity rule and assuming that the net charge is equal to zero, an energy band diagram of the ZnO(n)/$CuInSe_2$(p) system has been constructed according to the material parameters for both ZnO and $CuInSe_2$ (see table 3.1). This was done in order to determine the possible reasons for the large apparent barrier height. The constructed energy band diagram is shown in figure 3.8. Since the electron affinity of ZnO is very close to that for $CuInSe_2$, the conduction band discontinuity, ΔE_c, is small (not shown in figure) and the valence band discontinuity is large and is essentially equal to,

$$\Delta E_v = E_g(ZnO) - E_g(CuInSe_2) = 2.3 \text{ eV}$$

The total band bending, qV_D, from the diagram is about 0.8 eV which is not sufficient to produce the large apparent barrier height observed from the C-V measurements. For ZnO/$CuInSe_2$ heterojunctions with large lattice mismatch (>40%), a very large density of interface states (Q_{is}) is expected [3.12]. It can be seen (from figure 3.9) that when interface states of an abrupt p-n heterojunction are filled with holes (by absence of the electrons), the space charge distribution will change (by the requirement that the net

charge be equal to zero) so that the area under the curve of electric field distribution is smaller than the one when interface states are not included. Therefore, the apparent diffusion potential is smaller than the work function difference. It also can be shown that negatively charged interface states will affect the band structure in a similar way. It has been proposed [3.6] that the measured apparent diffusion voltage V_{Di} of a junction can be related to the value of V_D assuming a finite value of Q_{is} and a finite value of χ_m which represents an electric dipole effect,

$$V_{Di} = V_D - \chi_m - [Q_{is}^2 / 2q(\varepsilon_1\varepsilon_o N_1 + \varepsilon_2\varepsilon_o N_2)].$$

Here q is electronic charge, N_1 and N_2 are the net ionized impurity concentration values in ZnO and $CuInSe_2$ and ε_1 and ε_2 are the dielectric constants in the two materials. Since the presence of interface states (occupied by electrons or holes) will only reduce the apparent diffusion potential, V_{Di} (as described before), a strong dipole effect seems to be needed to account for the high apparent V_{Di} of the devices. From the above equation, the value of χ_m must be negative for the present case. This suggests that the dipole has the same dipolar direction with the space charge and therefore enlarges the diffusion potential. Since the amount of the electron dipole is unknown, density of interface states can not be obtained in the present case.

From the band diagram shown in figure 3.8, it is seen that because of the large discontinuity in the valence band the barrier height for holes is much larger than that for electrons. Therefore, the hole emission current over the large barrier in the ZnO/$CuInSe_2$ heterojunctions can be neglected. At temperatures near to room value, it appears that emission of electrons and recombination at interface states (processes 1 and 2 in figure 3.8) are the dominant current transport processes. As the temperature is decreased, the emission and recombination current value decreases and the third current transport process becomes relatively important in determining the device current in the low voltage range. It is believed that tunneling of holes from the valence band of $CuInSe_2$ to the interface states (process 3, figure 3.8) is responsible for the device current which is not very sensitive to the temperature decrease. It is also noted from figure 3.6 that the rate of current decrease with temperature in the intermediate voltage region is less than that for an p-n $CuInSe_2$ homojunction, which will be reported in chater 4.

(4) Photoresponse

Under an approximate AM1 illumination condition, the devices showed an open circuit voltage of about 0.2 volt and a short circuit photocurrent density of about 5 mA/cm^2, (see

figure 3.10). Spectral variation of open circuit voltage of one of the devices is shown in figure 3.11. It is seen that the photovoltage variation covers a wavelength range from 0.4 to 1.4 μm. The response curve (in arbitrary units) for a sprayed thin film $ZnO/CuInSe_2$ cell showing a smaller wavelength range reported by Tomar and Garcia [3.3] is also plotted for comparison.

3.5.2 Isotype $ZnO/CuInSe_2$ (n-n) Heterojunctions

(1) I-V characteristics

Two isotype ZnO(n)/$CuInSe_2$(n) heterojunctions have been fabricated and studied in the present work. Figure 3.12 shows the room temperature dark and light current-voltage characteristics for sample $CuInSe_2$/ZnO-11 in a voltage range from -3 to 3 volts. Under the dark condition, the device current was small in both forward ($CuInSe_2$ positive) and reverse (ZnO positive) directions. Under the illuminated condition (tungsten lamp, about 80 mW/cm^2), the magnitude of current increased both in the reverse voltage range and for the most part of the forward region. The illuminated current-voltage characteristics shown in figure 3.12 are thus different from that predicted using a superposition principle for an ideal p-n junction. Such characteristics could be explained by considering the energy band diagram similar to

the one proposed for an n-n Si/Ge heterojunction as shown in figure 3.3 [3.12]. The energy band diagram for the isotype ZnO/$CuInSe_2$ heterostructures could be constructed so that the energy bands near the interface are bent upwards due to the presence of net electric charge in the interface states. Alternatively, the band diagram could also be constructed so that the energy bands near the interface are bent downwards due to the presence of positive charge in the interface states.

(2) Photoresponse

In order to get an idea about the band structure (bands bent upwards or downwards in the interface region), spectral response measurements were carried out on the two n-n devices. In such measurements, open circuit voltage across the junction was measured using a voltmeter with a high input impedance and the incident monochromatic light intensity determined by a calibrated Si and InSb detector. The normalized open circuit voltage (to incident photon flux density) is plotted against the optical wavelength in figure 3.13 for the sample. The open circuit voltage is negative ($CuInSe_2$ negative) in the ranges from 0.4 to 0.55 and from 1.35 to 1.7 μm. In the wavelength range from 0.55 to 1.35 μm, the open circuit voltage is positive.

The photoresponse in the wavelength range from 0.55 to 1.35 μm is very similar to that for a $CuInSe_2$ homojunction (to be described in chapter 4), suggesting that the photovoltaic effect in this region is due mainly to the optical absorption in $CuInSe_2$. The spectral response in the two outer regions has an opposite voltage polarity, and is believed to be due to the excitation of deep levels located at about 0.8 eV [3.13] below the conduction band edge of crystalline ZnO and the excitation of electrons from valence band to conduction band in ZnO side.

(3) Energy Band Structure

The energy-dependent polarity of the photoresponse suggests that the devices have an energy band structure in which band edges bent downwards near the interface, as shown in figure 3.14. From the band diagram shown in figure 3.14, photo-excited carriers generated near the space charge region in $CuInSe_2$ will flow in a direction opposite to that for carriers generated in ZnO. Therefore, the polarity of open circuit voltage (or photocurrent) is expected to be affected by the energy of incident photons. When photons with energy larger than $E_g(CuInSe_2)$, the excited electrons at $CuInSe_2$ side will drift from left to right and make $CuInSe_2$ to be more positive than ZnO. For photons with energy between 0.8 eV and 1.01 eV or larger than 3.3 eV, the excited electrons

will be swept out of the space charge region in ZnO. This will make $CuInSe_2$ side to be more negative.

Under the dark condition, due to the presence of the potential notch (figure 3.14), device current will be limited for both bias directions (see figure 3.12). When a forward voltage ($CuInSe_2$ positive) is applied across to the junction, the space charge region in $CuInSe_2$ is narrowed and that in ZnO is widened. The photo-current will be due mainly to carrier excitation in ZnO, giving rise to a bias-dependent photocurrent flowing from $CuInSe_2$ side to ZnO side. When a reverse bias voltage (ZnO positive) is applied, the space charge region in ZnO side is narrowed and that in the $CuInSe_2$ side is widened and the major part of photocurrent is from excitation of carriers in the $CuInSe_2$ side. The combined photocurrent is now flowing from ZnO to $CuInSe_2$ and is opposite to that under forward bias condition. Because of the large energy gap and the small optical absorption coefficient of crystalline ZnO, the photocurrent under reverse bias conditions is several times of that under forward bias (figure 3.12).

3.6 CONCLUSIONS

Isotype and anisotype heterodiodes of the form ZnO(n)/$CuInSe_2$(p or n) have been fabricated by sputtering a layer of ZnO on polished monocrystalline Bridgman-grown $CuInSe_2$ samples. The current-voltage and capacitance-voltage characteristics of the devices have been investigated. Energy band diagrams with a negligible conduction band discontinuity have been established for the heterosystems based on the material parameters. Dipole effect with a negative sign were found to be neccesary to account for the large apperant diffusion potential found from the differential capacitance-voltage measurements on the anisotype heterojunctions. However, the density of interface states and dipole can not be determined from the present results. For the anisotype ZnO(n)/$CuInSe_2$(p) junctions, the dark current flowing in the devices in the low voltage region appeared to be dominated by a tunneling and recombination process of carriers through these interface states. For these heterostructures, if a larger electron affinity value for crystalline $CuInSe_2$ is adopted [3.14] for the energy band diagram, then a conduction band discontinuity will be present.

The variation of open circuit voltage with wavelength for the junctions fabricated using p-type $CuInSe_2$ was similar to that for a $CuInSe_2$ homojunction. For the diodes

fabricated using n-type $CuInSe_2$, however, the polarity of the open circuit voltage was dependent on the optical wavelength. In the short wavelength region, the open circuit voltage was produced mainly by the band gap exitation of ZnO. In the long wavelength region, the voltage was due to the possible exitation of deep levels located at about 0.8 eV below the conduction band edge of ZnO. In the medium wavelength region, the voltage was dominated by the band gap exitation of $CuInSe_2$.

TABLE 3.1 PARAMETERS USED TO CONSTRUCT THE ZnO/$CuInSe_2$ BAND DIAGRAM.

Parameters	ZnO	$CuInSe_2$
Energy Gap, E_g (eV)	3.3	1.01
Electron Affinity (eV)	4.35 [3.15]	4.3 [3.16]
Net Donor Conc. (cm^{-3})	10^{20}	------
Net Acceptor Conc. (cm^{-3})	------	10^{15}
m_e/m_o	0.24 [3.18]	0.09[3.19]
m_e/m_h	0.21 [3.18]	0.12[3.19]
E_F-E_V (eV, 300K)	------	0.21
Lattice Constant, a (Å)	3.24 [2.2]	5.78[3.20]
Relative Dielectric Constant, ϵ_r	8.5 [2.1]	9.3

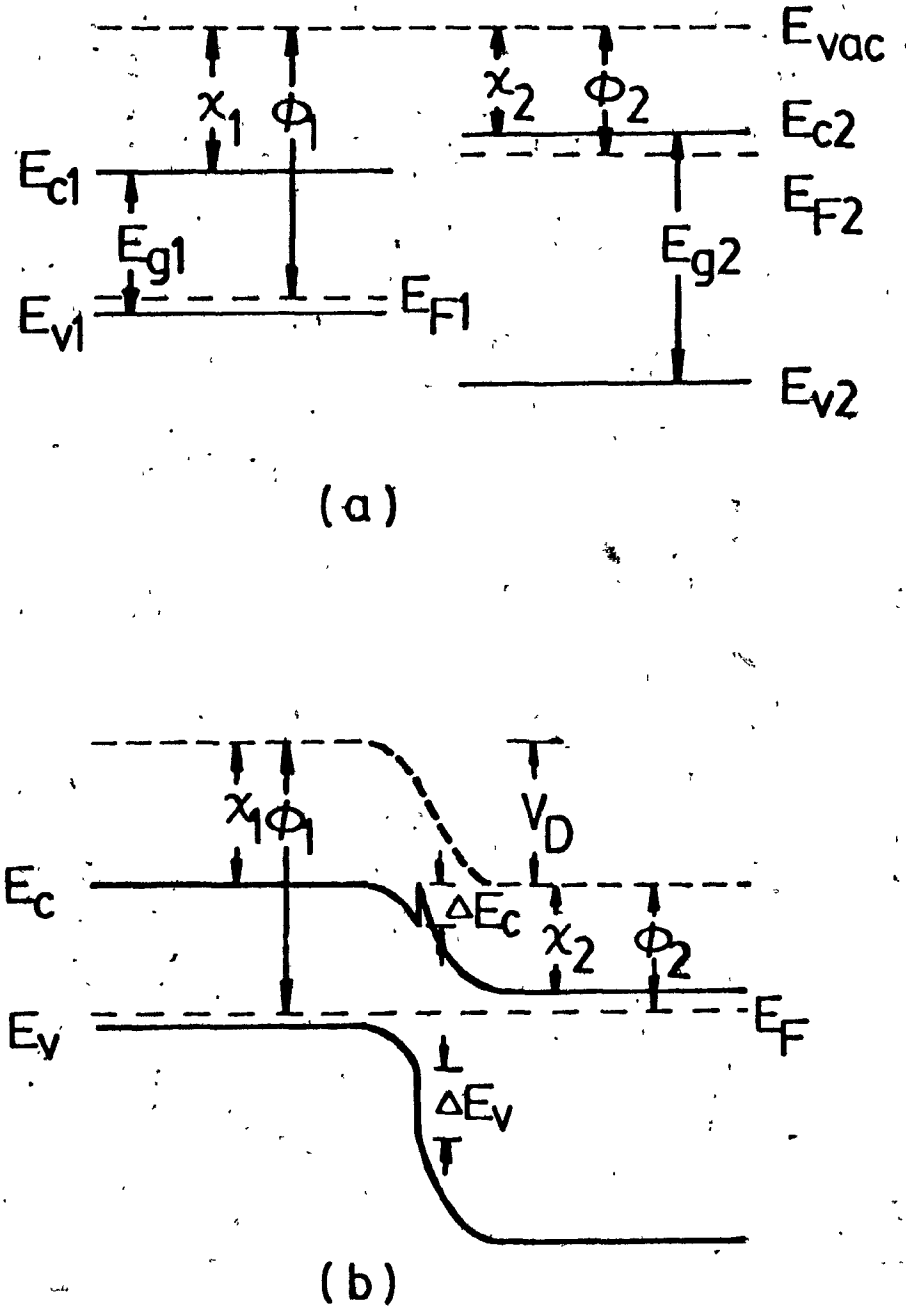

Fig. 3.1 Equilibrium energy band diagram of an anisotype heterojunction: (a) before and (b) after the formation.

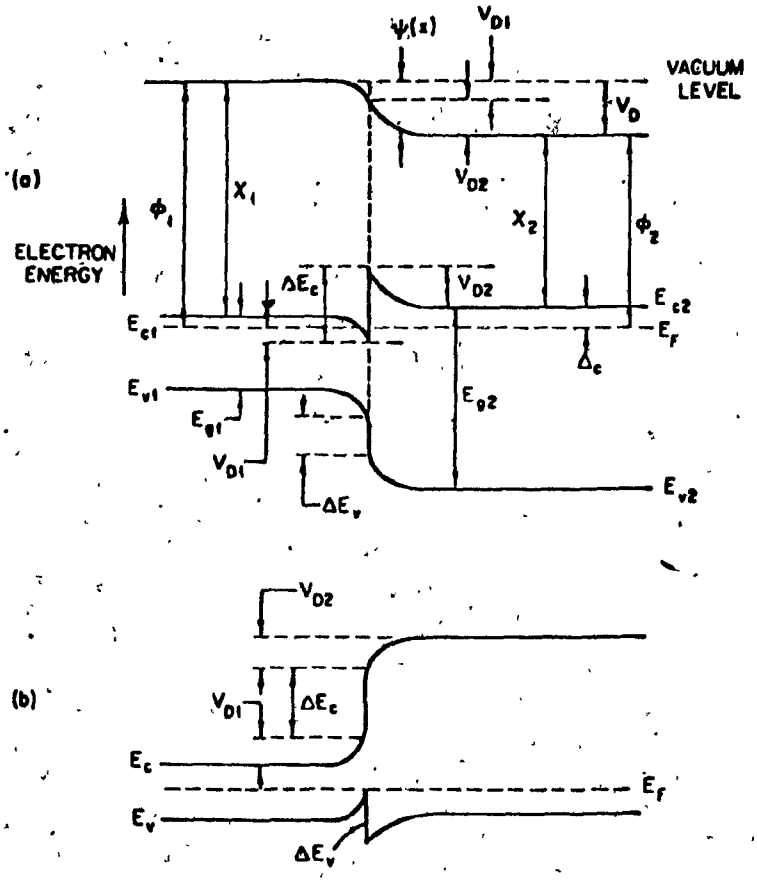

Fig. 3.2 Energy band diagrams of (a) an n-n and (b) a p-p heterojunction without interface states [3.1].

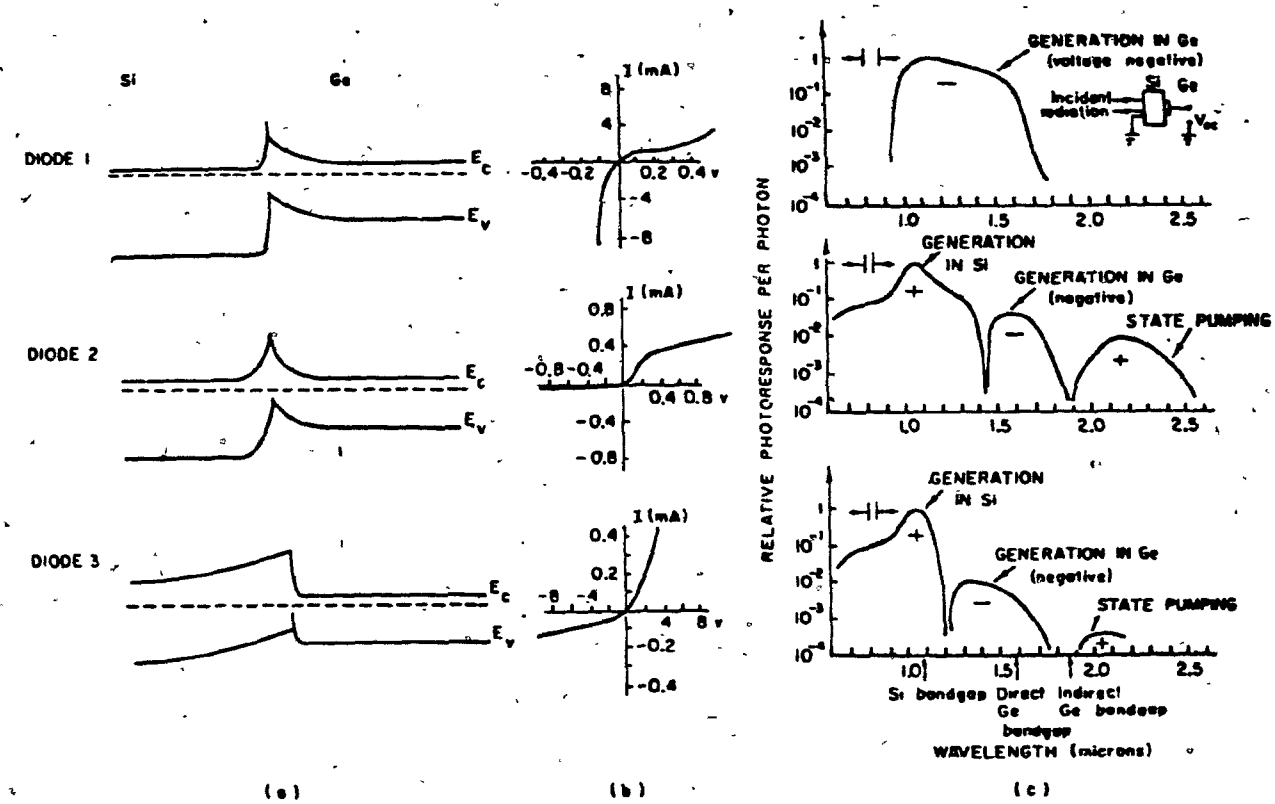

Fig. 3.3 (a) Energy band diagrams of three isotype heterojunctions with interface states: diode 2 with depletion regions on both sides of the junction while diodes 1 and 3 with most of the depleted region located in lightly doped side, (b) corresponding I-V characteristics and (c) variation of relative photoresponse with wavelength. It is noted that the polarity of the response for diodes 2 and 3 changes when the wavelength is changed [3.10].

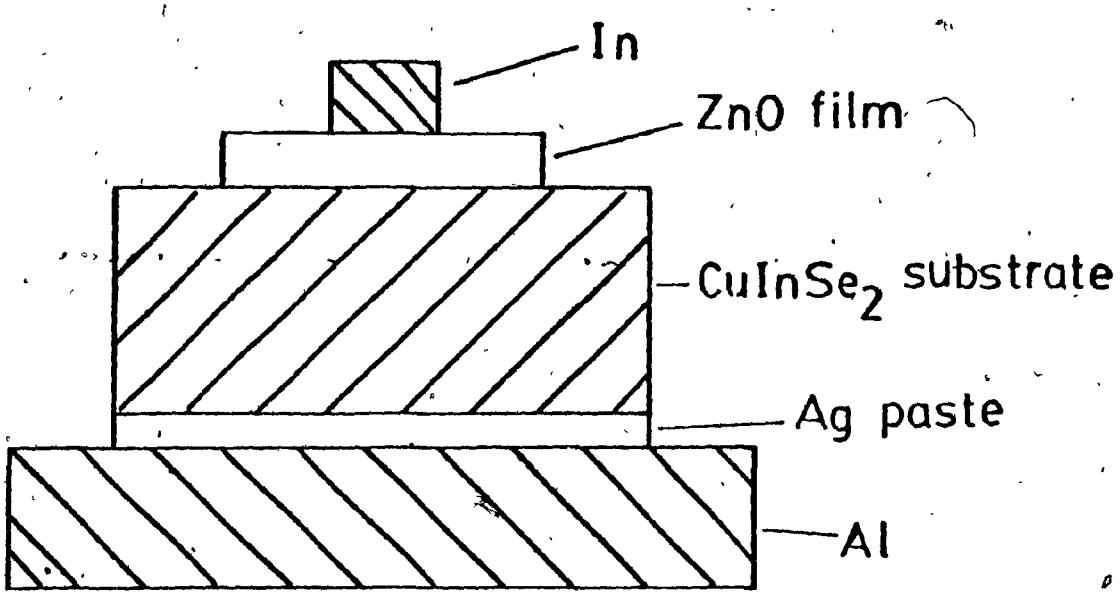

Fig. 3.4 A schematic cross sectional view of the fabricated ZnO/$CuInSe_2$ heterojunction.

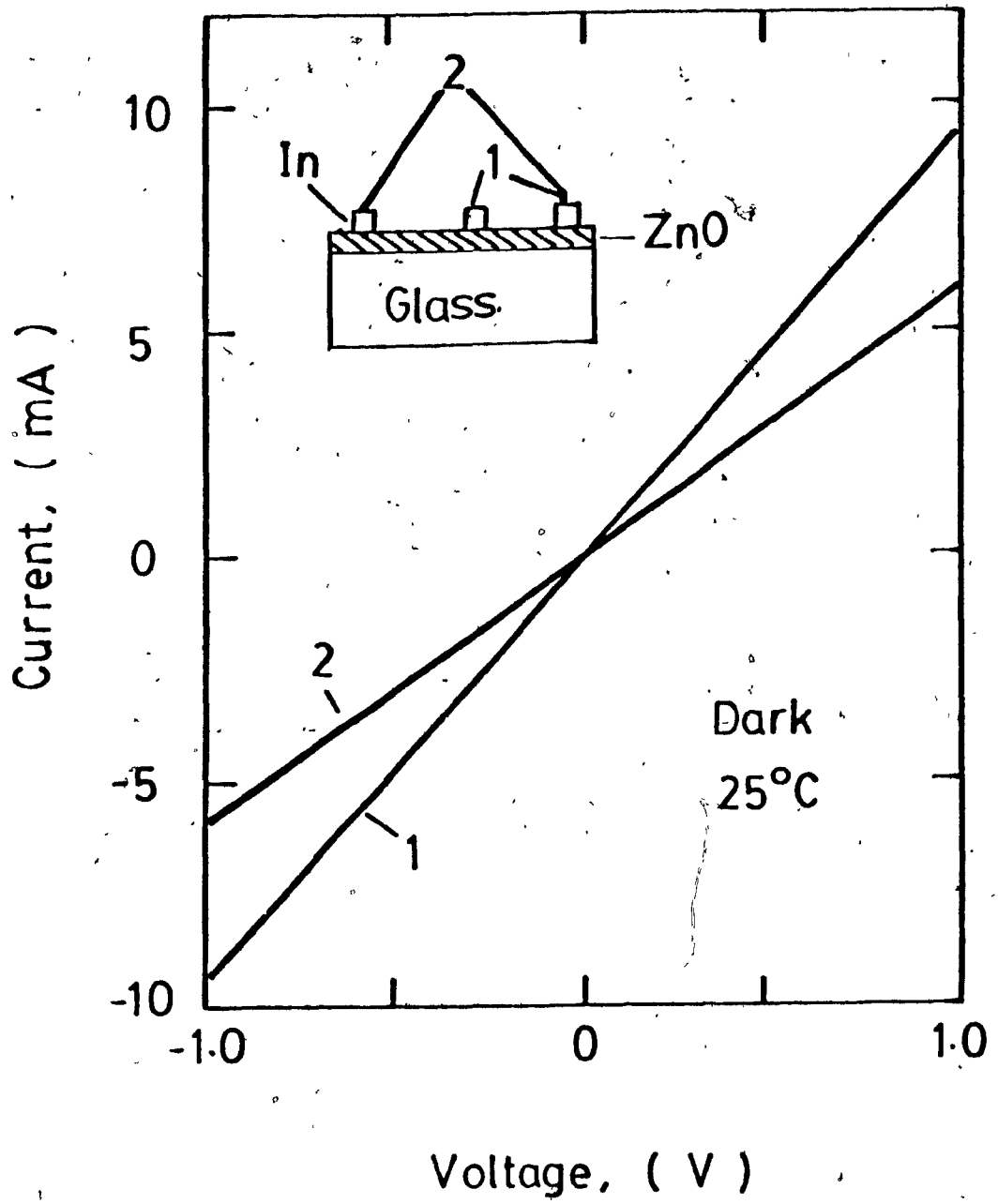

Fig. 3.5 Current-voltage characteristics between two indium areas deposited on a ZnO film showing the low resistance properties of the In/ZnO contact.

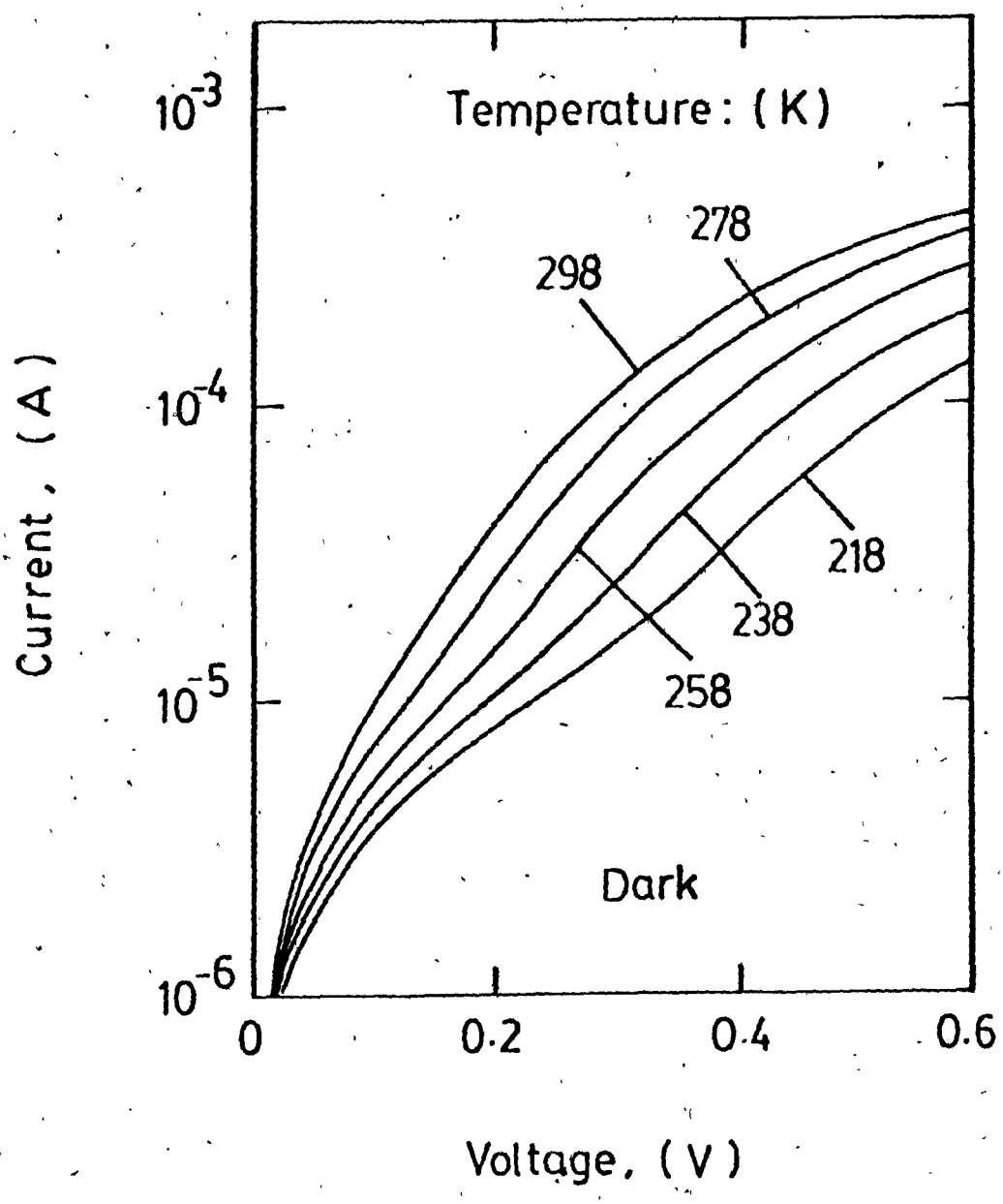

Fig. 3.6 Dark forward current-voltage characteristics of a ZnO(n)/$CuInSe_2$(p) junction measured at different temperatures.

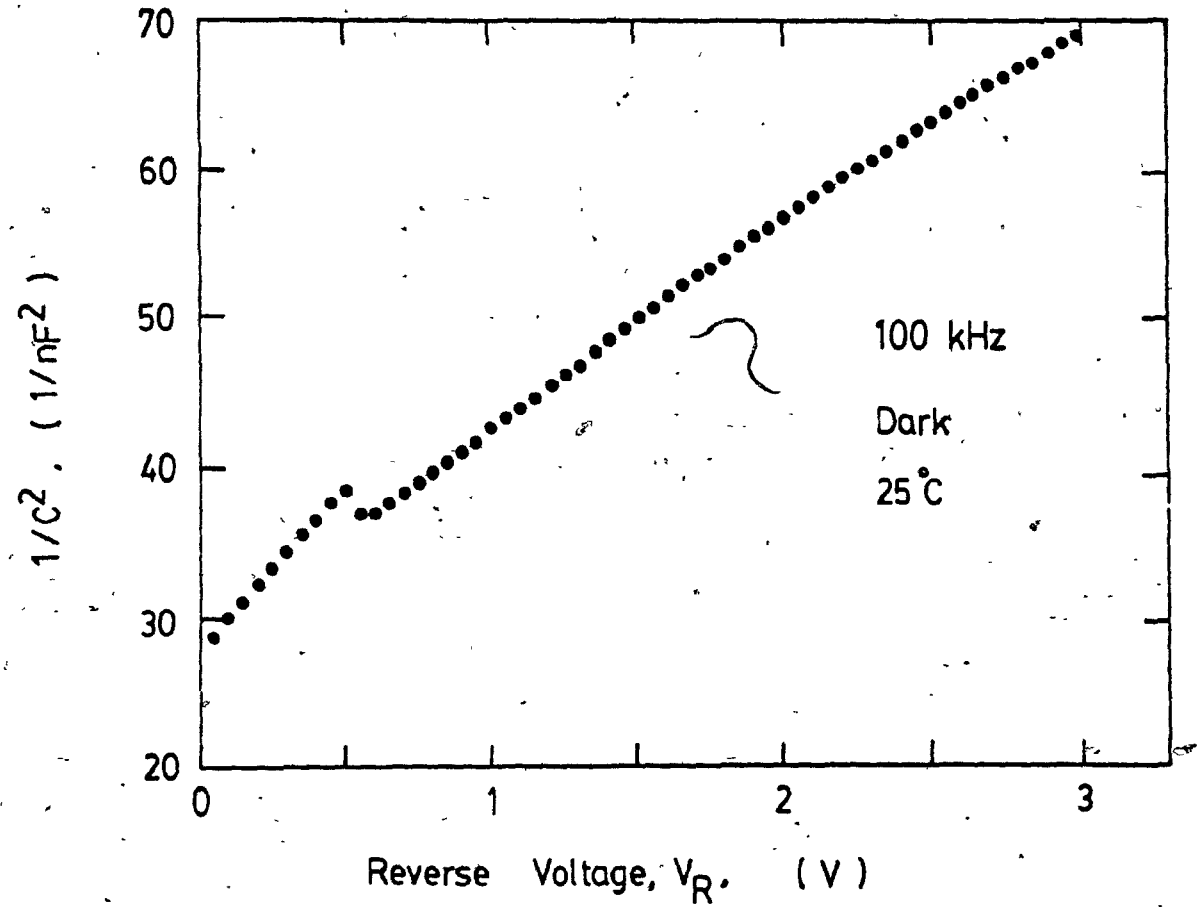

Fig. 3.7 A plot of $1/C^2$ versus reverse voltage for the anisotype ZnO(n)/$CuInSe_2$(p) heterojunction at room temperature, showing the relatively large apparent barrier height.

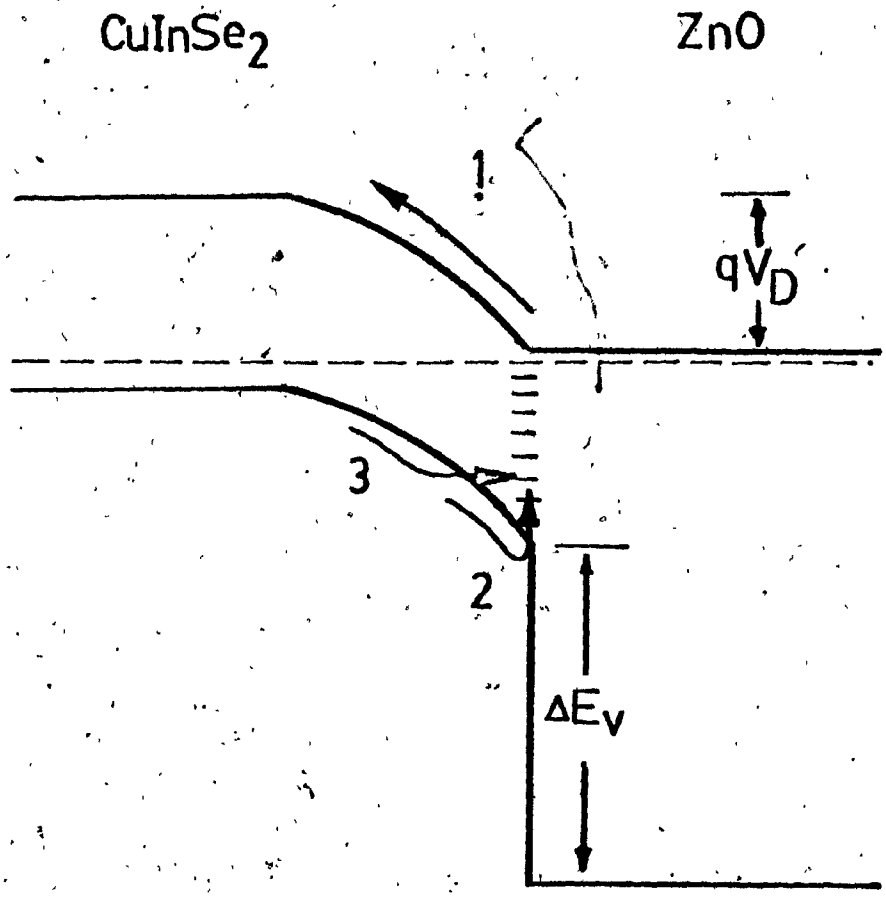

Fig. 3.8 Energy band diagram of the anisotype $ZnO(n)/CuInSe_2(p)$ heterojunctions.

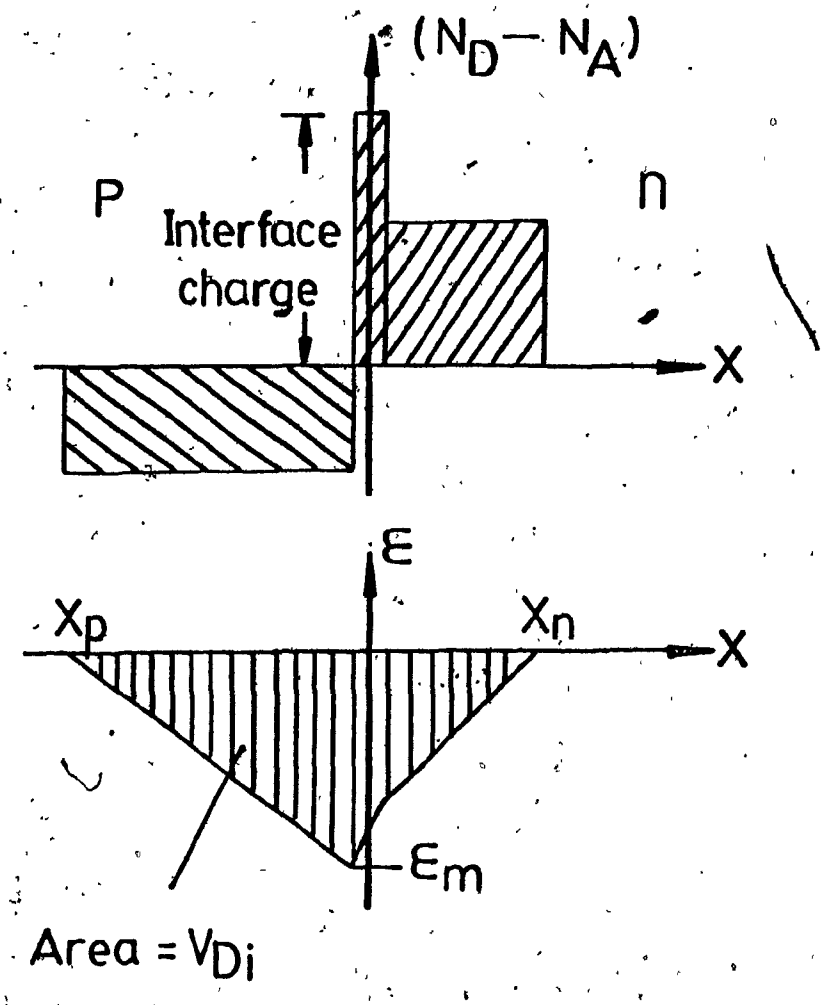

Fig. 3.9 Net space charge density distribution and the corresponding electric field distribution of a heterojunction showing the effect of charged interface states.

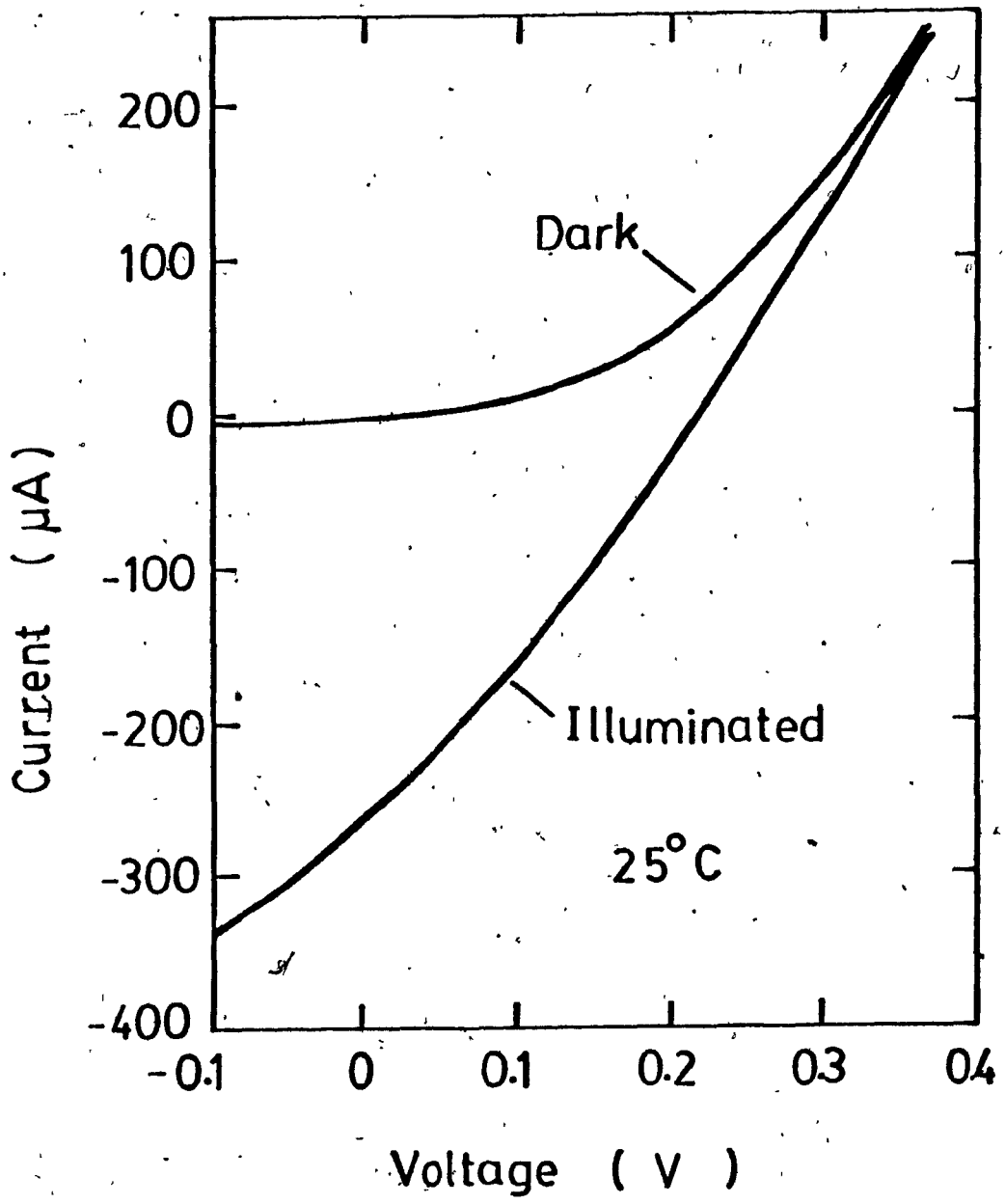

Fig. 3.10 Dark and illuminated current-voltage characteristics of the ZnO(n)/$CuInSe_2$(p) heterojunction.

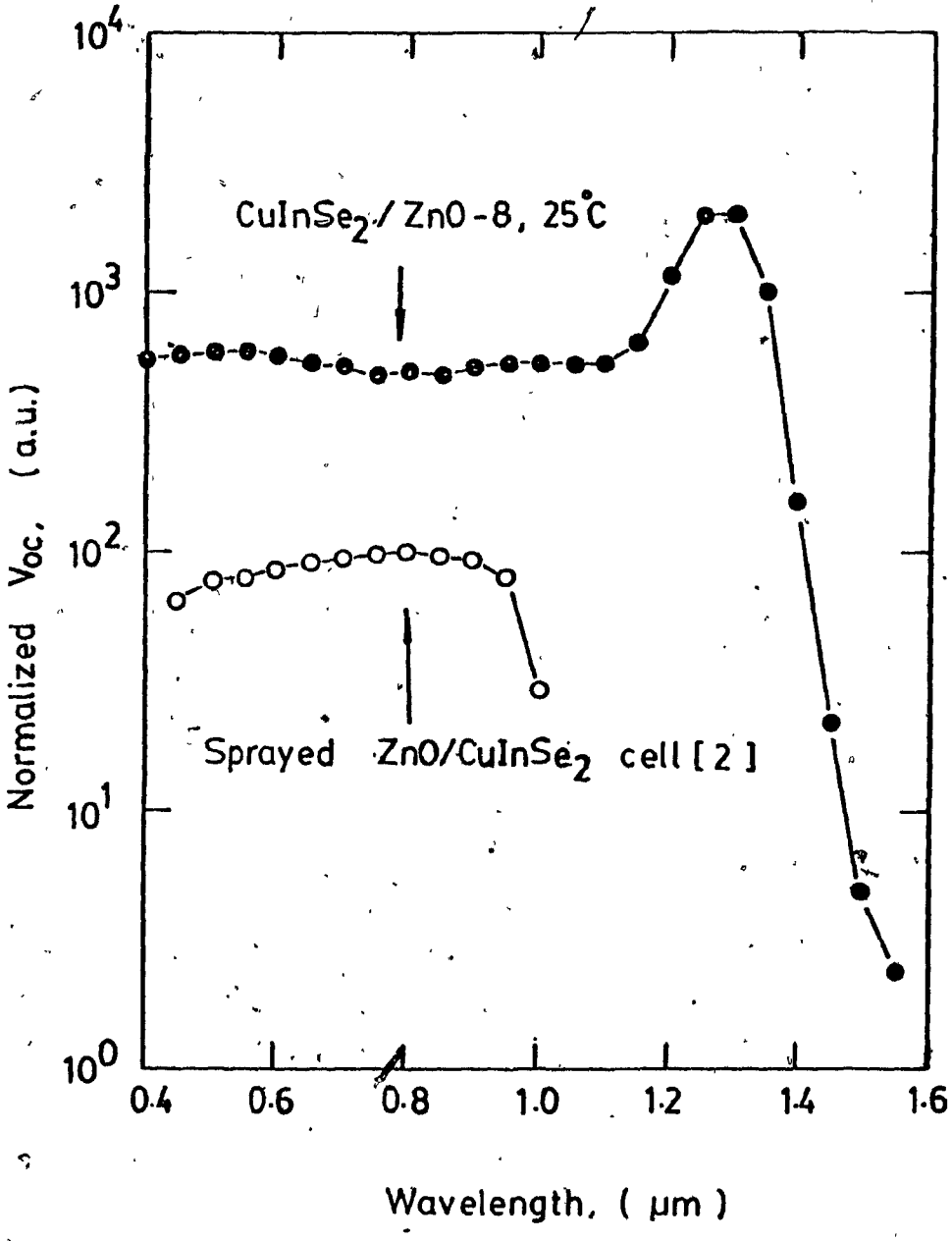

Fig. 3.11 Normalized open circuit voltage plotted against wavelength for the anisotype ZnO(n)/$CuInSe_2$ (p) heterojunction. The response curve of a sprayed cell is also given for comparison.

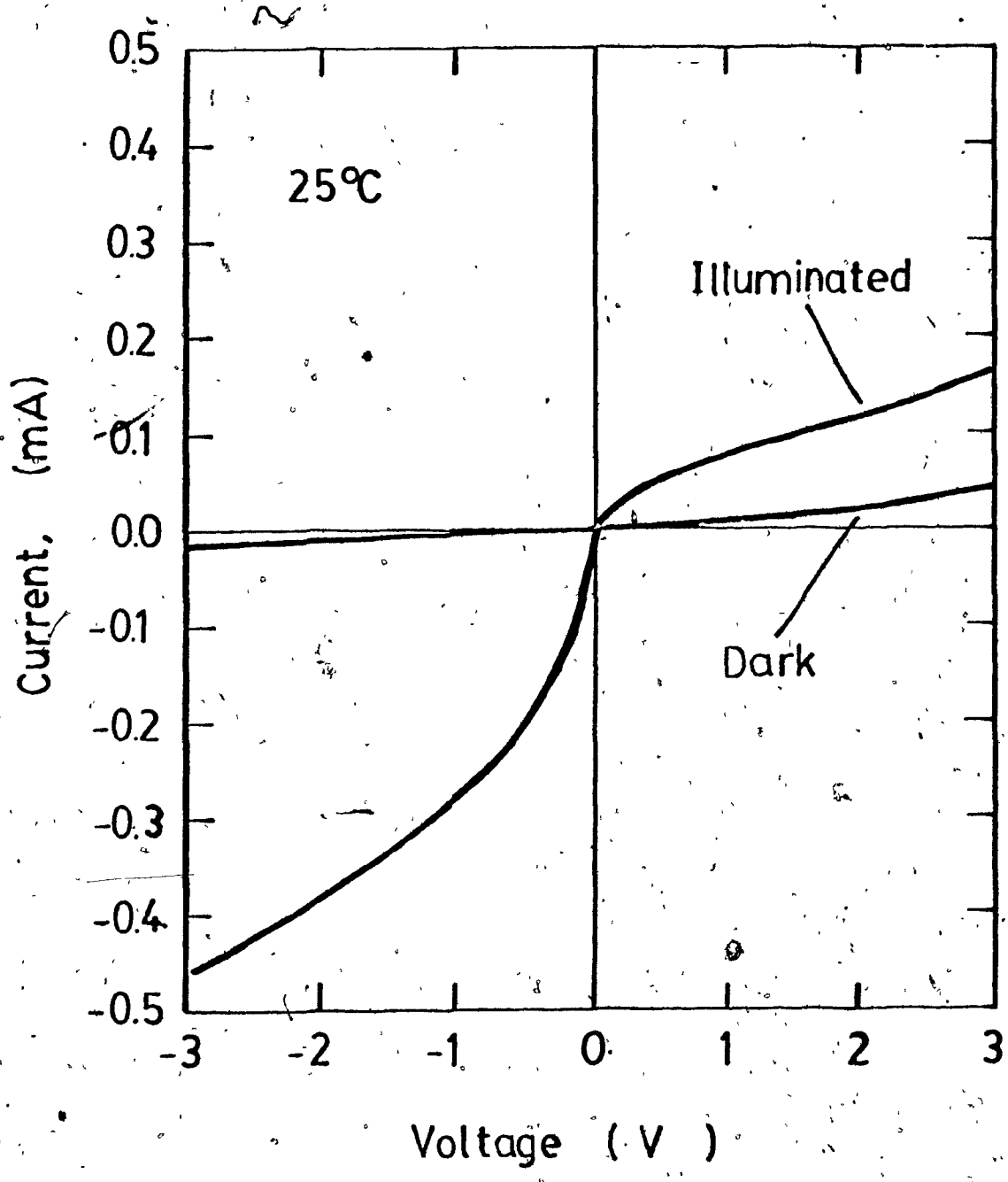

Fig. 3.12 Dark and illuminated current-voltage characteristics of an isotype ZnO/$CuInSe_2$ heterojunction.

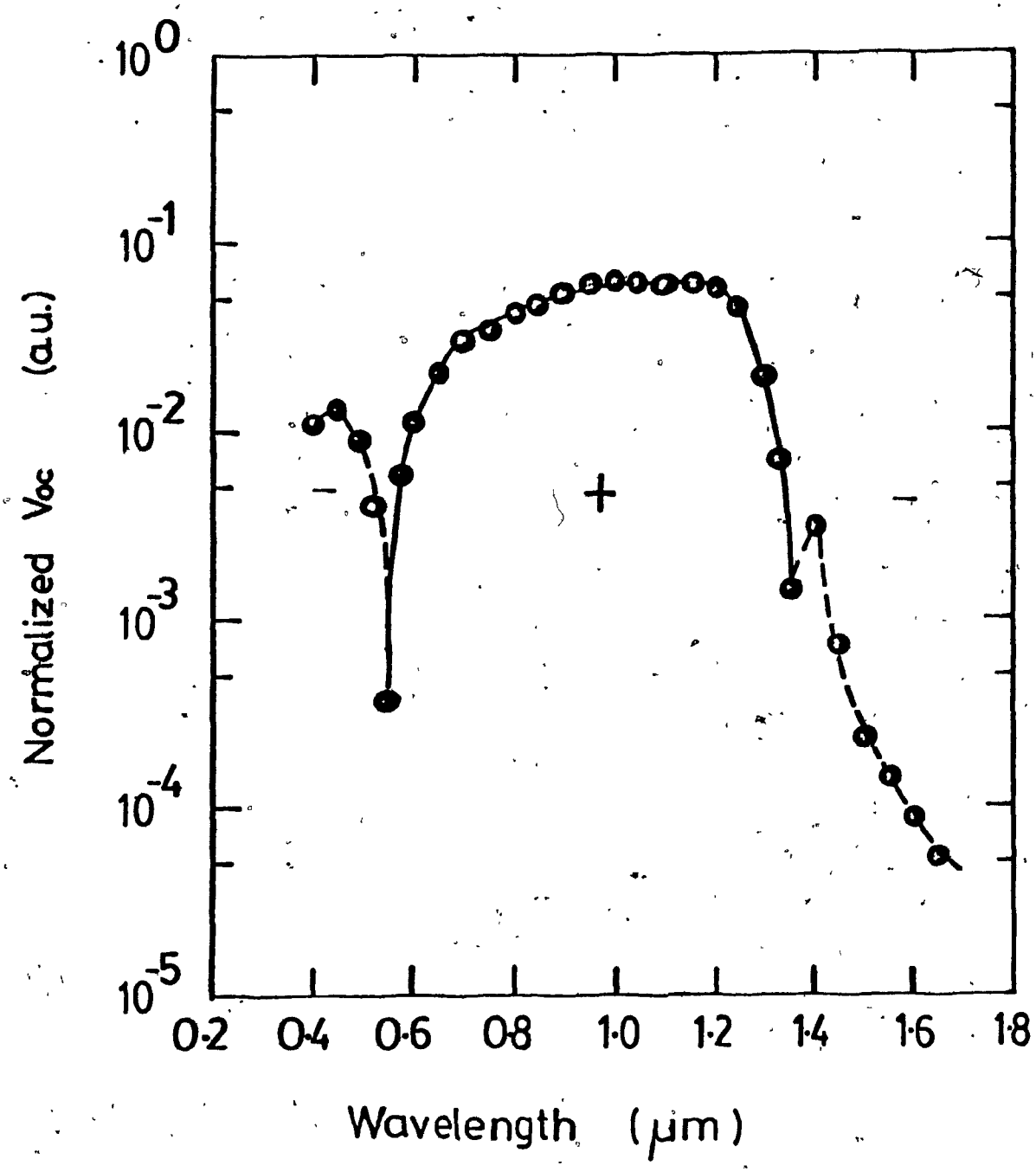

Fig. 3.13 Normalized open circuit voltage of the isotype ZnO(n)/$CuInSe_2$(n) junction plotted against the optical wavelength, showing the reversal of voltage polarity.

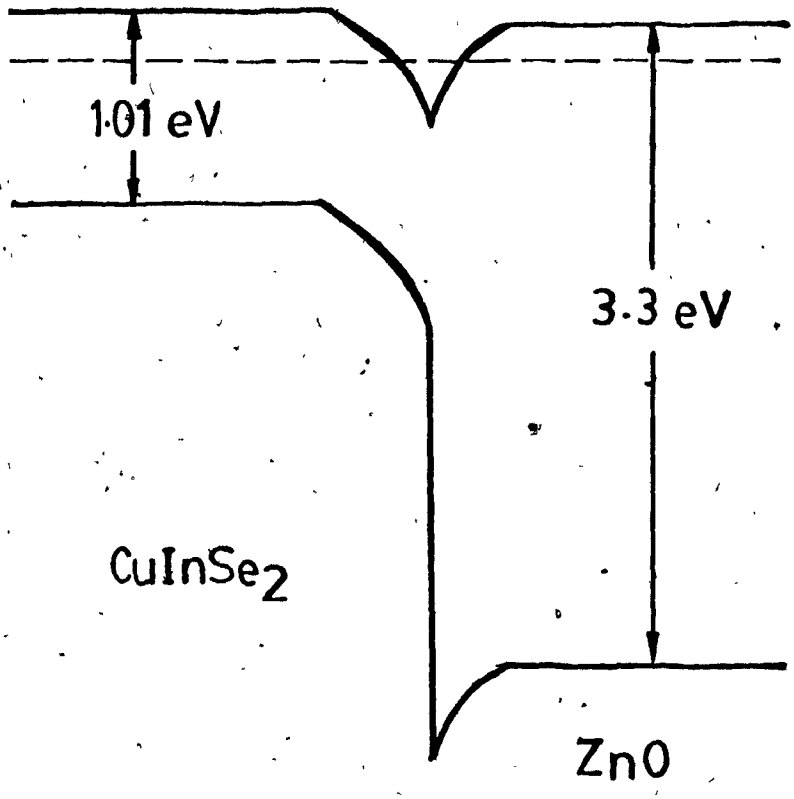

Fig. 3.14 Energy band diagram constructed for the isotype ZnO(n)/$CuInSe_2$ (n) heterojunctions.

Chapter 4 ELECTRICAL STUDIES OF MONOCRYSTALLINE $CuInSe_2$ JUNCTIONS

4.1 INTRODUCTION

In chapter 3, I-V characteristics, photoresponse and energy band structures of the $ZnO/CuInSe_2$ heterojunctions have been described. However, due to the presence of interface states (the density of which could be comparable to the dangling bond density at the interface) only limited information about characteristics of $CuInSe_2$ monocrystalline sample of the heterostructure has been obtained. In order to further characterize the crystalline $CuInSe_2$ material, several n^+p homojunctions fabricated by diffusing indium or bismuth into the Bridgman-grown p-type monocrystalline $CuInSe_2$ samples [3.11] have been studied. Using the n^+p homojunctions for measurements (C-V for example), effect of interface states can be neglected. Therefore, characteristics of $CuInSe_2$ near the depletion region edge can be conveniently obtained.

It is also important to investigate energy states in crystalline $CuInSe_2$ especially for device applications. These have been reported recently by luminescent and electrical

studies [4.1-4.3, 3.20] revealing several shallow acceptor or donor states with ionization energy values of few tens of a meV. From the I-V characteristics studies of $CuInSe_2$ homojunctions, it is expected that recombination centers of a large density exist in monocrystalline $CuInSe_2$. Therefore, to further characterize crystalline $CuInSe_2$, a preliminary program was initiated in the present work to study deep levels. The preliminary investigation of deep levels in p-type region of the device was made by a differential capacitance technique, a transient technigue [4.4] and a thermally stimulated capacitance method [4.5]. The results obtained from these measurements indicate that deep traps are present in the depletion region although the energy position of the trap levels can not been determined precisely at the present time.

4.2 SAMPLE PREPARATION AND MEASUREMENT TECHNIQUES

4.2.1 Sample Preparation

P-type $CuInSe_2$ crystalline samples were selected from ingots grown by the horizontal Bridgman method [4.6]. The samples were then polished using 0.05 μm alumina powder and etched in a mixture of HNO_3 and HCl with a ratio of 1:3 for about 2 minutes to remove the oxide layer. A circular area of Bi or In with a diameter of about 3 mm and a thickness of

about 1 μm was evaporated onto the polished surface in a vacuum chamber with a base pressure of 10^{-6} Torr. The samples were then heated in an inert atmosphere at about 200 °C for about 20 minutes (samples In-5-1 and In-5-2) and a junction depth of about 10 μm was achieved in the fabricated devices. Sample In-3 was heated at 200 °C for 10 minutes and Bi-3 was heated at 250°C for 10 minutes. After that, the back side of the sample was polished using a fine sand paper. Contact to the back side (p-type region) was obtained by applying a layer of silver paste between the sample and an aluminium holder and heat treating the sample at a temperature of 100°C for 10 minutes. The front contact was made directly by soldering a metal wire using Wood's alloy.

4.2.2 I-V Measurement Technique

Dark current-voltage characteristics of the devices were obtained by using a Hewlett Packard model 4145A Semiconductor Parameter Analyzer. The time delay for each measurement (hold time) was chosen to be 0.2 second. The fabricated $CuInSe_2$ devices were mounted to an Oxford Instruments model CF 100 cryostat which was connected directly to the analyzer. During the measurements, liguid nitrogen was used to cool the samples to low temperatures. Sample temperature was controlled by a temperature controller

and an accuracy better than ± 0.5°C in the range between 200 and 300 K was achieved.

4.2.3 C-V Measurement Techniques

Differential capacitance measurements of the homojunctions were performed using an HP 4274A LRC meter (freguency range from 10^2 to 10^5 Hz) controlled by an IBM PC as described in chapter 3. A parallel circuit mode was chosen during the measurements and the amplitude of the ac signal was about 0.01 V throughout the present experiments. The experiments were carried out under a dark condition with different reverse bias voltages, frequencies, time intervals (only for transient capacitance measurements) and temperatures (only for thermally stimulated capacitance technique). For differential capacitance and thermally stimulated capacitance experiments, at least four sets of measurement were taken under the same condition (bias voltage, frequency, temperature) and the average results were recorded using a printer or plotter unit (HP model 7475 A). In order to reduce the stray capacitance introduced by connecting wire, a cryostat with very short lead wire was used.

4.3 EXPERIMENTAL RESULTS

4.3.1 I-V Characteristics and Transport Mechanisms

Shockley [4.7] has pointed out that the current flowing in an ideal p-n junction is given by the following equation,

$$I \propto T^3 \exp(-E_g/KT)[\exp(eV/nKT)-1] \qquad (4.1)$$

where the curve factor (n=1) is independent of temperature. For non-ideal junctions, the current component resulting from recombination processes is important. The recombination current in the depletion region as a function of bias voltage has been studied by Sah et al [4.8] and can be described by the following equation,

$$I \propto T^{3/2} \exp(-E_g/nKT)[\exp(eV/nKT)-1] \qquad (4.2)$$

where n=2 and this value may change slightly in actual devices, which will be shown later in this chapter.

The dark forward I-V characteristics of two In-diffused junctions at several temperatures are shown in figures 4.1 and 4.2 and that for a Bi-diffused junction are plotted in figure 4.3. It is seen that in the present voltage range,

three regions exist, especially for the low-temperature case. In the low-bias region the I-V curve factor, n, is greater than two while in the high-bias region the series resistance effect becomes dominant. In the medium voltage region, the curve factor n is about two for three samples (less than 2 for In-5-1, Bi-3 and greater than 2 for In-3). The transition point for low-voltage region and medium-voltage region increases with the decrease of the temperature. This fact suggests that there are two current components in this voltage range, one is less sensitive to temperature while the other decreases with decreasing temperature. The first component might be due to the surface leakage. The second one, dominant in the medium voltage region, has an exponential dependence on the bias voltage and the slope of it almost unchanged when temperature changes from 295 to 200 K. The room temperature saturation current, obtained by extrapolating the linear (medium) region of the forward room temperature I-V curve, is about 2×10^{-8} A for both In- and Bi-diffused devices. The measured saturation currents within the 295-200 K range cover more than three orders of magnitude. These characteristics in the medium voltage range (n=2, saturation current changes over 3 orders of magnitude in the range of 100 K) suggests that the junction current in the medium region is mainly controlled by the recombination mechanism in the depletion region, where the current is given

by equation (4.2) and the curve factor is about 2 in practical devices.

It is noted that the saturation current I_o is proportional to $T^{3/2}\exp[-E_g/nKT]$. Therefore, a plot of $\log[I_o/(T^{3/2})]$ against $1/T$ will yield a straight line. Figure 4.4 shows the current results for the three samples. Results caculated from the recombination current equation, assuming E_g=1 and n=2, is given by the solid line for comparison. It is seen that all the three samples show a linear variation with a slope close to the caculated one. The small slope value, E_g/n, for sample In-3 in figure 4.4 is due to the large curve factor n. This results let one conclude that the dominant transport mechanism in the medium voltage range is carrier recombination in the space charge region.

4.3.2 C-V Characteristics and Deep Levels

(1) Frequency-Dependent C-V Characteristics

Using the depletion approximation, the differential capacitance of a p^+n junction under the reverse bias condition without deep traps is given by,

$$C = dQ/dV = \varepsilon/W = [q\varepsilon N_D/2(V_D-V)]^{1/2} \qquad (4.3)$$

Here ε is the dielectric constant of the semiconductor, W is the depletion layer width, N_D is ionized impurity concentration in the semiconductor, V_D is the built-in potential and V is the bias voltage. It is noted from the equation that the differential capacitance is independent of the measurement frequency. However, if traps are present in the depletion region, the finite time constant for charging and discharging of the traps will result in frequency-dependent capacitance characteristics. This phenomenon has been investigated on gold-doped silicon p^+n-junctions by Sah and Reddi in 1964 [4.9]. Their model is based on the trapping time constant of the deep-gold acceptor level in the depletion region and is in agreement with the experimental results. This effect has also been studied theoretically by E. Schibli and A.G. Milnes using a numerical technique [4.10].

For a one-sided junction (n^+p for example) with simple traps, the capacitance characteristics are relatively simple and can be devided into three regions. At low frequencies, deep traps can follow the charging and discharging processes. Therefore, the capacitance is determined both by shallow impurity (acceptor in this case) and deep traps and the differential capacitance value is large. At high frequencies, most of the traps can not respond to the charging/discharging voltage, therefore the capacitance is determined only by the

effective dopant concentration in lightly doped side of the junction (acceptor) and essentially has a constant value. In the medium frequency range, the density of responding traps decreases as the frequency is increased, causing a decrease in the differential capacitance until a constant value is reached. Therefore, non-constant capacitance-frequency characteristics will serve as an initial indication for the presence of deep traps in the lightly doped side of the one-sided homojunction devices.

In the present experiments, capacitance-voltage results of three n^+p $CuInSe_2$ homojunctions have been obtained at a temperature of 298 K over a frequency range from 10^2 to 10^5 Hz. Figure 4.5 shows the measured results for sample Bi-3. It is clear that the capacitance decreases with the increase of frequency. The measured differential capacitance for three samples at a reverse voltage of -0.3 volt is also plotted versus frequency in figure 4.6. It is seen that the differential capacitance decreases by a factor of 2 to 3 as the frequency is increased from 10^2 to 10^5 Hz. Constant capacitance region does not appear to exist in the frequency range studied, suggesting that the charging/discharging time constant of the traps covers a relatively large range. The results also suggest that the total effective traps density is comparable to the net acceptor concentration, which is about 10^{14} cm^{-3} in the depletion edge region of the p-type $CuInSe_2$.

variation in the density of traps occupied by holes, p_T, which can be described by,

$$dp_T/dt = -e_p\ p_T \qquad (4.5)$$

here t is time and e_p is emission rate of the trapped holes. The time-dependent trapped hole density then results in a transient capacitance effect. Curve 1 in figure 4.8 shows the results of transient capacitance taken for sample In-5-1 at room temperature. Similar results have been obtained for sample In-5-2 and Bi-3. The $\Delta C(t)$ values, which are negative, confirm that hole traps are responsible for the major part of the transient process. From this curve, the hole emission rate and the density of participating trapped holes can be estimated. Assuming $p_T << N_A$, a simple relation as shown below can be obtained from the differential capacitance equation,

$$\Delta C(t)^2 / C_o^2 = p_T/N_A \qquad (4.6)$$

here C_o and $\Delta C(t)$ have the same definition as above. Since $C_o^2 \propto N_A$, so

$$\Delta C(t) \propto -(p_T)^{1/2} \qquad (4.7)$$

The minus sign is chosen because the hole traps dominate the

transient effect and a negative $\Delta C(t)$ is expected. From the curve 1 in figure 4.8, the hole emission rate is estimated to be about 0.35 1/second and the emission time constant is 2.8 seconds. Assuming the traps are all occupied by holes and neglecting the time delay (0.2 sec.) before taking the measurement, density of trapped holes having the above emission time constant can be estimated from the equation $\Delta C(t)^2 / C_o^2 = p_T/N_A$. The value obtained is in the order of 10^{10} cm^{-3}.

In order to see the effect of minority carrier (electron) traps, a positive filling pulse (0.3 volt) with a duration of 10 seconds was applied. After that, a zero biasing condition was maintained for about 0.2 second to sweep the free electrons, which will affect the transient capacitence results, out of the regions A and B. The induced capacitance sequence is shown in figure 4.9. Under the application of the forward bias pulse, both electron and hole traps are filled in the neutral region (region A, figure 4.9). For the n^+p $CuInSe_2$ homojunctions under consideration with $\mu_n/\mu_p > 10$ [3.11], the number of injected holes under the forward biasing condition is much smaller than that for electrons. Hole traps in region B are essentially empty. The capacitance transient, under such conditions, is therefore governed both by the electron and hole emission events. Results obtained from sample In-5-1 are shown in figure 4.8,

curve 2. In the initial stage of the capacitance transient process with the 0.3 volt filling pulse, magnitude of $\Delta C(t)$ first increases with the increase of time mainly due to the emission of the trapped electrons and then decreases with a decay time constant similar to that for curve 1. (It should be pointed out that the data points at t=0 in figure 4.8 were taken at about 0.1 second after the reverse bias voltage had been applied.) The results indicate that in the initial decay period (the first two seconds), the emission process is dominated by electrons. However, the hole emission is important in the most part of the decay process. Therefore, the results given in curve 2 suggest that either the density of the trapped electrons is small or the electron emission time constant is short as compared to that for holes.

(3) Thermally Stimulated Capacitance (TSCAP)

Thermally stimulated capacitance [4.5] was also investigated for the sample In-5-1 to determine the energy position of the traps. Two sets of measurement were taken on this sample and the results were then compared. In the first measurements, a reverse bias voltage of -0.7 volt was first applied to the junction (to empty the traps in the depletion region) at room temperature. The device was cooled to about 120 K in a period of about 5 minutes and then warmed up at a rate of about 15 ^{o}C/min. During the warming process,

differential capacitance data were taken at 100 kHz at a $5^{o}C$ interval. The results are shown in figure 4.10, curve 1. To observe the deep traps, a small forward bias was applied to the device during the cooling period and the same reverse voltage was used in the warming process. At low temperature range, the differential capacitance of the device will be smaller than that measured when the traps are empty. During the warming process, thermally stimulated emission of trapped holes causes an increase in the capacitance.

The characteristic temperature in the TSCAP curve where the capacitance value increases drastically can be used to estimate the energy position of the traps. Curve 2 in figure 4.10 shows the TSCAP characteristics of the sample In-5-1. The curve shows a rapid increase in the capacitance at about 200 K indicating a rapid emission of the trapped holes at this temperature. However, the results given in figure 4.10 must be regarded as tentative, because it has been observed from about 20 experimental runs that the TSCAP results for the $CuInSe_2$ junction were affected by the heating/cooling cycle and the biasing history of the device.

4.4 CONCLUSIONS AND DISCUSSION

Dark I-V characteristics of three crystalline $CuInSe_2$

n^+p homojunctions (two In-diffused and one Bi-diffused) have been studied over a temperature range from 100 to 300 K by using an HP model 4145 A Semiconductor Parameter Analyzer. It was found that all devices possess the following characteristics. (1) The curve factor is about 2 in the medium voltage range. (2) The room temperature saturation current is about $2x10^{-8}$ A and decreases by about 3 orders of magnitude as the temperature is decreased to 200 K. These facts indicate that the current in the medium voltage range of the $CuInSe_2$ homojunctions is dominated by a recombination mechanism in the depletion region.

Initial results of deep levels obtained in the present work have been described in this chapter. Differential capacitance at a reverse voltage of about -0.3 volt decreased by a factor of 2 to 3 as the frequency was increased from 10^2 to 10^5 Hz for all samples, suggesting that the total density of deep traps with trapping time constant less than 0.01 second is comparable to the net acceptor concentration. Transient technique was adopted to study the characteristics of traps at a frequency of 100 kHz. Effects for both hole and electron traps have been observed on samples In-5-1, In-5-2 and Bi-3. The results show that the density of hole trapping centers with an emission time constant of about 2.8 seconds is of the order of 10^{10} cm^{-3} (traps with a shorter emission time constant can not be observed using the present

technique since the time delay of instrument). Transient effects have not been observed for sample In-3 becuase a large N_A value at the depletion region edge (due to the short diffusion time of 10 minutes). The large N_A value reduces the effect of traps ($\Delta C^2/C_o^2 = p_T/N_A$). Results of thermally stimulated capacitance provided an idea about the energy position of the trapping levels but these can only be regarded as tentative at the present.

It is also interesting to point out that, Roberts and Crowell [3.12] have developed a model for a Schottky diode with several deep levels. Each deep trap state is assumed to have a short time constant (less than the reciprocal of the frquency) and will contribute a dip to the C^{-2} versus V_R plot when the level is pulled above the Fermi level (for electron traps) at a particular voltage. Following this model, trapping states in thin film CdS/Cu_xS heterojunctions have been observed recently by L. Hmurcik et al [4.11] using the capacitance measurement technique. Their results appear to be the first ones to support the Roberts and Crowell model. In the present work, C-V characteristics of two $CuInSe_2$ homojunction samples also have been investigated in the frequency range from 100 Hz to 100 kHz. A single dip of $1/C^2$ vs. V_R plot was observed on samples In-5-1 and In-5-2 at certain frequencies. For In-5-1, a dip at a reverse voltage of about 0.51 volt was obtained at the frequency of 10 kHz

(see figure 4.11). The dip (at 0.6 volt) for In-5-2 was observed at a lower frequency (4kHz). No special feature was found when other frequncies were adopted. Since all trapping levels are always joined up with the Fermi level, the observed dips might be due to other unknown mechanisms which have not been studied further at the present time.

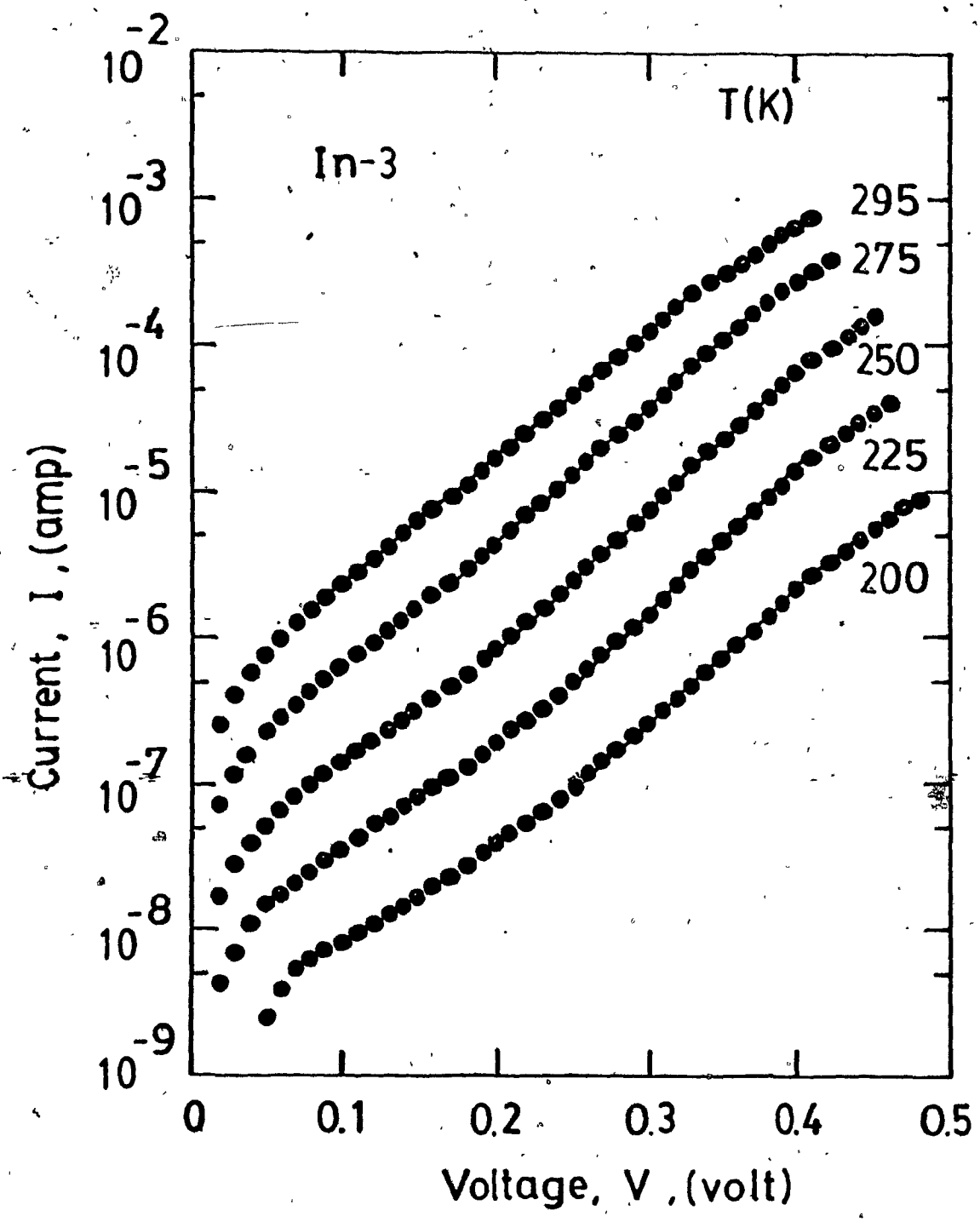

Fig. 4.1 Forward dark current-voltage characteristics of an indium-diffused $CuInSe_2$ homojunction (sample In-3) different temperatures.

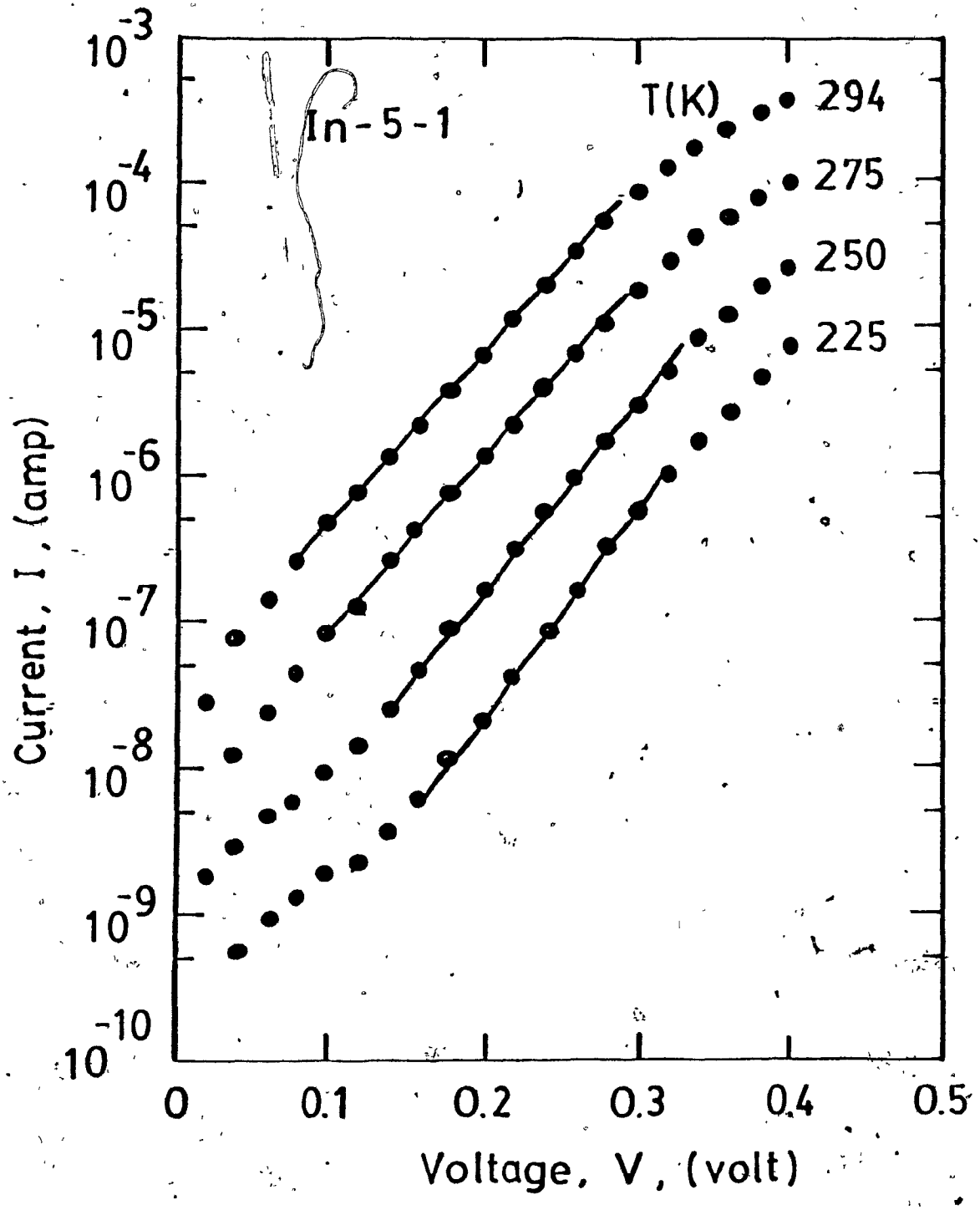

Fig. 4.2 Forward dark current-voltage characteristics of an indium-diffused $CuInSe_2$ homojunction (In-5-1) at different temperatures.

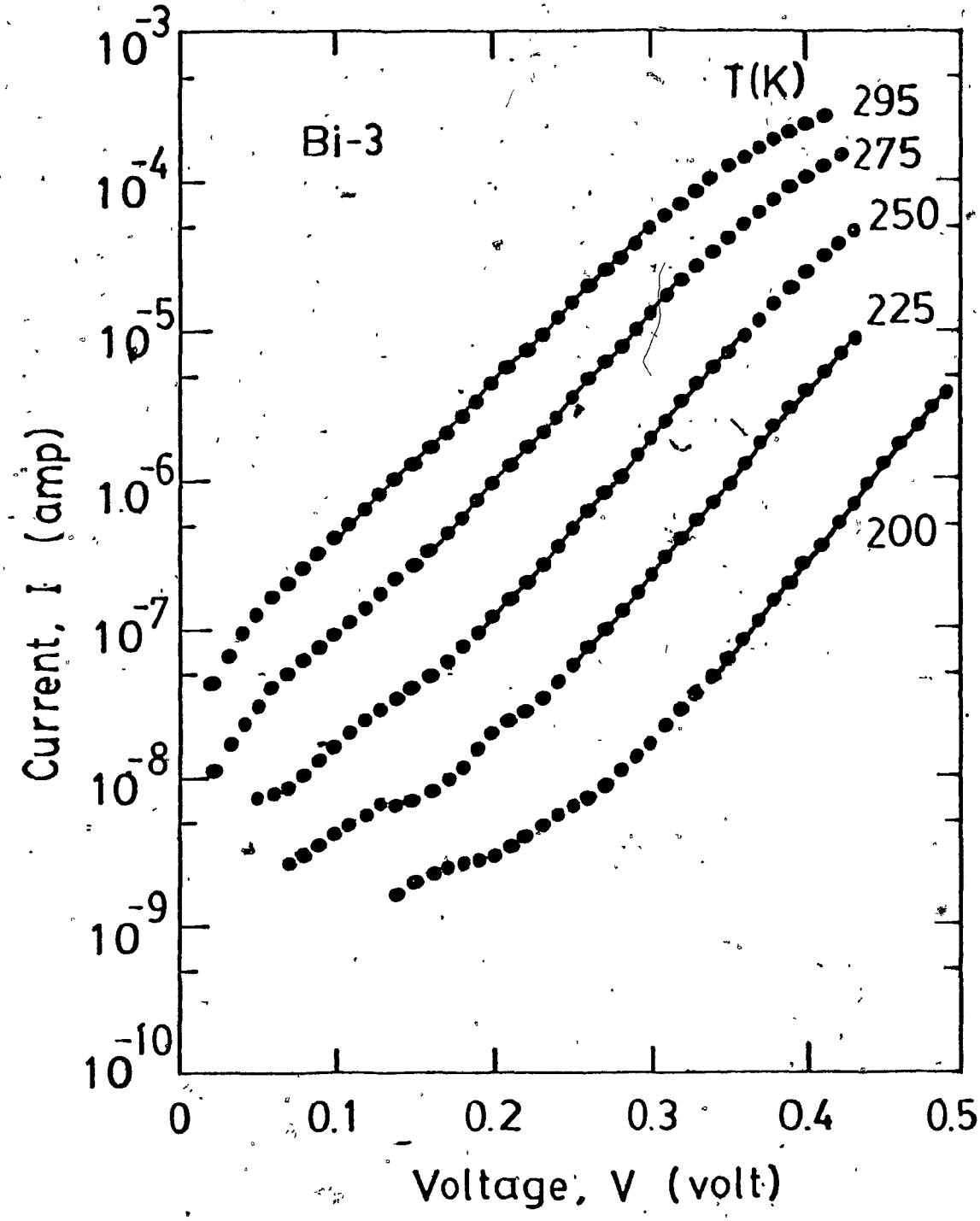

Fig. 4.3 Forward dark current-voltage characteristics of a bismuth-diffused $CuInSe_2$ homojunction (sample Bi-3) at different temperatures.

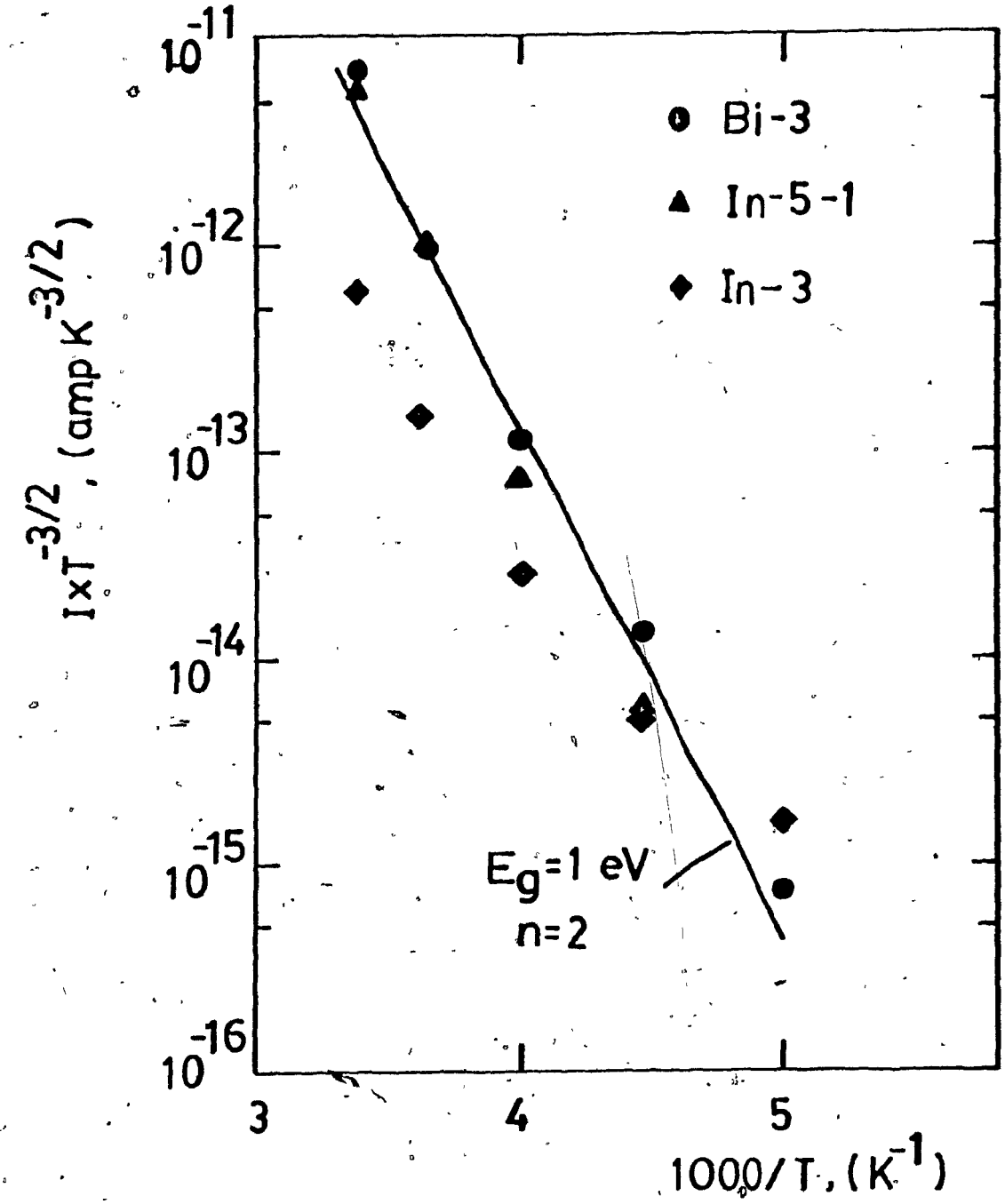

Fig. 4.4 $I_o * T^{-3/2}$ plotted against 1/T for three junctions in a semilogarithmic scale showing essentially linear variation over the temperature range.

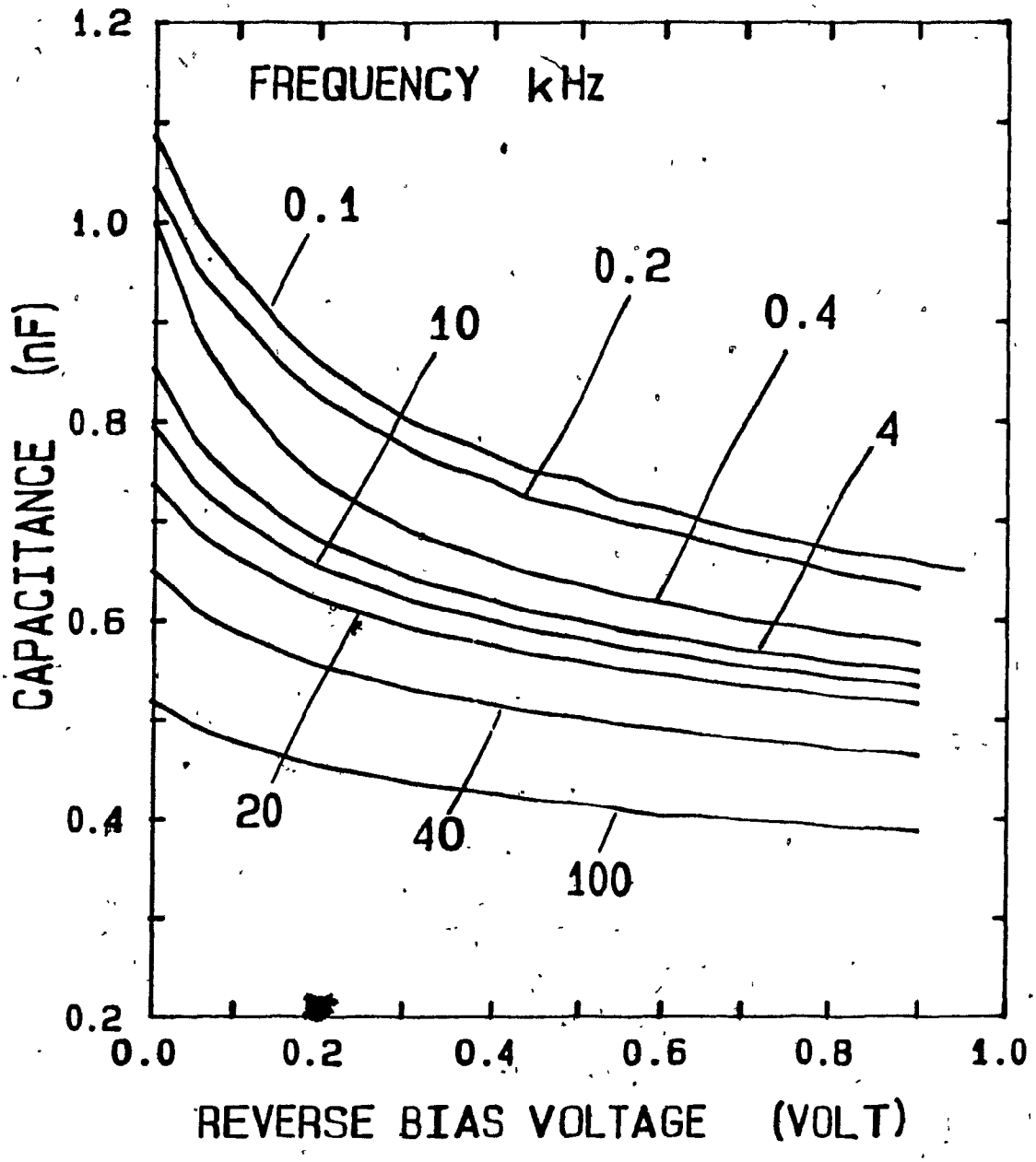

Fig. 4.5 Dark differential capacitance plotted versus reverse bias voltage for a bismuth-diffused sample showing frequency-dependent charar-cteristics.

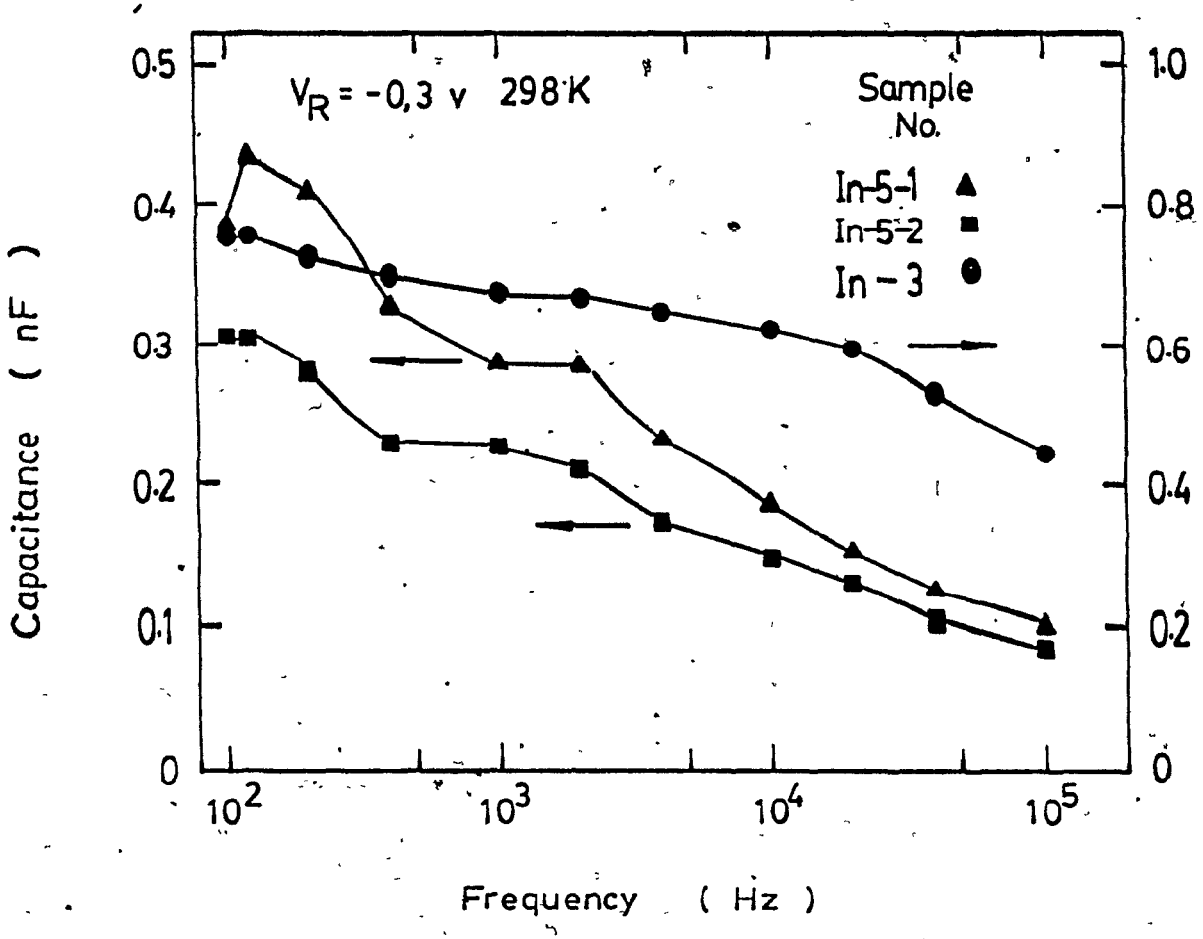

Fig. 4.6 Differential capacitance results for three samples showing the variation with frequency.

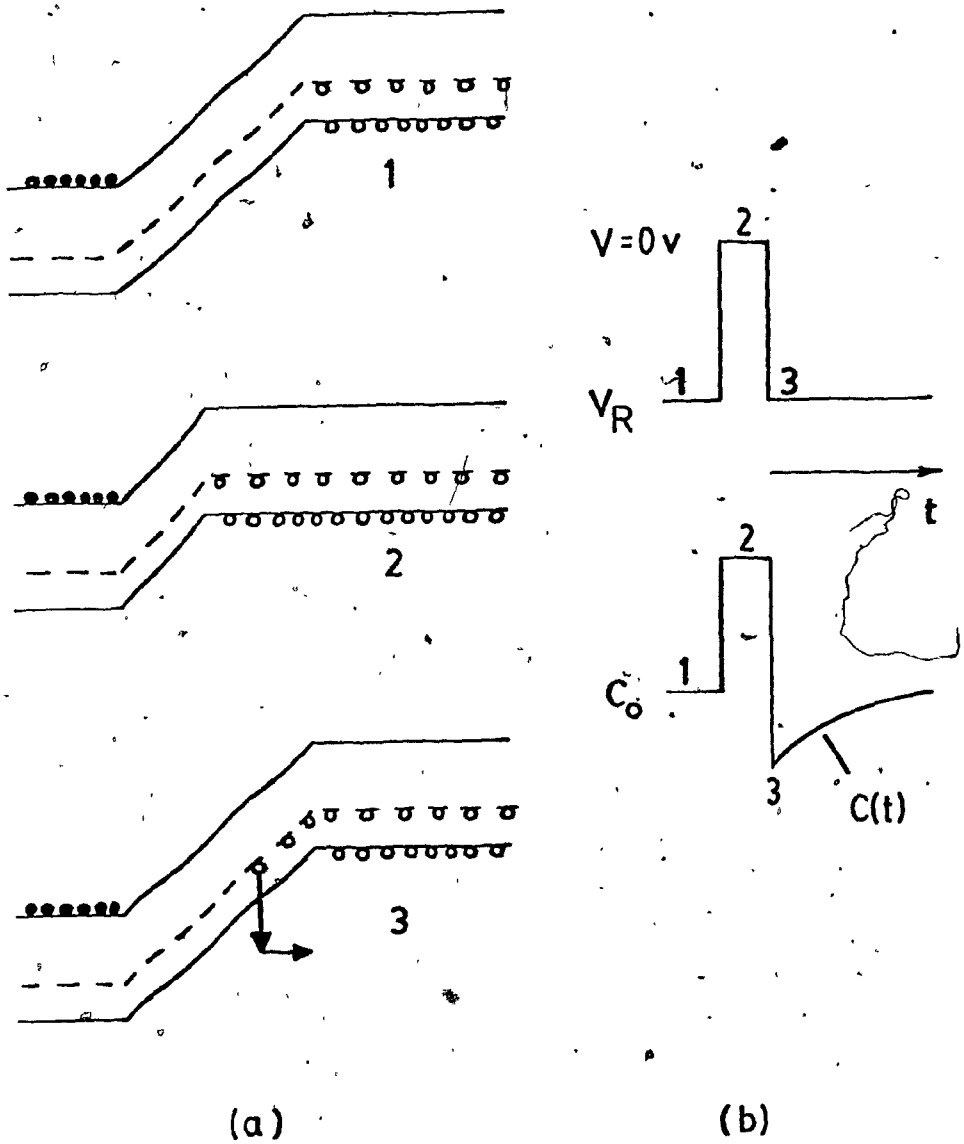

Fig. 4.7 (a) Energy band diagrams of the n^+p $CuInSe_2$ junction at different biasing stages with the zero filling pulse and, (b) biasing sequence and capacitance transient resulting from emission of trapped holes.

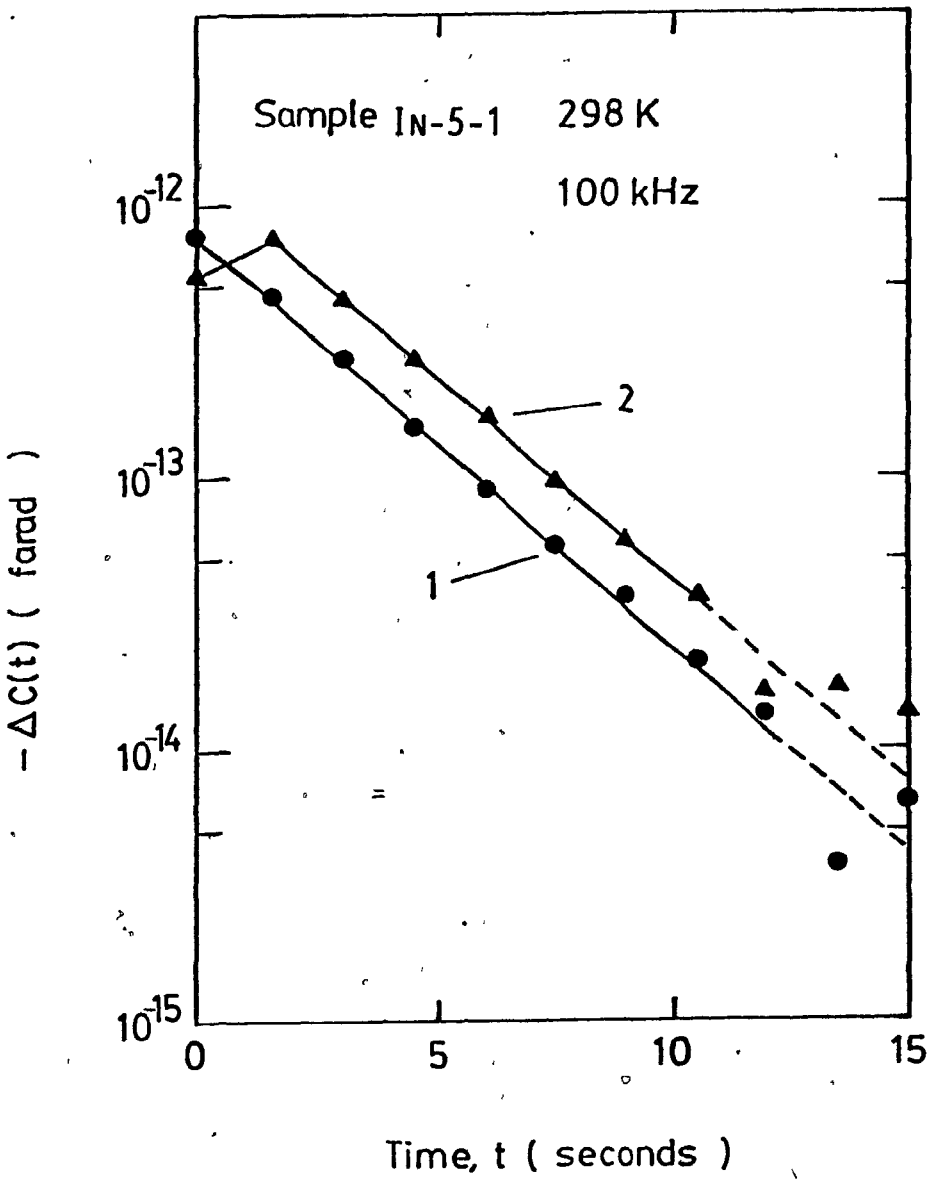

Fig. 4.8 Transient capacitance - $\Delta C(t)$ plotted against time under two different biasing conditions.

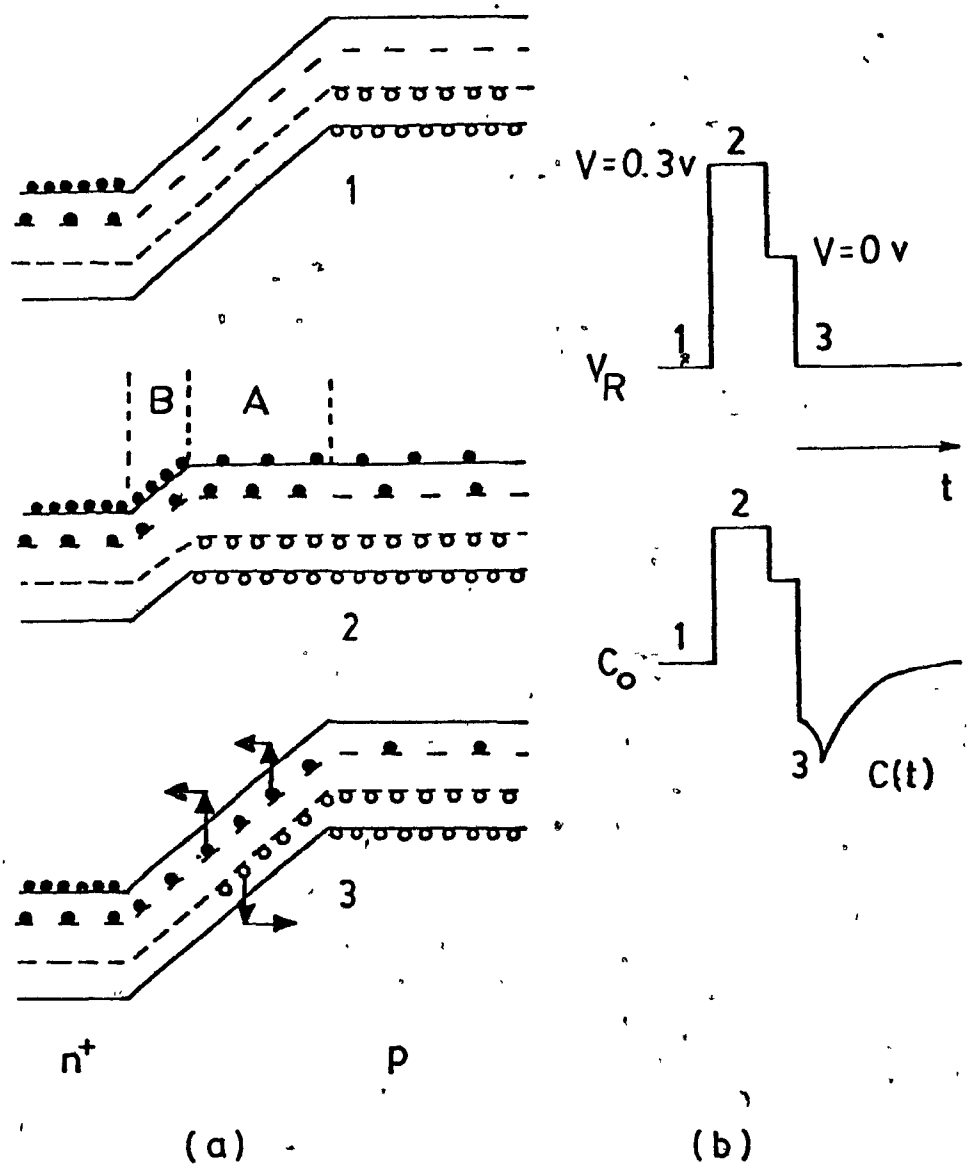

Fig. 4.9 (a) Energy band diagrams of the n^+p $CuInSe_2$ junction at different biasing stages with the 0.3 V forward bias filling pulse and, (b) biasing sequence and the capacitance transient results from emission of both trapped holes and electrons.

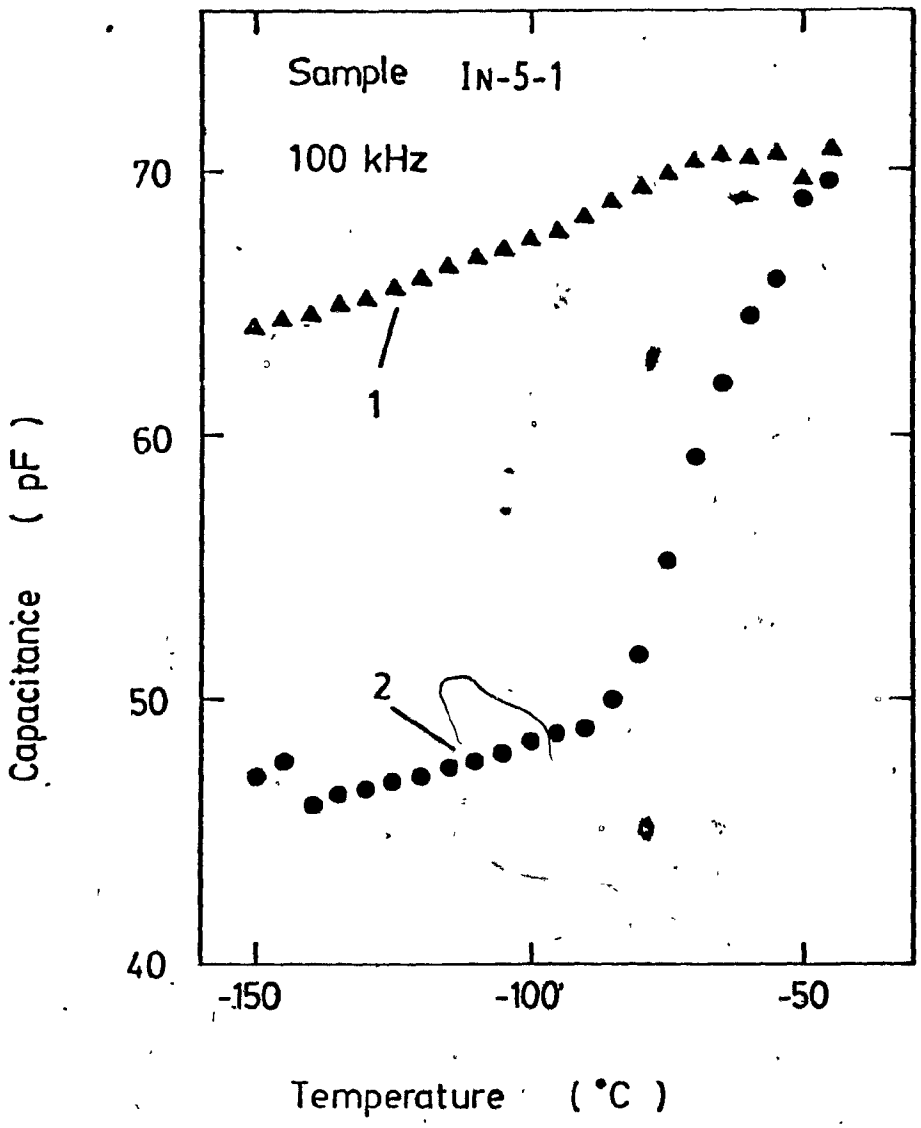

Fig. 4.10 Differential capacitance results plotted versus temperature (TSCAP) for different trap filling conditions.

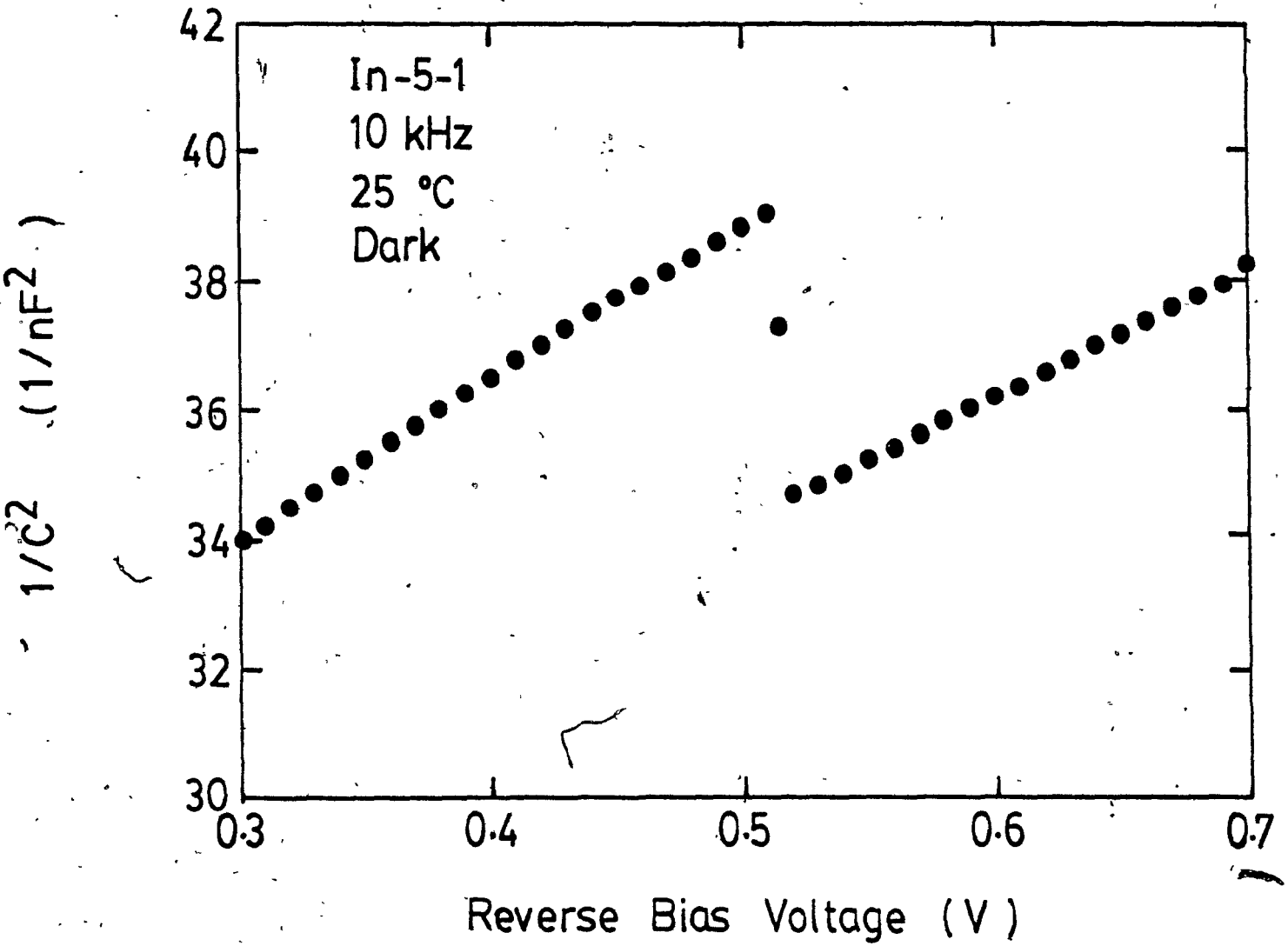

Fig. 4.11 Differential capacitance versus voltage at 100 kHz for sample In-5-1 showing a dip at 0.51 volt.

CHAPTER 5 CONCLUSIONS

Final conclusions of the thesis are given in this chapter. Both $CuInSe_2$ and ZnO, which have been studied in the present work, are promising for terrestrial photovoltaic application. As mentioned before, $CuInSe_2$ has the highest absorption coefficient (for photons with an energy above the band gap value) among any known semiconductors. Because of this, the material has been considered as a potential candidate for terrestrial photovoltaic applications. However, in order to develope $CuInSe_2$ to become a useful material for the future opto-electronic device applications, it is necessary to characterize further the electrical and optical properties. Apart from this, it is also important to study alternative window materials for the $CuInSe_2$-based photovoltaic devices (other than those being used, like CdS and CdZnS). In this work, an important window material, ZnO, has been investigated and used to form $ZnO/CuInSe_2$ heterojunctions. Homojunctions were also fabricated by indium- and bismuth-diffusion. Characteristics of monocrystalline $CuInSe_2$ have been studied by investigating these heterojunctions and homojunctions, and the following main conclusions were obtained.

(1) Good quality, low resistivity ZnO films can be deposited (using rf magnetron sputtering method) on glass substrates by doping using indium or tin. All deposited films show a single phase feature with a preferred (002) orientation. The Sn content in the films was roughly equal to that in the target while the In-content in the film was less than that in the target.

(2) Resistivity of the films decreased by 4 orders of magnitude as the indium oxide content in the target was increased from 0 to 10 wt.%. For tin-doped films, the resistivity decreased by 3 orders of magnitude as the tin oxide content was increased from 0 to 2 wt.%.

(3) Deposition rate and dark electrical resistivity of ZnO films was affected by argon pressure and incident rf power. A relatively high deposition rate (high incident rf power and low argon pressure) will result in a relatively low resistivity.

(4) Optical transmission of indium-doped ZnO films at a wavelength of 0.7 μm was essentially constant, however, it was affected at 0.5 μm wavelength. For tin-doped films, the optical transmission first decreased as the tin content was increased, reached minima at about 5% SnO_2 then increased as the tin content was further increased.

(5) The fabricated ZnO(n)/$CuInSe_2$(p) heterojunctions showed a rectification effect and the ideality factor was about 2.8 in the intermediate voltage range. Temperature-dependent dark current-voltage characteristics measured for these devices suggested that the room temperature current transport in the junctions was dominated by an electron emission and recombination process. In the low voltage region, a second current component was dominant especially for lower temperatures. This current component was believed to be due to a tunneling/recombination mechanism or a shunting effect. The variation of the open circuit voltage covers a wavelength range from 0.4 to 1.4 μm.

(6) An energy band diagram has been constructed for the ZnO(n)/$CuInSe_2$(p) junctions based on the material parameters. In this heterostructure, the conduction band discontinuity is negligible, however, there is a large energy discontinuity (2.3 eV) for the valence band.

(7) From differential capacitance measurements, the apparent diffusion potential was found to be greater than that predicted by the energy band diagram. This is due to a strong dipole effect in the interface region. The polarity of the dipole was found to be the same as that of the space charge and therefore enlarged the diffusion potential.

(8) Isotype ZnO(n)/$CuInSe_2$(n) heterojunctions were also studied. From the dark/illuminated current-voltage characteristics and variation of open circuit voltage with incident optical wavelength (variation of V_{oc} was similar to that for a $CuInSe_2$ homojunction in the wavelength range from 0.55 to 1.35 μm, and the V_{oc} was found to have an opposite polarity in the wavelength ranges from 0.4 to 0.55 and from 1.35 to 1.7 μm), an energy band diagram has been established. The energy bands bend downwards in the space charge region. This effect is believed to be due to the presence of positively charged interface states.

(9) Temperature-dependent dark current-voltage characteristics of both indium and bismuth diffused $CuInSe_2$ homojunctions have been studied in the present work. It was found that the ideality factor was about two for these junctions in the intermediate voltage range and it was almost unchanged when temperature changed from 295 to 200 K. The measured saturation current within the temperature range covered more than 3 orders of magnitude. These effects suggested that the diode current in the intermediate voltage range was mainly controlled by a recombination process through the deep levels in the space charge region.

(10) Differential capacitance measurements over the

frequency range of 10^2-10^5 Hz have been performed on several homojunctions. Frequency-dependent differential capacitance characteristics (value decreased by a factor of 2 to 3 as the frequency was increased from 10^2 to 10^5 Hz) suggested that the density of the total effective traps was comparable to the net acceptor concentration. Constant capacitance region did not exist in the frequency range studied, suggesting that the charging/discharging time constant of the traps covered a relatively large range. Tentative information about the energy position of the traps have been obtained from the thermally stimulated capacitance measurement results.

(11) Transient capacitance effects have been observed in both In- and Bi-diffused junctions. The results suggested that the majority carrier traps with a charging/discharging time constant of about 2.8 seconds are dominant in these transient effects. The effect of minority carrier traps also has been observed.

The present investigation on thin film ZnO and bulk monocrystalline $CuInSe_2$ has results in the above described main conclusions. The information will be useful for future research development of $CuInSe_2$-based photovoltaic cells. However, there are still many questions for $CuInSe_2$ remained to be answered. For example, work is needed to prepare good quality $CuInSe_2$ crystals and to fabricate both homojunction

and heterojunction using such crystals. Differential capacitance measurements should be carried out over a larger frequency range. Furthermore, transient differential capacitance effects should be studied using high speed instrument to obtain a complete set of data for the deep levels.

Both the open circuit voltage and short circuit current density of the ZnO(n)/$CuInSe_2$(p) junctions under simulated AM1 conditions are small. This is due to the large lattice mismatch between the two materials. However, ZnO still will be a useful material if a thin layer of material like CdS is introduced between $CuInSe_2$ and ZnO. This structure has already been reported recently by Potter and coworkers [5.1]. Their devices, having a layer of undoped CdS with a thickness of 500 Å, demonstrated an AM1 conversion efficiency up to 11.2%.

REFERENCES

[1.1] D. M. Chapin, C. S. Fuller and G. L. Pearson, J. Appl. Phys., 25, 676 (1954).

[1.2] M. A. Green, A. W. Blakers, Jiqun Shi, E. M. Keller, S. R. Wenham, R. B. Godfrey, T. Szpitalak and M. R. Willison, 18th IEEE Photovoltaic Spec. Conf., Florida, 386 (1984).

[1.3] J. G. Werthen, H. C. Hamaker and C. F. Ford, 18th IEEE Photovoltaic Spec. Conf., Florida, 1412 (1984).

[1.4] A. M. Hermann, L. Fabick, K. Zweibel and R. Hardy, 16th IEEE Photovoltaic Spec. Conf., Orlando, 840 (1982).

[1.5] R. A. Mickelsen and W. S. Chen, 16th IEEE Photovoltaic Spec. Conf., Orlando, 781 (1982).

[1.6] V. K. Miloslavskii and A. I. Ranyuk, Opt., Spectr., 11, 289 (1961).

[1.7] L. L. Kazmerski, P. J. Ireland, F. R. White and R. B. Cooper, 13th IEEE Photovoltaic Spec. Conf., New York, 185 (1978).

[1.8] W. G. Haines and R. H. Bube, J. Appl. Phys., 49, 304 (1978).

[1.9] E. Shanthi, A. Banerjee, V. Dutta and K. L. Chopra, J. Appl. Phys., 53, 1615 (1982).

[1.10] J. R. Sites, Inst. Phys. Conf. Ser. 43, Chap. 22 (1979).

[2.1] D. C. Reynolds, C. W. Litton and T. C. Collins, Phys. Stat. Sol. 12, 3(1965).

[2.2] T. L. Tansley, D. F. Neely and C. P. Foley, Thin Solid Films, 117, 19(1984).

[2.3] B. T. Khuri-Yakub, G. S. Kino and P. Galle, J. Appl. Phys., 46, 3266(1975).

[2.4] D. E. Brodie, R. Shigh, J. H. Morgan, J. D. Leslie, C. J. Moore and A. E. Dixon, 14th IEEE Photovoltaic Spec. Conf., 486(1980).

[2.5] J. B. Webb, D. F. Williams and M. Buchanan, Appl. Phys. Lett., 39, 640(1981).

[2.6] J. Aranovich, A. Ortiz and R. H. Bube, J. Vac. Sci. Technol., 16, 994(1979).

[2.7] K. Ito and T. Nakazawa, Jpn. J. Appl. Phys., 22, L245(1983).

[2.8] H. Nanto, T. Minami, S. Shooji and S. Takata, J. Appl. Phys., 55, 1029(1984).

[2.9] P. S. Nayar, J. Electronic Materials, 11, 967(1982).

[2.10] T. Minami, H. Nanto and S. Takata, Jpn. J. Appl. Phys., 23, L280(1984).

[2.11] H. R. Koenig and L. I. Maissel, IBM J. Res. Dev., 14, 168(1970).

[2.12] J. O. Barnes, D. J. Leary and A. G. Jordan, J. Electrochem. Soc., 127, 1636(1980).

[3.1] R. L. Anderson, Solid State Electronics, 5, 341 (1962).

[3.2] J. L. Shay, S. Wagner and H. M. Kasper, Appl. Phys. Lett., 27, 89 (1975).

[3.3] M. S. Tomar and F. J. Garcia, Thin Solid Films, 90, 419 (1982).

[3.4] R. H. Rediker, S. Stopek and J. H. R. Ward, Solid State Electronics, 7, 621 (1964).

[3.5] U. Dolega, Z. Naturforsch. 18, 653 (1963).

[3.6] J. P. Donnelly and A. G. Milnes, IEEE Trans. Electron Devices, ED-14, 63 (1967).

[3.7] L. J. van Ruyven, J. M. P. Papenhuijzen and A. C. J. Verhoeven, Solid State Electronics, 8, 631 (1965).

[3.8] A. G. Milnes and D. L. Feucht, Heterojunctions and Metal-Semiconductor Junctions, Academic, New York, 1972.

[3.9] J. P. Donnely and A. G. Milnes, Solid State Electronics, 9, 174 (1966).

[3.10] A. Vahid Shahidi, I. Shih and C. H. Champness, Canadian J. Phys., 63, 811 (1985).

[3.11] G. I. Roberts and C. R. Crowell, J. Appl. Phys., 41, 1767 (1970).

[3.12] W. G. Oldham and A. G. Milnes, Solid State Electronics, 7, 153 (1964).

[3.13] M. A. Seitz and D. H. Waitmore, J. Phys. Chem. Solids, 29, 1033 (1968).

[3.14] L. L. Kazmerski, Proc. 16th IEEE Photovoltaic Spec. Conf., (1982).

[3.15] J. A. Aranovich, D. Golmayo, A. L. Farenbruch and R. H. Bube, J. Appl. Phys., 51, 4260 (1980).

[3.16] S. Wagner J. L. Shay and H. M. Kasper, J. Phys. (France), 36, C-3 101 (1975).

[3.17] W. S. Bear, Phys. Rev., 154, 785 (1967).

[3.18] R. E. Dietz, J. J. Hopfield and D. G. Thomas, J. Appl. Phys., 32, 2282 (1961).

[3.19] T. Irie, S. Endo and S. Kimura, Jpn. J. Appl. Phys., 18, 1303 (1979).

[3.20] J. Parkes, R. D. Tomlinson and M. J. Hampshire, J. Appl. Cryst., 6, 414 (1973).

[4.1] G. Masse and E. Redjai, J. Appl. Phys., 54, 1154 (1984).

[4.2] F. A. Abou-Elfotouh, D. J. Dunlavy, A. M. Herman and L. L. Kazmerski, 6th European Photovoltaic Solar Energy Conference, London, (1985).

[4.3] H. Neumann, R. D. Tomlinson, E. Nowak and N. Avgerinos, Phys. Stat. Sol., (a)56, K137(1979).

[4.4] A. C. Wang and C. T. Sah, J. Appl. Phys., 57, 4645(1985).

[4.5] C. T. Sah, W. W. Chan, H. S. Fu and J. W. Walker, Appl. Phys. Lett., 20, 193(1972).

[4.6] I. Shih, A. Vahid Shahidi and C. H. Champness, J. Crystal Growth, 70, 411(1984).

[4.7] W. Shockley, Bell Syst. Tech. J., 28, 435(1949).

[4.8] C. T. Sah, R. Noyce and W. Shockley, Proc. IRE, 45, 1228(1975).

[4.9] C. T. Sah and V. G. K. Reddi, IEEE Trans. Electron Devices, 11, 345(1964).

[4.10] E. Schibli and A. G. Milnes, Solid State Electronics, 11, 323(1968).

[4.11] L. Hmurcik, L. Ketelsen and R. A. Serway, J. Appl. Phys. 53, 3839(1982).

[5.1] R. R. Potter, C. Eberspacher and L. B. Fabick, 18th IEEE Photvoltaic Spec. Conf., Las Vegas, (1985).